POLITECNICO DI TORINO

Master's Degree in Aerospace Engineering

Master's Degree Thesis

Indirect trajectory optimization for minimum-propellant transfers in the Sagittarius A* black-hole centered system under the general relativity assumptions

Supervisors

Prof. Manuela Battipede

Prof. Luigi Mascolo

Candidate

Ilaria Scafetta

Academic year 2025/2026

Thesis Title

Indirect trajectory optimization for minimum-propellant transfers in the Sagittarius A* black-hole centered system under the general relativity assumptions

Thesis Author

Ilaria Scafetta

Abstract

The increasing interest in deep-space navigation and high-energy astrodynamics motivates the development of trajectory optimization methods capable of operating within relativistic gravitational regimes. While classical astrodynamics provides reliable tools for guidance in weak gravitational fields, future extreme-environment missions and fundamental physics experiments may require a consistent integration of optimal control theory with general relativistic dynamics.

This research presents a relativistic optimal control framework for low-thrust spacecraft trajectory optimization in strong gravitational fields. The problem is formulated within the framework of Einstein's General Relativity and describes the gravitational field using the Schwarzschild metric. Spacecraft motion is defined using the relativistic four-velocity state representation, treating motion as fully three-dimensional and including mass variation due to continuous thrust propulsion. The optimal control problem is solved using Indirect Methods and Pontryagin's Maximum Principle, transforming the trajectory optimization into a Two-Point Boundary Value Problem. The resulting coupled differential system includes both the relativistic equations of motion and the corresponding costate dynamics governing the optimal thrust control law. To demonstrate the capabilities of the proposed framework, a challenging test scenario involving transfers between stars of the S-cluster orbiting the supermassive black hole Sagittarius A* is investigated. The spacecraft propulsion system is modeled as a high-performance magnetic confinement fusion engine enabling continuous low-thrust propulsion within a deep relativistic gravitational potential. Numerical solutions are obtained using Oculus, an optimal control software that integrates the relativistic geodesic dynamics with the optimal control law. The numerical simulations demonstrate the convergence of the indirect optimization scheme and the emergence of a bang–bang optimal thrust structure predicted by the theory. In addition, the conservation of the Hamiltonian along the trajectory confirms the consistency and numerical stability of the relativistic optimal control formulation. The optimized trajectories reflect relativistic orbital dynamics and highlight key relativistic effects, including the divergence between proper time and coordinate time as the spacecraft approaches the event horizon.

The proposed study provides a general methodology for relativistic trajectory optimization and flight dynamics, representing a first step toward trajectory design and navigation tools for spacecraft operating in extreme gravitational environments.

to those who navigate their own spacetime,
who explore distant horizons,
and dream beyond the limits of the known.

Table of Contents

1 Introduction **1**

1.1 The Astrophysics Context . . . 1

1.1.1 Black Holes and Sagittarius A* . . . 1

1.1.2 S-Stars Cluster . . . 3

1.1.3 Engineering Rationale for the Present Thesis . . . 4

1.2 Relativistic Navigation Challenge: the Limits of Classical Mechanics in Strong Gravitational Fields . . . 5

1.3 Thesis Objectives . . . 6

1.4 Structure of the Thesis . . . 7

2 General Relativity Flight Dynamics and Physics Model **9**

2.1 Introduction to General Relativity . . . 9

2.1.1 Geometrical structure: manifold, metric and curvature . . . 11

2.1.2 From Minkowski Spacetime to Curved Spacetime Geometry . . . 12

2.2 Connections and Christoffel Symbols . . . 15

2.2.1 The Levi-Civita Connection . . . 16

2.2.2 Christoffel Symbols . . . 16

2.3 Einstein Field Equations . . . 17

2.3.1 Tensor Formulation . . . 18

2.3.2 Vacuum Equations and the Solution for Sagittarius A* . . . 19

2.4 Schwarzschild Solution . . . 20

2.4.1 Key Assumptions and Birkhoff Theorem . . . 20

2.4.2 The Metric . . . 21

2.4.3 Singularities . . . 24

2.4.4 Schwarzschild Precession of the Pericentre . . . 24

2.4.5 Relativistic Effective Potential . . . 26

2.4.6 Analysis of the Simulation Model . . . 28

2.5 Relativistic Dynamics: The Geodesic Equations . . . 29

2.5.1 Relativistic State Vector and Four-Velocity . . . 29

2.5.2 Analytical Derivation of the Christoffel Symbols . . . 30

2.5.3 The Motion Equations . . . 32

2.6 Thrust and Propulsive Model . . . 34

2.6.1 Perturbed Motion Equations and Covariant Acceleration . . . 34

2.6.1.1 The Orthogonality Constraint . . . 34

2.6.1.2 Thrust Components Calculation 35
2.6.2 Mass Variation and Propellant Dynamics 36
2.6.2.1 Final State Vector and Operational Constraints 36
2.6.2.2 Dynamic Coupling and Thrust-to-Weight Ratio 37
2.6.3 Advanced Propulsion: Magnetic Confinement Fusion 37

3 Optimal Control Theory 42
3.1 Numerical approach: Direct vs Indirect Methods 42
3.1.1 The Choice of Indirect Methods for Relativistic Regimes 43
3.2 Optimal Control Theory 44
3.2.1 Dynamic System and Constraints Definition 44
3.2.2 Augmented Merit Index and Hamiltonian 45
3.2.3 Boundary Conditions for Optimality and Transversality 47
3.2.4 Adjoint Variables Equations and Control Variables 48
3.3 Multi-Point Optimal Control Problem 49
3.3.1 The Functional and Variations in the Multi-Point Domain 51
3.4 The Implemented Boundary Value Problem 52
3.5 OCP in Relativistic Regimes 56
3.5.1 Augmented State Vector and Relativistic Hamiltonian 56
3.5.2 Optimal Direction and Switching Function 58
3.5.3 Differential Equations for Relativistic Adjoint Variables 58
3.6 Computational Framework: OCULUS 59
3.6.1 Architecture and Automation of Initial Guess 60
3.6.2 Validation of the Relativistic Model 60

4 Numerical Simulation and Results 61
4.1 Dynamic Model Validation: Free-fall trajectories 62
4.1.1 Normalization and Reference Units 62
4.1.2 Scenario Setup and Initial Conditions 63
4.1.3 Kinematics of the Spiral and Transition to ISCO 64
4.1.4 Metric Divergence and Time Dilation 66
4.2 Interstellar Transfer Optimization: the S29-S31 Mission 68
4.2.1 Scenario, Boundary Conditions and Numerical Normalization 69
4.2.2 State Vector: from Keplerian Elements to Relativistic Vectors 72
4.2.3 The BVP Challenge: Numerical Solution via Homotopy in OCULUS 73
4.2.4 Orbital Parametrization and Solution Mapping 77
4.2.5 Analysis of the Adjoint Variables Mapping 80
4.2.6 The Optimum Transfer of the S29–S31 Mission 89
4.2.7 Translation into Physical Quantities and Engineering Feasibility of the Mission 97

5 Conclusions and Future Developments 99
5.1 Summary of the Research and Key Achievements 99
5.2 Future Developments and Research Perspectives 101

A Christoffel Symbols for Schwarzschild metric **106**

B Motion equation **108**

C Optimal Control Theory Equations **109**

Dedications **115**

List of Figures

1.1 First image of Sgr A* captured by EHT collaboration . . . 3
1.2 Radio (left) and X-ray (right) image of the surroundings of the super massive Black Hole Sgr A . . . 4

2.1 Geometrical representation of a curved differentiable manifold . . . 12
2.2 Spacetime causal structure . . . 14
2.3 Embedding diagram of curved spacetime . . . 18
2.4 Schwarzschild Precession of the Pericentre . . . 25
2.5 Relativistic effective potential $V_{eff}(r)$ . . . 27
2.6 Topological anatomy of a non-rotating supermassive black hole. . . . 28
2.7 Definition of the spherical coordinate system $\{r, \theta, \phi\}$ . . . 29
2.8 Conceptual schematic of a Direct Fusion Drive utilizing a Field-Reversed Configuration . . . 39

4.1 Spiral Fall Trajectory . . . 65
4.2 Free fall Trajectory results . . . 65
4.3 Time Dilation in Free-fall . . . 67
4.4 3D spatial configuration of the departure orbit (S29) and the target orbit (S31) . . . 70
4.5 One-dimensional Convergence . . . 74
4.6 Complete Optimized Solution . . . 75
4.7 Switching Function . . . 76
4.8 Hamiltonian . . . 77
4.9 3D graphs examples . . . 79
4.10 $\lambda_{r,0}$ vs (f_0, f_{tgt}) . . . 81
4.11 λ_{u^r} vs (f_0, f_{tgt}) . . . 83
4.12 λ_{u^ϕ} vs (f_0, f_{tgt}) . . . 84
4.13 λ_{u^θ} vs (f_0, f_{tgt}) . . . 85
4.14 λ_m vs (f_0, f_{tgt}) . . . 86
4.15 λ_{u^t} vs (f_0, f_{tgt}) . . . 88
4.16 Full Convergence of the $-5° \rightarrow 135°$ Transfer . . . 90
4.17 3D map of the true optimal transfer trajectory . . . 91
4.18 Switching Function $\mathcal{S}_\mathcal{F}$ . . . 92
4.19 Hamiltonian $\mathcal{H}$ . . . 93

4.20 Mass vs τ 94
4.21 Evolution of r, θ, ϕ, vs τ 94
4.22 Velocity u^r, u^θ, u^ϕ vs τ 95
4.23 u^t vs τ 96

5.1 1-0-1-0-1 Switching Structure 102

List of Tables

2.1 Physical parameters used in the simulation. 28
2.2 Non-vanishing Christoffel symbols in Schwarzschild spacetime 31
2.3 Nominal performance parameters for the advanced fusion propulsion system used in the astrodynamics simulation. 40

4.1 Free-fall simulation data 68
4.2 Classical orbital parameters of the stars relative to the focus in Sagittarius A* 70
4.3 Normalized state vectors for the optimal mission configuration 73
4.4 Physical and performance normalized parameters of the global optimum for mission S29–S31 89
4.5 Adjoint Variables Initial Guesses Vector $\boldsymbol{\lambda}_0$ for the Optimal Trajectory . . . 91
4.6 Results for Mission S29–S31 98

Acronyms

BCs	Boundary Conditions.
BVP	Boundary Value Problem.
CoV	Calculus of Variations.
DC	Differential Corrector.
DFD	Direct Fusion Drive.
DU	Distance Unit.
EFE	Einstein Field Equations.
EHT	Event Horizon Telescope.
EIH	Einstein-Infeld-Hoffmann.
FRC	Field-Reversed Configuration.
GR	General Relativity.
HBVP	Hamiltonian Boundary Value Problem.
HTS	High-Temperature Superconductors.
ISCO	Innermost Stable Circular Orbit.
IM	Indirect Methods.
MCF	Magnetic Confinement Fusion.
MIT	Massachusetts Institute of Technology.
MPBVP	Multi-Point Boundary Value Problem.
NLP	Non-Linear Programming.
OCP	Optimal Control Problem.
OCT	Optimal Control Theory.
ODE	Ordinary Differential Equations.

PMP	Pontryagin Minimum Principle.
PN	Post Newtonian.
PPPL	Princeton Plasma Physics Laboratory.
PSFC	MIT Plasma Science and Fusion Center.
SEP	Strong Equivalence Principle.
SI	International System.
SMBH	Super Massive Black Hole.
Sgr A*	Sagittarius A*.
SR	Special Relativity.
STM	State Transition Matrix.
TBVPM	Two-Body Value Problem Method.
TU	Time Unit.
VLT	Very Large Telescope.
VLBI	Very Long Baseline Inteferometry.
VU	Velocity Unit.
WEP	Weak Equivalence Principle.

Chapter 1

Introduction

Space exploration has historically focused its efforts within the boundaries of the Solar System, ruled almost entirely by the laws and principles of classical celestial mechanics formulated by Newton and Kepler. The growing interest in interstellar exploration and the theoretical evolution of advanced propulsion systems require extending the horizons of astrodynamics towards unexplored physical regimes.

This thesis lies at the intersection of space engineering, relativistic astrophysics and optimal control theory, proposing the study, simulation, and optimization of trajectories for a spacecraft operating in the extreme gravitational field of a supermassive black hole. This first chapter serves as a framework for the entire thesis: it outlines the astrophysical context of reference, introduces the intrinsic challenges of navigation in General Relativity, defines the research objectives, and illustrates the structure of the work.

1.1 The Astrophysics Context

One of the most suitable locations to investigate powerful gravitational dynamics in the Milky Way is within the Galactic Center since it is among the most extreme gravitational environments. The black hole is known to be at a distance of about 8.178 kpc from the Sun, in the direction of the Sagittarius constellation and it is heavily covered by gas clouds and interstellar dust. This setting makes the central region inaccessible to observations in the optical spectrum, requiring the use of observational techniques in the radio, infrared, and X-ray bands.

At the heart of this region lies an ultra-compact radio source named Sagittarius A* (Sgr A*): the dynamical analysis of the stars orbiting in its immediate vicinity, conducted for more than two decades, has proved without doubt that it is a supermassive black hole (SMBH).

1.1.1 Black Holes and Sagittarius A*

A **Black Hole** can be described as a spacetime singularity enclosed by an event horizon, defining a region in which the gravitational field is sufficiently strong to prevent any form of signal, including electromagnetic radiation, from reaching distant observers.

Despite being intrinsically unobservable, the presence of a Black Hole can be inferred indirectly through its gravitational effects on the surrounding environment. In particular, the motion of nearby stars often reveals the existence of an extremely massive object confined within a volume significantly smaller than that allowed by any known form of matter. Although Black Holes are a central focus of modern observational astrophysics, their internal structure remains largely unknown, representing a domain of ongoing theoretical investigation and mathematical modeling.Direct imaging of these objects is fundamentally impossible due to their defining properties, however, observational evidence indicates the presence of gravitational fields so extreme that they cannot be accounted for by any alternative compact object, strongly supporting the Black Hole hypothesis.

Sagittarius A*, shown in Figure 1.1, is the supermassive Black Hole located at the dynamical center of the Milky Way. From the perspective of Earth, it appears projected near the boundary between the constellations Sagittarius and Scorpius. High-precision measurements indicate that its position coincides, within approximately $1''$, with the center of a remarkably dense stellar cluster, significantly more concentrated than any comparable structure observed within the galactic disk.

The source Sgr A* was first detected in 1974 by Bruce Balick and Robert L. Brown, who identified it as a compact and exceptionally bright radio emitter. Its unusually high brightness temperature, extremely small angular size, and association with strong infrared and radio continuum emission distinguished it from other galactic sources. Nevertheless, its physical nature could not be conclusively determined at that time based solely on radio observations. The Galactic Center, and Sgr A* in particular, has been extensively investigated by the GRAVITY collaboration, with the aim of testing the predictions of General Relativity and validating the Black Hole paradigm. These observations strongly support the interpretation of Sgr A* as a massive Black Hole described by the Schwarzschild–Kerr family of solutions.

Further investigation and discoveries of Sgr A*'s peculiarity awarded Reinhard Genzel and Andrea Ghez the Nobel Prize in Physics in 2020 and observational confirmation followed in 2022 when the Event Horizon Telescope (EHT) collaboration published the first direct image of the shadow of Sgr A*.

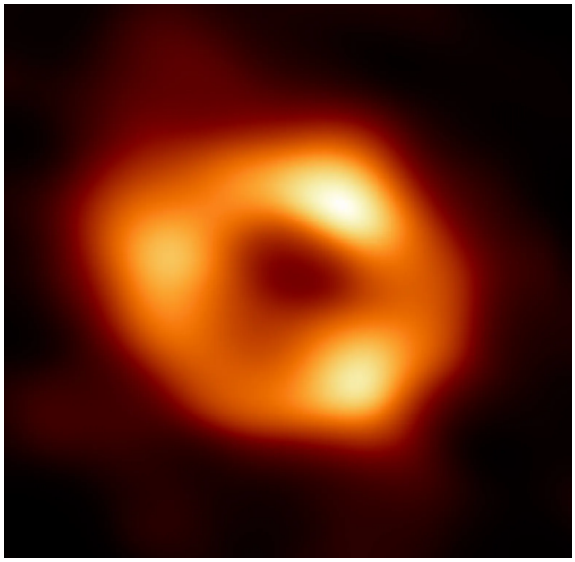

Figure 1.1: First image of Sgr A* captured by EHT collaboration

Through the use of Very Long Baseline Interferometry (VLBI) on a global scale, it was possible to resolve the emission coming from the region immediately outside the event horizon, providing direct verification of the predictions of General Relativity in strong gravity. The most recent measurements, particularly those obtained with the GRAVITY instrumentation installed in the Very Large Telescope (VLT), gave an estimate of the mass of Sgr A*.

$$M_{SgrA*} \approx 4.297 \times 10^6 M_\odot$$

Despite the enormous mass, the characteristic dimensions on an astrodynamics scale are compact. The Schwarzschild radius for Sagittarius A* takes a value of

$$R_s \approx 1.27 \times 10^{10}\text{m}$$

To make a comparison, this distance is lower than the distance between the Sun and Mercury at its perihelion, highlighting an extremely high concentration of mass within a relatively small volume.

The combination of multi-million solar mass and geometric compactness generates a gravitational field characterized by intense curvature of space-time. In the vicinity of R_s, the dynamics of test particles and orbiting bodies cannot be described by Newtonian approximations: the escape velocity approaches the speed of light, the proper time of a local observer undergoes significant dilation compared to the coordinate time measured at a great distance, and geodesic trajectories are substantially affected by the metric structure of space-time.

1.1.2 S-Stars Cluster

Orbiting very close to the supermassive black hole is a dense cluster of stars, mainly young and massive, known as S-Cluster. Because of the huge gravitational attraction exerted

by Sgr A*, these stars have very perturbed Keplerian orbits, with high eccentricity and orbital velocities that can reach significant fractions of the speed of light c.

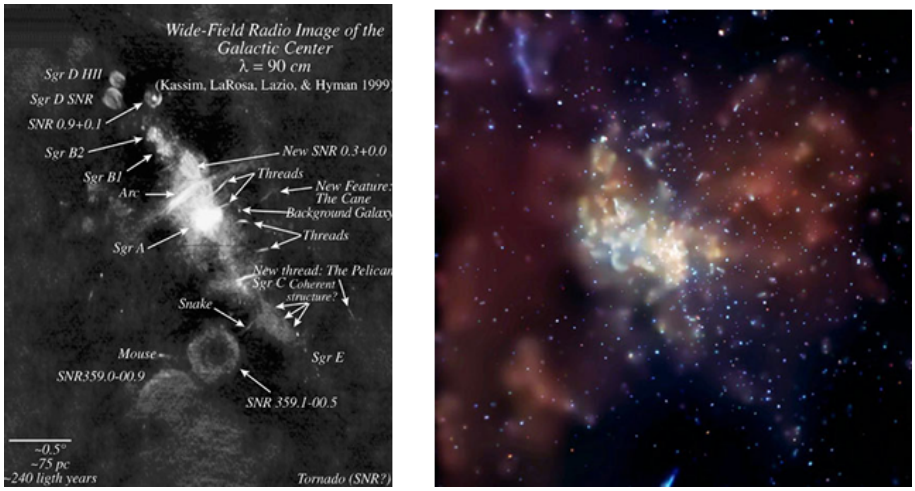

Figure 1.2: Radio (left) and X-ray (right) image of the surroundings of the super massive Black Hole Sgr A

In recent years, thanks to high-precision optical and interferometric instruments, astronomers have been able to trace the kinematics of several stars in the cluster, detecting non-negligible macroscopic relativistic deviations from classical Newtonian orbits. Specifically, for stars that penetrate deeper into the potential well, effects such as gravitational redshift and Schwarzschild precession have been successfully measured. This peculiar star cluster constitutes a natural environment for testing the predictions of Einstein's General Theory of Relativity in a strong-field regime.

Although these systems are primarily studied in astrophysics, they also provide an extreme testbed for the development of advanced astrodynamics and trajectory optimization methodologies.

1.1.3 Engineering Rationale for the Present Thesis

The gravitational environment of the Galactic Center, characterized by

- High space-time curvatures,
- Relativistic orbital velocities,
- Strong dynamical nonlinearity,

represents a completely different context compared to classical astrodynamics.

In this thesis, this scenario is taken as the theoretical operational theater for the analysis of a relativistic orbital transfer problem. In particular, a hypothetical automated spacecraft that must perform a transfer between stellar orbits is considered, aiming at optimizing propellant consumption in a gravitational field described by the Schwarzschild metric.

The objective is not to propose a mission that is realistically feasible in the short term, but rather to develop a mathematical and numerical framework capable of rigorously

addressing optimal control problems in a strong relativistic regime. In such a dynamic context, the planning of propelled trajectories requires a complete departure from classical astrodynamics.

1.2 Relativistic Navigation Challenge: the Limits of Classical Mechanics in Strong Gravitational Fields

Classical astrodynamics architecture is based on the hypothesis that the gravitational fields are weak and the operating velocities are lower than the speed of light

$$v \ll c$$

In such regimes, a space vehicle's motion can be modelled with high accuracy through Newton's Equations, considering space as a three-dimensional Euclidean domain and time as an absolute parameter independent from the dynamic state of the system.

In the gravitational field of the supermassive black hole Sagittarius A*, these hypotheses do not hold true anymore: the dynamics cannot be described as the effect of a force acting in a fixed space but rather has to be defined within General Relativity, in which free motion corresponds to the evolution along the geodesic of a curved space-time. Gravity does not appear as a force term but is embedded in the metric structure that rules the trajectories propagation.

From an engineering point of view, this means a substantial redefinition of the state variables. The vehicle is not described by a vector of six dimensions $(\mathbf{r}, \mathbf{v})$ but by an eight-dimensional representation that includes the time components necessary to describe the four-position and four-velocity vectors. One of the major and most relevant implications concerns the time notion. In a relativistic context one has to distinguish coordinate time t, defined with respect to a remote observer, from proper time τ, measured by the onboard clock. The notion of time will be discussed in more detail further on. The propulsion system delivers thrust according to proper time τ, while orbital constraints and boundary conditions are formulated in the global coordinate frame. This results in a dynamic problem in which state propagation requires simultaneous evaluation of spatial evolution and transformation between t and τ, which depends on the depth of the gravitational field and local velocity.

The introduction of continuous thrust further modifies the framework. In classical mechanics, thrust translates into an additive term of acceleration superimposed on Newtonian gravity. In General Relativity, however, the action of the thruster represents a forced deviation from the natural geodesic. The variation of the spatial components of the four-velocity produces a coupled effect on the temporal component as well: the resulting dynamics are highly nonlinear and exhibit a marked sensitivity to initial conditions and control parameters. From a numerical perspective, the use of impulsive methodologies or classical optimization techniques is inadequate and, instead, the problem takes the form of a constrained nonlinear differential system, for which a rigorous formulation in terms of continuous optimal control is required.

This thesis addresses the challenge by applying Pontryagin's Maximum Principle, transforming the relativistic trajectory problem into a two-point boundary value problem (TPBVP) solved numerically.

1.3 Thesis Objectives

In light of the limitations of classical orbital mechanics in strong gravity, this work aims to develop a rigorous mathematical framework for the optimization of propelled trajectories in the curved space-time generated by a supermassive black hole. The novelty of this work lies in coupling relativistic orbital dynamics with continuous low-thrust optimal control.

The primary goal is to minimize the propellant consumption or, equivalently, to maximize the vehicle's final mass during an orbital transfer between bodies belonging to the S-Cluster orbiting around Sagittarius A*. The vehicle is modeled on a high-performance continuous thrust propulsion system based on a magnetic confinement nuclear fusion reactor, characterized by an effective exhaust velocity equal to a significant fraction of the speed of light ($c_e = 0.05c$).

To achieve this overall objective, the work is divided into three fundamental sub-objectives.

1. **Definition of the relativistic dynamic model**

   The first objective is to implement a complete spatial dynamic model, without restricting motion to the equatorial plane $\theta = \pi/2$, as is often the case in simplified studies.

   The vehicle is described by the equation of perturbed motion in Schwarzschild metric under the General Relativity assumptions, propagating a nine-component state vector including:

   - the four space-time coordinates,
   - the four-velocity components,
   - the evolution of the spacecraft mass as an additional state variable

   The four-velocity is subject to the relativistic norm restriction, which introduces a structural coupling between the dynamic components. The independent variable of integration is the proper time τ of the vehicle.

2. **Formulation of the Optimal Control Problem**

   The second objective concerns the formulation of the problem in terms of continuous Optimal Control. Through the use of the Indirect Method and Pontryagin's Maximum Principle, the relativistic control Hamiltonian is defined and the differential equations of the adjoint variables are derived. Maximizing the Hamiltonian leads to the analytical determination of the optimal control law for the orientation and intensity of the thrust, characterized by a Bang-Bang type structure and formalized by means of the so-called Primer Vector.

3. **Validation of the numerical algorithm and results analysis**

   The third objective is to implement the problem within the *Oculus* software to validate the algorithm, with particular attention to numerical stability, sensitivity to initial conditions, and verification of convergence towards physically acceptable and optimal solutions.

Achieving these objectives allows relativistic dynamics and optimal control theory to be integrated into a single coherent computational framework, providing a quantitative tool for analyzing propelled trajectories in strong gravity conditions.

1.4 Structure of the Thesis

To meet the ambitious goals established, this thesis is divided into five main chapters, logically structured to guide the reader from the definition of the astrophysical environment to the analysis of the optimization of the numerical results.

- **Chapter 1 - Introduction**: This chapter outlines the astrophysical context of the Galactic Center and of the supermassive black hole Sagittarius A*. It also defines the engineering challenges of navigation in the relativistic regime, the reasons for the research and the primary objectives of the Thesis.
- **Chapter 2 - General Relativity Flight Dynamics and Physics Model**: The chapter provides the mathematical foundations of the simulation environment. Einstein's General Relativity is explained, the Schwarzschild metric is introduced to define the spacetime curvature and the Christoffel Symbols are derived. Furthermore, the geodesic and three dimensional perturbed motion equations are specified, rigorously distinguishing between proper and coordinate time.
- **Chapter 3 - Optimal Control Theory**: This section explains the "algorithmic engine" of the Thesis. After a comparison between direct and indirect numerical methods, the Indirect Method based on the Pontryagin's Maximum Principle (PMP) is applied. The problem is formalized as a Multi-Point Boundary Value Problem (MPBVP) to manage the Bang-Bang structure of the thruster. The presentation concludes with the analytical derivation of the Hamiltonian Problem in General Relativity, defining the Relativistic Primer Vector, the control laws for the optical orientation of the thrust and shooting method.
- **Chapter 4 - Numerical Simulation and Results**: Chapter 4 constitutes the core application of the work, presenting the results obtained with the numerical algorithm. The optimized transfer trajectories between the orbits of the S-Cluster stars are analyzed, examining the temporal evolutions of the controls, the mass consumption, and the deep influence of relativistic effects on the interstellar space flight geometry.
- **Chapter 5 - Conclusions and Future Developments**: The final chapter summarizes the goals achieved by the research, discusses the implications of the obtained

results for future exploration in deep space and suggests possible improvements or directions for further study.

Chapter 2

General Relativity Flight Dynamics and Physics Model

To carry out a mission analysis in the proximity of the Galactic Center, it is necessary to have a radical paradigm shift with respect to classical astrodynamics. Although Newtonian mechanics has been successful for decades in the exploration of the Solar System, it proves inadequate when the system's characteristic velocities become a fraction of the speed of light and the gravitational field becomes so intense that it ends up deforming the space and time structure itself.

Sagittarius A*, the supermassive black hole located in the center of the Milky Way, represents an extreme gravitational environment and, to study the orbital dynamics and correctly model trajectories in this setting, adding perturbative terms to Kepler's Equation is not sufficient: a mathematical framework capable of describing motion not as a response to a force, but rather as a path through curved geometry becomes necessary.

This chapter presents the theoretical framework, from the historical and conceptual foundation of Einstein's theory to the rigorous definition of the Schwarzschild metric and the geodesic equations, building the mathematical substrate on which the optimization work completed in this thesis is based.

2.1 Introduction to General Relativity

The formulation of General Relativity, completed by Albert Einstein in 1915, is not only a simple extension of the Newtonian theory, but a reformulation of classical physics, as it does not describe gravity as a force, but as a manifestation of the geometry of the space-time. The theory finds its foundations in the conflict between two pillars: Newton's Law of Universal Gravitation and Special Relativity (SR).

In 1905, Einstein had already published the theory of Special Relativity, which merged space and time under a single four-dimensional structure. However, in that study, gravitation had not yet been included, and it was still defined by the Law of Universal Gravitation formulated by Newton in the 17th century, according to which two masses attract each other with a force directly proportional to the product of their masses and inversely proportional

to the square of the distance separating them.

According to Newton, gravitational force acts instantaneously at a distance and two events occurring at distinct locations take place at the same instant for all observers, regardless of their state of motion. This concept was in clear contrast with the relativistic principle that no information can travel faster than light and, even though it might have been possible to modify Newton's Law to align with Special Relativity, Einstein chose not to pursue this path, but instead to formulate an entirely new theory that would change the concepts of space, time and gravitation and that began with the formulation of two main principles: the Equivalence Principle, which provides physical intuition, and the General Covariance Principle, which provides the mathematical tool to construct a universal gravitational theory.

The Equivalence Principle

As mentioned, the starting point for Einstein's considerations has been the mass. In classical physics, the mass can be distinguished in two different ways:

1. Inertial mass (m_i): the resistance of a body to an acceleration, defined by the Second Law of Motion ($F = m_i a$).

2. Gravitational mass (m_g): the intensity of gravitational interaction, defined by the Law of Universal Gravitation
$$F = G\frac{M \cdot m_g}{r^2} \tag{2.1}$$

In the 19th century, Eötvös' experiments proved with great precision that:

$$m_i = m_g \tag{2.2}$$

Einstein elevated this congruence to a fundamental principle, formulating the Weak Equivalence Principle (WEP), according to which a particle's motion in any gravitational field does not depend on its mass and composition and, therefore, all bodies fall at the same acceleration in vacuum.

In 1907, he extended this concept to the Strong Equivalence Principle (SEP), which states that:

> *In a small enough region of spacetime, the outcomes of any experiment, gravitational or non-gravitational, are independent of the velocity and location of the freely falling reference frame in which they are performed.*

The principle brings with it several implications. First, all physics laws, including those of electromagnetism, nuclear forces, and quantum mechanics, must be the same for observers in free-fall as they are for observers in an inertial frame of reference.

Second, if gravity can be locally transformed away for an observer in free fall, then gravity is not an absolute force as, for example, electromagnetism is, but instead it depends on the state of motion of the observer.

And finally, it is not possible to define a global inertial system for the whole Universe: only local inertial systems can exist. Mathematically, this requires space-time to be a curved manifold: a surface that appears to be flat on an infinitesimal scale, but that has intrinsic curvature on a macroscopic scale. Therefore, the trajectories of free-falling bodies are not curves because of a force acting on them, but they are the straightest possible lines in this curved geometry.

General Covariance Principle

Once gravity is encoded in the curvature of spacetime, Einstein had to write the physics laws under these new assumptions, since in classical physics and in Special Relativity, the laws were written with respect to an inertial observer. However, if, as stated, one cannot define a global inertial system, physics laws valid for any observer regardless of its state of motion were needed.

This concept is delineated as the General Covariance Principle, and it states:

The laws of physics must take the same form in all coordinate systems.

The principle reflects deep ideas:

1. Space-time has no fixed background structure.
2. Geometry itself is dynamic and determined by physical content.
3. Physics must be formulated independently of arbitrary coordinate choices.

This requirement leads to the determination of the mathematical language of Einstein's theory: tensor equations. A tensor is a mathematical representation of a physical quantity characterized by magnitude and dependence on multiple directions.

$$A_{\mu\nu} = B_{\mu\nu} \tag{2.3}$$

If a tensor equation is true in a coordinate system x^μ, the rules of tensor algebra guarantee that it will be true in any other coordinate system x'^μ, since both terms of the equation transform covariantly under general coordinate transformations. In general, tensor equations preserve their structure under arbitrary differentiable coordinate changes, thus satisfying the principle of covariance. This formalism makes it possible to express gravitational dynamics through relations between geometric tensors and physical tensors.

2.1.1 Geometrical structure: manifold, metric and curvature

The mathematical translation of the Equivalence Principle requires abandoning the concept of Euclidean space as a global container for physics events.

In General Relativity, the Universe is modeled as a curved four-dimensional spacetime, defined as a manifold, that has a metric structure that determines its intrinsic geometry. To better comprehend gravity, it is important to distinguish between the geometry that describes physics at a local level, and the one that describes it on a broader global level and in the presence of mass.

Spacetime as a differentiable Manifold

Formally, spacetime is defined as a 4-dimensional differentiable manifold $\mathcal{M}$. The definition of manifold perfectly represents the Strong Equivalence Principle: although $\mathcal{M}$'s global structure might be topologically complex and have a non-zero curvature, it is locally diffeomorphic to $\mathbb{R}^4$.

This means that for each event point $P \in \mathcal{M}$, there exists an open set $U \subset \mathcal{M}$ and a bijective map $\psi : U \to \mathbb{R}^4$ that allows one to describe any event through four real coordinates $\{x^0, x^1, x^2, x^3\}$. Conventionally, the temporal coordinate is $x^0 = ct$, where c denotes the speed of light and t represents coordinate time.

A major distinction, usually overlooked in classical mechanics but of crucial importance in GR, is that physics vectors do not lie on the curved manifold itself, but they belong to the Tangent Space $T_P\mathcal{M}$ defined at P. Therefore, tangent space is a flat vector space that linearly approximates the manifold in an infinitesimal neighbourhood of P.

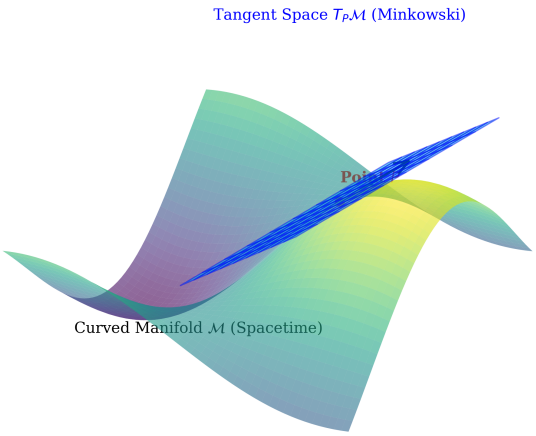

Figure 2.1: Geometrical representation of a curved differentiable manifold

Figure 2.1 shows the geometrical representation of a curved differentiable manifold $\mathcal{M}$ and its locally flat tangent space $T_P\mathcal{M}$ defined at point P. Physics vectors and the laws of Special Relativity operate within this flat local approximation.

2.1.2 From Minkowski Spacetime to Curved Spacetime Geometry

In Tangent Space $T_P\mathcal{M}$, the Special Relativity laws hold, and one can introduce a local inertial frame in which the metric locally reduces to the Minkowski form $\eta_{\mu\nu}$. In Cartesian coordinates, it takes the constant diagonal form:

$$\eta_{\mu\nu} = \text{diag}(-1, +1, +1, +1) = \begin{pmatrix} -1 & 0 & 0 & 0 \\ 0 & 1 & 0 & 0 \\ 0 & 0 & 1 & 0 \\ 0 & 0 & 0 & 1 \end{pmatrix} \tag{2.4}$$

The invariant interval in tangent space is given by the formulation:

$$ds^2 = \eta_{\mu\nu} d\xi^\mu d\xi^\nu = -c^2 d\tau^2 + dx^2 + dy^2 + dz^2 \tag{2.5}$$

However, in the presence of gravity, it is not possible to extend this flat metric to the entire manifold $\mathcal{M}$. The transition to General Relativity occurs by substituting the constant tensor $\eta_{\mu\nu}$ with a general metric tensor field $g_{\mu\nu}(x)$, whose components vary point by point as a function of the coordinates x^μ.

The general metric tensor g is a symmetric tensorial field of rank $(0, 2)$ that determines the manifold's intrinsic geometry. It generalizes the Pythagorean theorem to the curved spacetime, defining the scalar product between two vectors $u, v \in T_P\mathcal{M}$:

$$\mathbf{u} \cdot \mathbf{v} = g_{\mu\nu} u^\mu v^\nu \tag{2.6}$$

The invariant line element ds^2, which represents the four-dimensional distance between two events separated by an infinitesimal displacement dx^μ, becomes:

$$ds^2 = g_{\mu\nu}(x) dx^\mu dx^\nu = \sum_{\mu=0}^{3} \sum_{\nu=0}^{3} g_{\mu\nu}(x) dx^\mu dx^\nu \tag{2.7}$$

The presence of mass and energy deforms the components of $g_{\mu\nu}$, making the geodesics no longer straight, but instead curves that follow the geometry of spacetime.

The metric tensor $g_{\mu\nu}$ therefore encodes all the geometric information of spacetime and fully determines its causal and dynamical structure. It must comply with three fundamental mathematical properties:

1. **Symmetry**: $g_{\mu\nu} = g_{\nu\mu}$. This reduces the components from 16 to 10.
2. **Non-degeneracy**: $\det(g) \neq 0$. This guarantees the existence of the inverse metric tensor $g^{\mu\nu}$, such that $g^{\mu\lambda} g_{\lambda\nu} = \delta^\mu_\nu$, necessary for raising tensor indices.
3. **Lorentzian signature**: $(-1, +1, +1, +1)$. This is a key property as it preserves the physical distinction between time and space.

The indefinite nature of the Lorentzian metric signature subdivides the tangent space into three distinct regions, thereby establishing the causal structure of the theory

- **Timelike**, $ds^2 < 0$: it corresponds to events that can be linked by a particle with mass, such as a space vehicle. For these trajectories, one can define the proper time τ:

$$d\tau = \frac{1}{c} \sqrt{-g_{\mu\nu} dx^\mu dx^\nu} \tag{2.8}$$

- **Lightlike**, $ds^2 = 0$: it describes trajectories travelled by photons and massless particles. Geometrically, these vectors form the local Light Cone, or causality limit, in every point P
- **Spacelike**, $ds^2 > 0$: it connects events that cannot causally influence each other, as it would require superluminal propagation.

To visually synthesize this causal structure, Figure 2.2 illustrates the Minkowski Light Cone, which geometrically separates the accessible regions of spacetime from the causally disconnected ones.

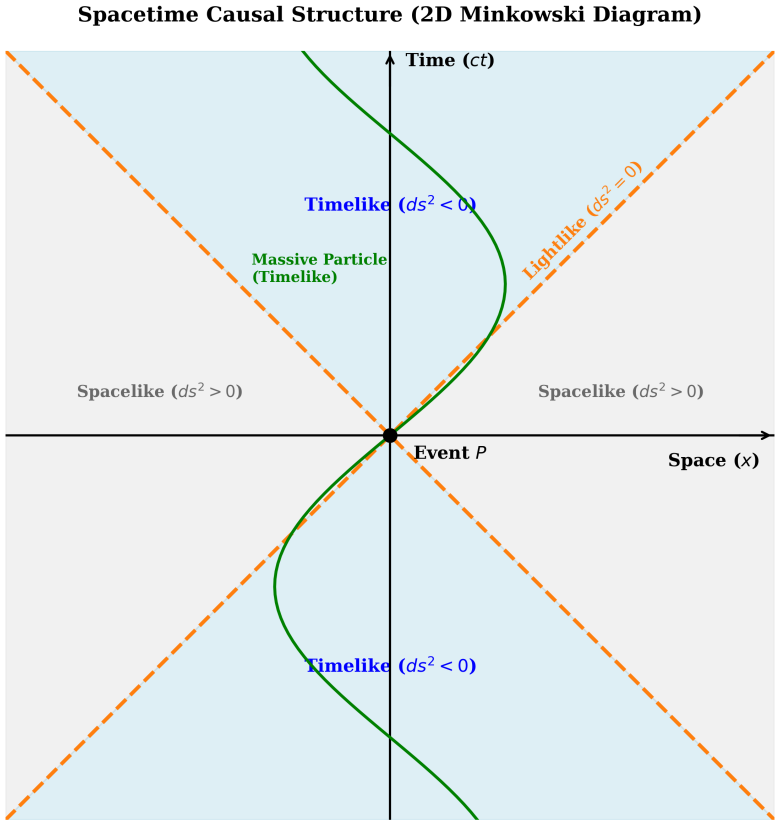

Figure 2.2: Spacetime causal structure

The Light Cone divides the tangent space around an event P into Timelike regions (accessible future and past for massive particles), Lightlike boundaries (photon trajectories), and Spacelike regions (causally disconnected). In this thesis project, the integration of the motion equation happens with respect to the first parameter, therefore to Timelike trajectories. The four-velocity normalization condition $u^\mu u_\mu = -c^2$ precisely proves the fact that the spacecraft's trajectory must always remain of the Timelike type.

While the metric defines distances and causal structure, it is through its derivatives that spacetime curvature emerges.

The metric tensor is therefore the central dynamical variable of General Relativity. Its evolution is governed by the Einstein Field Equations, which will be introduced in section 2.3.

The Curvature and Riemann Tensor

The main distinction between Minkowski's flat space and Riemann's curved one can be described with the concept of Curvature. Although it is always possible to make the Christoffel symbols vanish at a single point by choosing a free-falling system, it is not possible to cancel them in an entire neighbourhood if the space is curved. The intrinsic measurement of such curvature is given by the Riemann Tensor $R^{\rho}_{\sigma\mu\nu}$, defined as:

$$R^{\rho}_{\sigma\mu\nu} = \partial_{\mu}\Gamma^{\rho}_{\nu\sigma} - \partial_{\nu}\Gamma^{\rho}_{\mu\sigma} + \Gamma^{\rho}_{\mu\lambda}\Gamma^{\lambda}_{\nu\sigma} - \Gamma^{\rho}_{\nu\lambda}\Gamma^{\lambda}_{\mu\sigma} \tag{2.9}$$

In physics, this tensor measures the relative acceleration between two close geodesics, which corresponds to the tidal force. If $R^{\rho}_{\sigma\mu\nu} \neq 0$, spacetime is curved and tidal effects cannot be eliminated by any choice of reference frame, as gravity is irreducibly present. This shows that curvature is not an effect occurring in spacetime but a property of spacetime itself.

The metric tensor defines distances, causal structure, and local inertial properties of spacetime. However, to describe how vectors change from point to point and how curvature dynamically influences motion, an additional geometric structure is required: the affine connection. This leads to the introduction of Christoffel symbols and, ultimately, to the geodesic equations that govern motion in curved spacetime.

2.2 Connections and Christoffel Symbols

The introduction of a curved differentiable manifold brings with it the mathematical problem of how to compare vectors defined at different points of the spacetime.

In flat space, it is possible to rigidly transport a vector from a point P to a point Q while maintaining it parallel to itself, and one can notice the distinction between the two. In a curved manifold, tangent spaces $T_P\mathcal{M}$ and $T_Q\mathcal{M}$ are separate and there does not exist a unique method to move one vector without introducing an additional structure that designates the concept of parallelism. This structure is known as **Connection** and it allows to relate tangent spaces that are close to each other, denoting the rules for the derivation of tensorial fields.

Furthermore, the partial derivative ∂_{μ}, commonly used for infinitesimal calculus, cannot be applied to a vector V^{ν} in a generic manifold, because it does not transform and change coordinates like a tensor as it does not take accountability of how the vector changes from point to point due to the curvature. Thereby, to preserve the General Covariance, the **Covariant Derivative** ∇_{μ} has to be defined:

$$\nabla_{\mu}V^{\nu} = \partial_{\mu}V^{\nu} + \Gamma^{\nu}_{\mu\lambda}V^{\lambda} \tag{2.10}$$

In the equation,

- The first term $\partial_{\mu}V^{\nu}$ measures the variation of the vector's components;
- $\Gamma^{\nu}_{\mu\lambda}$ are the connection coefficients, known as the **Christoffel symbols**

- The second term $\Gamma^{\nu}_{\mu\lambda}V^{\lambda}$ is a corrective term which balances the variation of basis vectors in the coordinate system

This definition ensures that tensorial character is preserved under general coordinate transformations.

2.2.1 The Levi-Civita Connection

Mathematically, one can find infinite possible connections on a manifold. However, in General Relativity, a specific connection is used, the Levi-Civita Connection, that imposes two important physics constraints relating the connection to the metric $g_{\mu\nu}$:

1. **Symmetry and zero torsion**: a radical property to define a standard spacetime is that the infinitesimal parallelogram shall close with vanishing torsion. In order to guarantee so, it is required that the parallel transport is symmetrical, and therefore that the Christoffel symbols remain unchanged with respect to the interchange of the lower indices:

$$\Gamma^{\lambda}_{\mu\nu} = \Gamma^{\lambda}_{\nu\mu} \tag{2.11}$$

2. **Metric Compatibility**: the parallel transport of a vector along the curve shall maintain its length and angle with other vectors transposed in parallel. Considering the differential terms, it means that the metric tensor's covariant derivative shall be equal to zero anywhere, since the metric remains constant through the connection:

$$\nabla_{\rho} g_{\mu\nu} = 0 \tag{2.12}$$

From these considerations and the Levi-Civita Connection, the Christoffel symbols may be derived and subsequently, the basis of the Einstein Field Equations and geodesics can be defined.

2.2.2 Christoffel Symbols

The computational importance of the Christoffel symbols in this study is that they embody the gravitational terms in the motion equation. The explicit expression has been derived in terms of the metric partial derivatives starting from the condition of metric compatibility.

By expanding the covariant derivative:

$$\nabla_{\rho} g_{\mu\nu} = \partial_{\rho} g_{\mu\nu} - \Gamma^{\lambda}_{\rho\mu} g_{\lambda\nu} - \Gamma^{\lambda}_{\rho\nu} g_{\mu\lambda} = 0 \tag{2.13}$$

Equation 2.13 can be rewritten exchanging the indices μ, ν, ρ three times:

1. $\partial_{\rho} g_{\mu\nu} = \Gamma^{\lambda}_{\rho\mu} g_{\lambda\nu} + \Gamma^{\lambda}_{\rho\nu} g_{\mu\lambda}$
2. $\partial_{\mu} g_{\nu\rho} = \Gamma^{\lambda}_{\mu\nu} g_{\lambda\rho} + \Gamma^{\lambda}_{\mu\rho} g_{\nu\lambda}$
3. $\partial_{\nu} g_{\rho\mu} = \Gamma^{\lambda}_{\nu\rho} g_{\lambda\mu} + \Gamma^{\lambda}_{\nu\mu} g_{\rho\lambda}$

Adding equations 2 and 3, subtracting equation 1 and using the tensor's symmetry and the symmetry 2.11, the following is obtained:

$$\partial_\mu g_{\nu\rho} + \partial_\nu g_{\rho\mu} - \partial_\rho g_{\mu\nu} = 2g_{\lambda\rho}\Gamma^\lambda_{\mu\nu}$$

The last passage is to multiply both terms of the equation by the inverse metric tensor $g^{\sigma\rho}$, use the property $g^{\sigma\rho}g_{\lambda\rho} = \delta^\sigma_\lambda$ and, finally, isolate the Christoffel symbol:

$$\Gamma^\lambda_{\mu\nu} = \frac{1}{2}g^{\lambda\sigma}\left(\frac{\partial g_{\sigma\mu}}{\partial x^\nu} + \frac{\partial g_{\sigma\nu}}{\partial x^\mu} - \frac{\partial g_{\mu\nu}}{\partial x^\sigma}\right) \tag{2.14}$$

Equation 2.14 represents one of the main features used for the orbital propagation implemented in the software developed for this thesis. Differently from Newtonian gravity, in which the field is characterized by a single scalar potential Φ, in four dimensions, the connection has 64 components in total. However, despite their number, these coefficients do not represent the fundamental gravitational degrees of freedom: they are constructed from first derivatives of the metric tensor, which contains the true dynamical variables of the theory. The coefficients are, in fact, not tensors: their values depend on the reference frame, and they can be locally set equal to zero in a free-falling system.

2.3 Einstein Field Equations

While differential geometry and tensorial calculations give the basis to describe a curved spacetime, the Einstein Field Equations (EFE) constitute the dynamical laws. The equations, published in their definitive form in November 1915, are the core of General Relativity and they represent the relation between the manifold geometry and its energy and matter content.

The EFE can be viewed as a generalization of Poisson's equation[1] for Newtonian gravitation. As discussed, in classical physics, the gravitational source is described by a scalar quantity, and the field is represented by a scalar potential Φ. In Einstein's framework, this structure is extended: the source becomes the second-order energy–momentum tensor, while the gravitational field is no longer a potential but is encoded directly in the spacetime metric tensor.

This mutual dependence between geometry and matter is captured by John Archibald Wheeler's well-known statement:

> *"Spacetime tells matter how to move; matter tells spacetime how to curve."*

> *"Spacetime tells matter how to move; matter tells spacetime how to curve."*

This profound mutual dependence between mass-energy and geometry is visually conceptualized in an embedding diagram (Figure 2.3), which represents the spatial curvature induced by a massive body like Sagittarius A*.

[1] $\nabla^2\Phi = 4\pi G\rho$

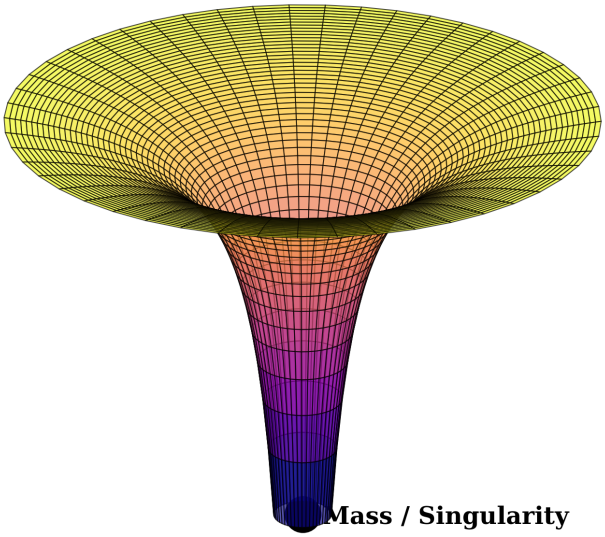

Figure 2.3: Embedding diagram of curved spacetime

The presence of a massive body deforms the surrounding geometric "fabric", creating a gravitational well. In General Relativity, orbits and trajectories are the geodesics traversing this curved topology.

2.3.1 Tensor Formulation

Einstein Field equations are a ten second-order non-linear partial differential equation system.

$$G_{\mu\nu} \equiv R_{\mu\nu} - \frac{1}{2}Rg_{\mu\nu} = \frac{8\pi G}{c^4}T_{\mu\nu} \tag{2.15}$$

Equation 2.15 depicts the canonical form and by analyzing each term, the deep theory architecture becomes evident.

1. $G_{\mu\nu}$**: Einstein Tensor**
   The term on the left side of the equation describes the geometry by combining two curvature measurements:

   - Ricci Tensor $R_{\mu\nu}$: it is obtained from the contraction of Riemann Tensor (see Equation 2.9), it represents the average curvature of spacetime and describes how volumes change under geodesic deviation.
   - Ricci Scalar R: it is the trace of the Ricci Tensor, which gives a scalar measurement of the curvature in every point.

   The specific combination of the two is the following

$$R_{\mu\nu} - \frac{1}{2}Rg_{\mu\nu} \tag{2.16}$$

The relation in Equation 2.16 is not arbitrary: in fact, it is mathematically proven that it is the only tensorial combination to satisfy Bianchi's contracted identities

$$\nabla^{\mu} G_{\mu\nu} = 0 \tag{2.17}$$

These identities hold purely for geometrical reasons and are independent of the dynamical content of the theory. Consistency of the Einstein Field Equations therefore requires that the source term satisfies

$$\nabla^{\mu} T_{\mu\nu} = 0$$

which expresses local conservation of energy and momentum.

2. $T_{\mu\nu}$**: Energy-momentum Tensor**
   The right-hand side term describes the field's source, since in GR, the mass is not the only gravity source. Tensor $T_{\mu\nu}$ includes:

   - The energy density T_{00}
   - The energy flux and momentum density T_{0i}
   - The momentum flux T_{ii}, that consists of isotropic pressure and shear stresses

   This implies, for example, that a star's internal pressure or heat gives a contribution to the gravitational field.

3. κ**: Einstein Gravitational Constant**
   Factor $\kappa = \frac{8\pi G}{c^4}$ is determined by imposing that, when in weak fields with velocities not comparable to the speed of light, the theory converges to the Newtonian gravity. The numerical value is very low ($\kappa \approx 2.07 \times 10^{-43} \frac{m}{kg \cdot s^2}$) and it demonstrates how stiff spacetime really is: extremely large concentrations of energy and mass are needed in order to create a noticeable curvature, such as in the case of Black Holes or Neutron Stars.

2.3.2 Vacuum Equations and the Solution for Sagittarius A*

The study focuses on the orbital dynamics outside of the Event Horizon of the supermassive black hole Sagittarius A* (Sgr A*). To first approximation, the external region can be modeled as vacuum, therefore, $T_{\mu\nu} = 0$, the EFE are reduced to the **Vacuum Solution**:

$$R_{\mu\nu} - \frac{1}{2} R g_{\mu\nu} = 0 \implies R_{\mu\nu} = 0 \tag{2.18}$$

This condition, known as Ricci-Flatness, in which the Ricci Tensor is reduced to zero, does not imply that the spacetime is flat, because in order to reach such conditions and so, to have the Minkowski flat space, the whole Riemann Tensor 2.9 must be reduced to zero.

In the space around a mass, the Riemann Tensor does not vanish, and it is exactly this Riemann residual curvature the one that defines the gravitational field which propagates

in void, generating the tidal forces that curve and influence the spacecraft's trajectories simulated in this work.

The vacuum approximation neglects the influence of surrounding stellar populations and accretion flows. However, at the orbital radii considered in this work, such contributions are negligible compared to the dominant curvature generated by the central black hole. Schwarzschild metric, fully explained in Section 2.4, is precisely the unique solution of the Vacuum Equation 2.18 for a spherical and symmetrical geometry.

2.4 Schwarzschild Solution

Schwarzschild solution has been an outstanding breakthrough for both General Relativity and the whole 20th century physics. In January 1916, just two months after the publication of the Einstein Field Equation 2.15, the astronomer Karl Schwarzschild obtained what was the first exact, analytic and non-trivial solution of the equations. According to the well-known Einstein equation:

$$E = mc^2$$

Energy is equivalent and proportional to mass and, because the gravitational field is encoded in the metric tensor itself, and the curvature tensors depend non-linearly on the metric and its derivatives, gravity is intrinsically self-interacting. In particular, the Ricci tensor contains both second derivatives of the metric and quadratic terms in the Christoffel symbols, which are themselves constructed from first derivatives of the metric. This property of **self-interaction** of gravity makes the superposition principle invalid and, for this reason, the field generated by two bodies is not equal to the vector sum of the two individual fields. The complexity given by these characteristics makes exact analytic solutions, such as the Schwarzschild one, extremely rare.

For this study, Schwarzschild metric has been considered the physical model defining the spacetime around the black hole Sagittarius A*. It is on this curved manifold that the optimal control problem is formulated, and the spacecraft's dynamics integrated.

2.4.1 Key Assumptions and Birkhoff Theorem

Schwarzschild metric describes the gravitational field around a spherical, static and electrically neutral mass. Its mathematical development follows the application of four physics and symmetry conditions to the vacuum equations 2.18:

1. **Spherical symmetry:** spacetime is invariant with respect to spatial rotations. The linear element on the 2-sphere must preserve the standard form $d\Omega^2 = d\theta^2 + \sin^2\theta d\phi^2$, with the consequent implication that gravity acts uniformly in all radial directions.

2. **Static nature:** the metric coefficients $g_{\mu\nu}$ are independent from the time coordinate $\partial_t g_{\mu\nu} = 0$ and the metric is invariant for time reversal $t \to -t$. This condition excludes the presence of source rotation which would introduce terms related to drag, and ensures the absence of gravitational waves.

3. **Vacuum Condition:** if $r > 0$ then the energy-momentum tensor is equal to 0 throughout the domain.

4. **Asymptotic Flatness:** for $r \to \infty$, the metric shall asymptotically approach the Minkowski metric tensor $\eta_{\mu\nu}$ reflecting the fact that at great distances the gravitational influence of the central mass vanishes, with the consequence of making it possible to identify the gravitational constant with the source gravitational mass M.

In 1923, with **Birkhoff Theorem** it was proven that:

Schwarzschild solution is the only spherically symmetrical solution to the Einstein equation in vacuum.

The implication is significant: the solution is necessarily static even if the central source is not, as long as it keeps its spherical symmetry. If a star or black hole pulsed radially in "breathing mode", and so expanding and contracting, the external gravitational field would not be affected and would exactly follow the description of the static Schwarzschild metric.

It is worth emphasizing that the Schwarzschild solution describes a **non-rotating** black hole. A rotating black hole would instead be described by the Kerr metric, which introduces frame-dragging effects and a qualitatively different orbital structure.

2.4.2 The Metric

The most general form of the metric describing a static and spherically symmetric spacetime can be written as

$$ds^2 = -f(r)\,dt^2 + h(r)\,dr^2 + r^2\left(d\theta^2 + \sin^2\theta\,d\phi^2\right) \tag{2.19}$$

This symmetry significantly simplifies the problem of determining the ten components of the metric tensor $g_{\mu\nu}$, reducing it to the determination of two functions, $f(r)$ and $h(r)$, which depend solely on the radial coordinate.

To proceed, one computes the Ricci tensor $R_{\mu\nu}$ associated with the metric and imposes the vacuum Einstein field equations:

$$R_{\mu\nu} = 0 \tag{2.20}$$

which must be satisfied by the unknown functions f and h.

Solving these equations leads to the relation:

$$\frac{f'}{f} + \frac{h'}{h} = 0 \tag{2.21}$$

from which it follows that:

$$f = Kh^{-1} \tag{2.22}$$

where K is an integration constant. This constant can be set equal to unity through a suitable rescaling of the time coordinate.

The general solution for $f(r)$ takes the form:

$$f(r) = 1 + \frac{C}{r} \tag{2.23}$$

where C is another integration constant. Substituting this result into the metric yields:

$$ds^2 = -\left(1 + \frac{C}{r}\right) c^2 dt^2 + \left(1 + \frac{C}{r}\right)^{-1} dr^2 + r^2 d\Omega^2 \tag{2.24}$$

where $d\Omega^2 = d\theta^2 + \sin^2\theta \, d\phi^2$.

This solution is asymptotically flat, meaning that as $r \to \infty$, the metric approaches that of Minkowski spacetime expressed in spherical coordinates. This property allows the Schwarzschild metric to be interpreted as describing the gravitational field outside an isolated, spherically symmetric mass.

The physical interpretation of the constant C can be obtained by considering the weak-field limit ($r \to \infty$) and comparing the resulting motion of a test particle with Newtonian gravity. This comparison shows that consistency with Newtonian dynamics requires:

$$m = -\frac{C}{2} \tag{2.25}$$

With this identification, the metric can be rewritten as:

$$ds^2 = -\left(1 - \frac{2m}{r}\right) c^2 dt^2 + \left(1 - \frac{2m}{r}\right)^{-1} dr^2 + r^2 d\theta^2 + r^2 \sin^2\theta \, d\phi^2 \tag{2.26}$$

Here, m represents the geometrized mass (or gravitational radius), related to the physical mass M by:

$$m = \frac{GM}{c^2} \tag{2.27}$$

Substituting this expression into the metric yields the standard Schwarzschild line element:

$$ds^2 = -\left(1 - \frac{2GM}{c^2 r}\right) c^2 dt^2 + \left(1 - \frac{2GM}{c^2 r}\right)^{-1} dr^2 + r^2 d\theta^2 + r^2 \sin^2\theta \, d\phi^2 \tag{2.28}$$

From this expression, the non-zero components of the metric tensor $g_{\mu\nu}$ can be directly identified as:

$$g_{\mu\nu} = \begin{pmatrix} -\left(1 - \frac{2GM}{c^2 r}\right) & 0 & 0 & 0 \\ 0 & \left(1 - \frac{2GM}{c^2 r}\right)^{-1} & 0 & 0 \\ 0 & 0 & r^2 & 0 \\ 0 & 0 & 0 & r^2 \sin^2\theta \end{pmatrix} \tag{2.29}$$

The region in which the Relativity effects become truly dominant is established by **Schwarzschild Radius** R_s, defined as:

$$R_s = \frac{2GM}{c^2} \tag{2.30}$$

By substituting this characteristic length in Equation 2.28, the final equation of the

Schwarzschild metric is obtained

$$ds^2 = -\left(1 - \frac{R_s}{r}\right) c^2 dt^2 + \left(1 - \frac{R_s}{r}\right)^{-1} dr^2 + r^2(d\theta^2 + \sin^2\theta d\phi^2) \tag{2.31}$$

Equation 2.31 highlights several of the main properties of the spacetime geometry and to implement a correct mission simulation it is important to understand the meaning of the measures of t and r, as they differ from what is measured in classical physics.

The Radial Coordinate r

Differently from Euclidean geometry, the term g_{rr} expresses that the proper radial distance between two points is not equal to the difference between their radial coordinates. The variable r, in fact, does not represent the radial distance from the center but it is geometrically defined in a way that a sphere centered in r would have exactly an area of $A = 4\pi r^2$ and an equatorial circumference of $C = 2\pi r$.

The *real* physical distance between two given spherical shells at r_1 and r_2 is given by the integration of the spatial metric component:

$$\Delta L = \int_{r_1}^{r_2} \sqrt{g_{rr}} dr = \int_{r_1}^{r_2} \frac{dr}{\sqrt{1 - R_s/r}} \tag{2.32}$$

Since the denominator is always smaller than 1, it follows that $\Delta L > r_2 - r_1$, clear evidence that space is *radially* stretched in the vicinity of the mass.

The Time Coordinate t

The coordinate t coincides with the time measured by an inertial observer located at the asymptotic infinity. For a space vehicle traveling in the extreme gravitational field of Sgr A*, time flows at a different rhythm. The differential relation between coordinate time t and proper time τ measured onboard, is ruled by the gravitational redshift factor

$$d\tau = \sqrt{-g_{tt}} dt = \sqrt{1 - \frac{R_s}{r}} dt \tag{2.33}$$

The term $g_{tt} = -(1 - \frac{R_s}{r})$ suggests that, while getting closer to the horizon $r \to R_s$, the proper time measured by a static clock at distance r is slower than the time measured by an observer at infinite distance and, therefore, that a finite time interval onboard corresponds to an infinite time interval for an external observer. This phenomenon justifies the use of proper time τ as the independent variable in the software developed, as it allows to avoid the numerical singularities linked to the freeze of coordinate time.

It is also instructive to consider the weak-field limit, for $r \gg R_s$. Expanding the metric component g_{tt} for small values of $\frac{R_s}{r}$, one obtains

$$g_{tt} \approx -\left(1 + \frac{2\Phi}{c^2}\right) \tag{2.34}$$

Where $\Phi = -\frac{GM}{r}$ is the classical Newtonian gravitational potential.

This expansion provides continuity between classical astrodynamics and relativistic orbital mechanics, because it shows that at large distances from the black hole, the relativistic corrections are negligible, and Newtonian orbital mechanics is an excellent approximation, while closer to the event horizon, the relativistic terms dominate, which justifies the use of full General Relativity in the simulation.

2.4.3 Singularities

The analysis of the metric coefficients in equation 2.31 reveals two divergence points:

- **The Coordinate singularity $r = R_s$:** When doing calculations at this distance, the metric appears to be singular. However, this depends on the choice of the Schwarzschild coordinate: in fact, to establish whether the singularity is reached, a curvature invariant given by the complete contraction of the Riemann Tensor, known as the Kretschmann's Scalar K needs to be introduced:

$$K = R_{\alpha\beta\gamma\delta}R^{\alpha\beta\gamma\delta} = \frac{48G^2M^2}{c^4r^6} \tag{2.35}$$

  Since the curvature is finite, tidal forces are finite, and an observer in free fall can cross this surface without suffering catastrophic local consequences. Evaluating K at $r = R_s$, a finite value is obtained:

$$K(R_s) = \frac{3}{4R_s^4} \tag{2.36}$$

  Physically, this surface is the **Event Horizon**, a one-way membrane that causally separates the inside close to the Black Hole from the outside.

- **The Physical singularity $r = 0$:** For $r \to 0$, Kretschmann's Scalar 2.35 diverges, $K \to \infty$: at this point the curvature becomes infinite and the classical description of spacetime is not valid anymore. This is an essential singularity, unremovable by any change of coordinates. In the simulation model this region is excluded from the integration domain.

2.4.4 Schwarzschild Precession of the Pericentre

It is often advantageous to investigate the geometry of orbital motion in Schwarzschild spacetime by expressing the radial coordinate as a function of the azimuthal angle, i.e., $r = r(\phi)$, rather than describing the evolution in terms of coordinate time $r(\tau)$. Within this framework, the distinction between Newtonian coordinate time t and relativistic proper time τ becomes less central, as the focus shifts to the parametrization of the trajectory.

In classical mechanics, the conservation of angular momentum, $L = r^2\, d\phi/dt$, enables to parameterize motion and express time as a function of the angular coordinate, ultimately deriving the orbital equation $r(\phi)$. An analogous procedure applies in General Relativity, where the conserved quantity $L = r^2\, d\phi/d\tau$ allows the proper time τ to be expressed in terms of ϕ, leading again to a description of the trajectory in the form $r(\phi)$. As a result,

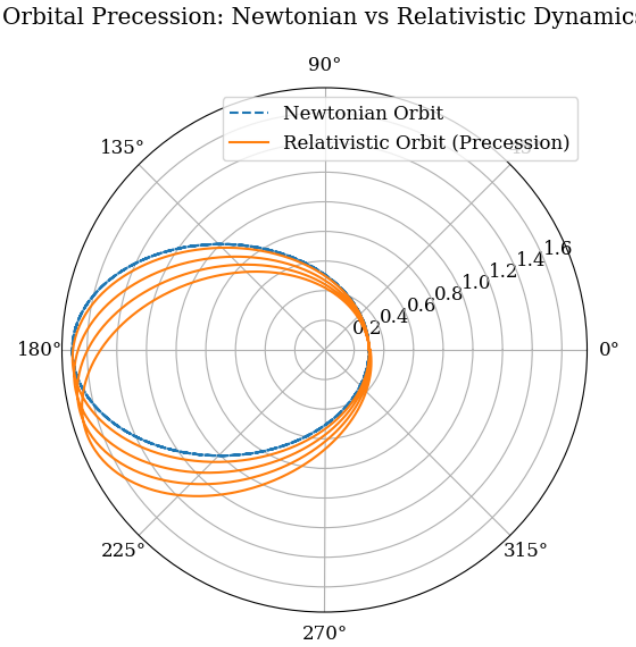

Figure 2.4: Schwarzschild Precession of the Pericentre

the mathematical treatment of orbital shapes in relativistic settings closely mirrors that of classical mechanics, permitting the use of familiar analytical techniques.

In Newtonian gravity, bound orbits generated by a central potential $\Phi = -GM/r$ take the form of conic sections with the central mass located at one of the foci. In contrast, within the Schwarzschild spacetime, test particles follow geodesics which, although qualitatively similar to classical orbits, are not closed curves and exhibit additional relativistic effects.

The pericenter, defined as the point of minimum radial distance from the central mass, behaves differently in the two frameworks. In a Newtonian inertial frame, the orientation of the pericenter remains fixed with respect to distant stars. However, in Schwarzschild geometry, the orbital ellipse undergoes a gradual rotation, leading to a precession of the pericenter over successive revolutions. The angular shift per orbit, denoted as $\Delta\theta$/revolution and illustrated in Figure 2.4, can be measured and computed explicitly. Notably, the Schwarzschild metric preserves the standard interpretation of angular coordinates, allowing this effect to be defined without ambiguity.

In the weak-field limit, the advance of the pericentre per revolution, $\Delta\omega$, is given by the well-known expression:

$$\Delta\omega \approx \frac{6\pi GM}{c^2 a(1-e^2)} \tag{2.37}$$

where a is the semi-major axis and e the orbital eccentricity. This relation highlights the strong dependence of the precession on the orbital parameters. In particular, the effect scales inversely with the semi-latus rectum $p = a(1-e^2)$, implying that the precession becomes more significant for compact orbits (small a) and highly eccentric trajectories.

As the eccentricity approaches unity ($e \to 1$), the term $(1-e^2)$ decreases rapidly, effectively amplifying the relativistic contribution. This behavior plays a crucial role in the selection of observational targets in the Galactic Center: stars on highly eccentric orbits

are expected to exhibit measurable precession over relatively short timescales, whereas the effect remains negligible for nearly circular or distant orbits.

2.4.5 Relativistic Effective Potential

The orbit architecture in General Relativity differs from that of Keplerian orbits also due to the shape of the Effective Potential. From the conservation laws[2], the equation of radial motion for a massive particle can be written in the form:

$$\frac{1}{2}\left(\frac{dr}{d\tau}\right)^2 + V_{eff}(r) = \frac{E^2 - c^4}{2c^2} \tag{2.38}$$

Where the relativistic effective potential $V_{eff}(r)$ takes the form:

$$V_{eff}(r) = -\frac{GM}{r} + \frac{L^2}{2r^2} - \frac{GML^2}{c^2 r^3} \tag{2.39}$$

The first term is the classical Newtonian attraction $(-1/r)$. The second term is the classical centrifugal barrier $(+1/r^2)$, which in Newtonian mechanics diverges positively at the origin, preventing collapse for particles with non-zero angular momentum. The third term, $-\frac{GML^2}{c^2 r^3}$, is a purely relativistic correction and because of the sign it can be seen that it is attractive. Since it depends on $-1/r^3$, at small distances it inevitably dominates over the repulsive centrifugal barrier.

This behavior creates an infinite potential well near the origin, defining two critical operating limits for space navigation. The modification of the orbital architecture compared to Newtonian mechanics is plotted in Figure 2.5, which shows the effective potential curves for different values of specific angular momentum L. The relativistic effective potential $V_{eff}(r)$ is plotted as a function of the radial distance in Schwarzschild spacetime. The curves highlight the collapse of the centrifugal barrier for low angular momentum (red line) and the presence of critical orbital thresholds (ISCO and Photon Sphere).

[2]Specific energy $E = -g_{tt}\frac{dt}{d\tau}c^2$ and specific angular momentum $L = r^2\frac{d\phi}{d\tau}$ are the conserved quantities for a massive particle moving in a Schwarzschild spacetime.

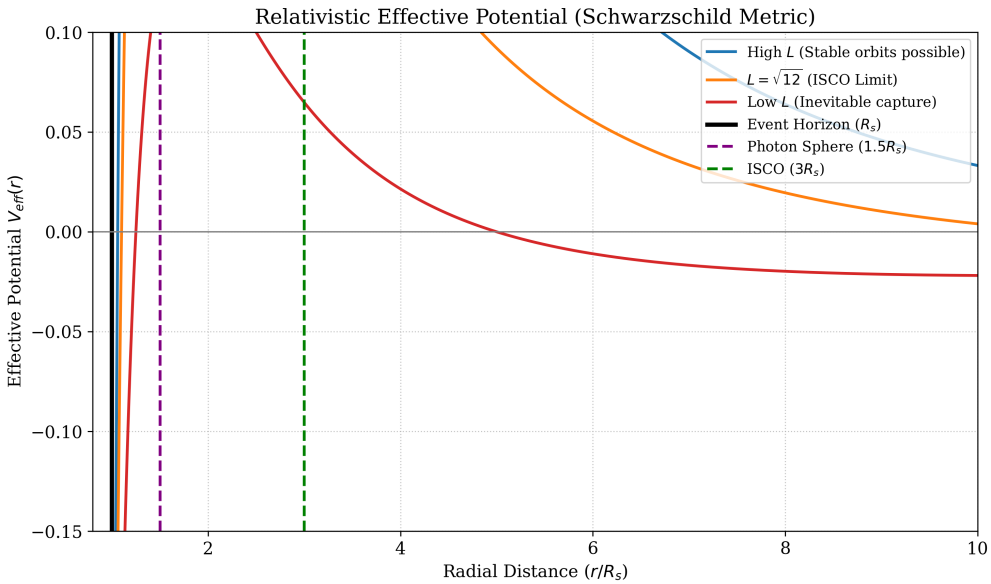

Figure 2.5: Relativistic effective potential $V_{eff}(r)$

1. **Innermost Stable Circular Orbit (ISCO):** at $r_{ISCO} = 3R_s$, the stable minimum of the potential disappears, transforming into an inflection point. Below this altitude, there are no stable circular orbits and this region takes the name of *plunge* region in which any perturbation causes immediate fall toward the black hole.

2. **Photon Sphere:** at $r_{ph} = 1.5R_s$, gravity is such that it curves photons into unstable circular orbits. For massive particles, circular orbits exist only for radii larger than the photon sphere and become unstable below the ISCO. At the photon sphere radius, only null geodesics can form circular trajectories: a massive spacecraft attempting to remain at that radius would require continuous acceleration and could not follow a geodesic trajectory as any small perturbation would lead either to escape or to inward plunge.

A schematic 2D representation of these concentric critical boundaries surrounding the central singularity is provided in Figure 2.6, which shows the sequence of critical radii derived from the Schwarzschild metric: the Event Horizon (R_s), the Photon Sphere ($1.5R_s$), and the ISCO ($3R_s$). This topological map serves as a navigational reference for the interstellar trajectories simulated in the subsequent chapters.

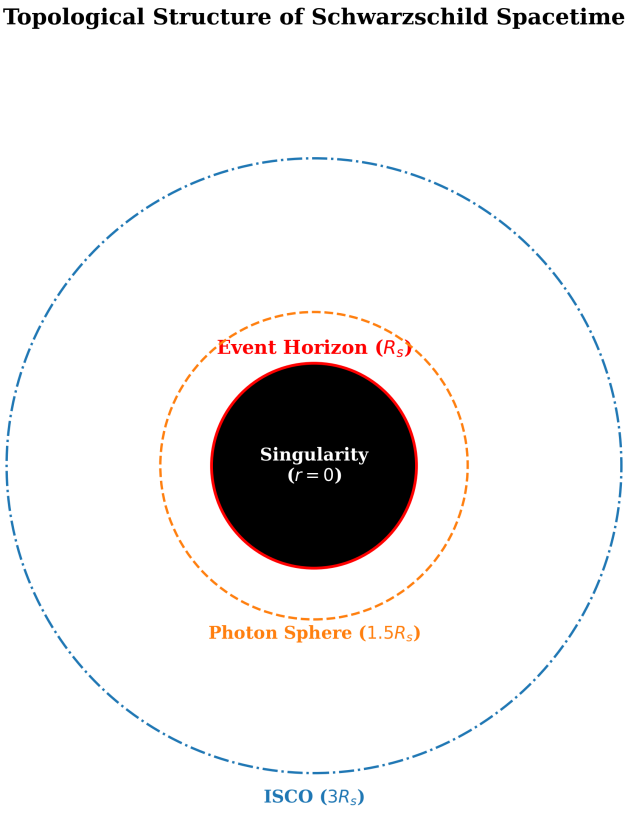

Figure 2.6: Topological anatomy of a non-rotating supermassive black hole.

2.4.6 Analysis of the Simulation Model

Table 2.1 includes the numerical values adopted for the simulation code prepared for the thesis:

Universal Gravitational Constant (G)	$6.67430 \times 10^{-11}\,\mathrm{m^3\,kg^{-1}\,s^{-2}}$
Speed of Light in Vacuum (c)	$299\,792\,458\,\mathrm{m/s}$
Sagittarius A* Mass (M_{SgrA})	$4.297 \times 10^6\,M_\odot$ [a]
Schwarzschild Radius (R_s)	$1.269 \times 10^{10}\,\mathrm{m} \approx 0.085\,\mathrm{AU}$ [b]

[a] $M_\odot \approx 1.98847 \times 10^{30}\,\mathrm{kg}$
[b] $1\,\mathrm{AU} = 1.495978707 \times 10^{11}\,\mathrm{m}$

Table 2.1: Physical parameters used in the simulation.

These values set the scales for orbital radii, time dilation, and relativistic effects in the simulation. In particular, the Schwarzschild radius defines the regime where General Relativity strongly deviates from Newtonian predictions.

2.5 Relativistic Dynamics: The Geodesic Equations

The definition of the spacetime geometric structure, formalized through the Schwarzschild metric, constitutes the substrate in which physical phenomena occur. For the space mission studied in this thesis, the focus is on the dynamics: it is necessary to determine how a space vehicle evolves within the curved manifold under the joint action of the black hole's gravitational field and the propulsive thrust.

In General Relativity, a free-falling body follows a **geodesic**, the four-dimensional straightest possible curve in curved spacetime. The motion equations are the analytical expression of these geodesic curves, eventually modified by the presence of non-gravitational forces such as thrust.

2.5.1 Relativistic State Vector and Four-Velocity

In classical mechanics, a satellite's state vector is formed by 6 components, 3 describing the position $\mathbf{r}$ and 3 the velocity $\mathbf{v}$, while time t is an absolute parameter not included in the system. In a relativistic framework, this distinction disappears: space and time become interconnected and the coordinates themselves are dynamical variables.

The position four-vector x^μ identifying an event in spacetime is

$$x^\mu = \begin{bmatrix} ct \\ r \\ \theta \\ \phi \end{bmatrix} \tag{2.40}$$

where t represents coordinate time and $\{r, \theta, \phi\}$ are the spherical coordinates. More precisely, r is the **radial coordinate**, θ is the **colatitude** or **polar angle** and ϕ is the **azimuthal angle**.

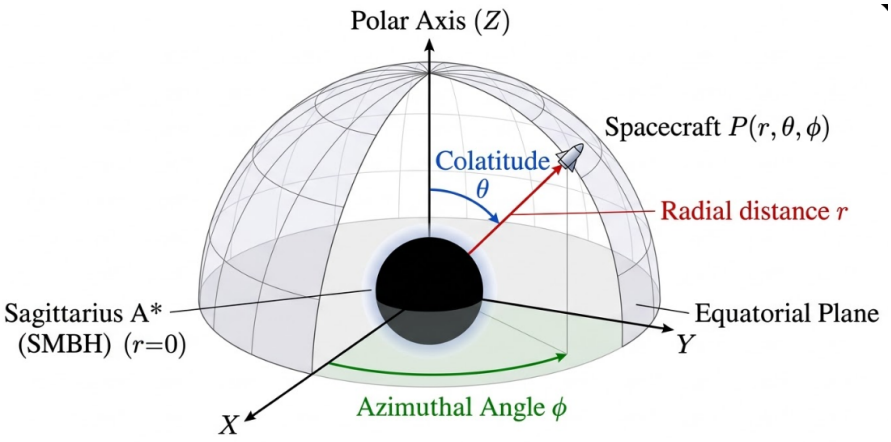

Figure 2.7: Definition of the spherical coordinate system $\{r, \theta, \phi\}$

The dynamic evolution is ruled by the four-velocity u^μ

$$u^\mu \equiv \frac{dx^\mu}{d\tau} = \begin{bmatrix} c\frac{dt}{d\tau} \\ \frac{dr}{d\tau} \\ \frac{d\theta}{d\tau} \\ \frac{d\phi}{d\tau} \end{bmatrix} \tag{2.41}$$

The spatial components u^i (with $i = 1, 2, 3$) relate to the velocity measured by a local observer, providing a physical interpretation of the motion.

The state vector that defines the dynamic system is therefore the 8-dimensional object, formed by the combination of 2.40 and 2.41

$$\mathbf{X}(\tau) = \begin{bmatrix} ct \\ r \\ \theta \\ \phi \\ c\frac{dt}{d\tau} \\ \frac{dr}{d\tau} \\ \frac{d\theta}{d\tau} \\ \frac{d\phi}{d\tau} \end{bmatrix} \tag{2.42}$$

A geometrical property of the four-velocity is that it has constant norm. Since the trajectory of a massive body is always timelike, it must satisfy

$$g_{\mu\nu} u^\mu u^\nu = -c^2 \tag{2.43}$$

Using the Schwarzschild metric, this constraint becomes

$$-\left(1 - \frac{R_s}{r}\right) c^2 \left(\frac{dt}{d\tau}\right)^2 + \left(1 - \frac{R_s}{r}\right)^{-1} \left(\frac{dr}{d\tau}\right)^2 + r^2 \left(\frac{d\theta}{d\tau}\right)^2 + r^2 \sin^2\theta \left(\frac{d\phi}{d\tau}\right)^2 = -c^2 \tag{2.44}$$

This relation represents a first integral of motion and is essential for verifying the physical consistency of the numerical integration.

2.5.2 Analytical Derivation of the Christoffel Symbols

Motion Equations in a curved manifold depend on the first derivatives of the metric tensor. In section 2.2.1 it has been explained how these variations are coded by the Levi-Civita Connection, whose components are the second species Christoffel symbols $\Gamma^\lambda_{\mu\nu}$. Their general definition 2.14, in terms of the metric tensor $g_{\mu\nu}$ and its inverse $g^{\mu\nu}$, is presented again:

$$\Gamma^\lambda_{\mu\nu} = \frac{1}{2} g^{\lambda\sigma} \left(\frac{\partial g_{\sigma\mu}}{\partial x^\nu} + \frac{\partial g_{\sigma\nu}}{\partial x^\mu} - \frac{\partial g_{\mu\nu}}{\partial x^\sigma} \right) \tag{2.45}$$

In a general four-dimensional manifold, the connection's coefficients $\Gamma^\lambda_{\mu\nu}$ are in total $4^3 = 64$. However, since Schwarzschild metric has been adopted, the properties of such geometry have to be considered and they drastically reduce the computational complexity

of the problem, making most of these terms vanish.

1. **Reduction for symmetry**: the Levi-Civita connection has no torsion, and this implies symmetry with respect to the lower indices 2.11. This reduces the components from 64 to 40.

2. **Reduction for diagonality**: Schwarzschild metric tensor is diagonal, therefore $g_{\mu\nu} = 0$ if $\mu \neq \nu$. As a consequence, the inverse tensor $g^{\lambda\sigma}$ is diagonal as well and $g^{\lambda\sigma} = 0$ if $\lambda \neq \sigma$. In the general definition sum, the only term that remains for the sum index σ is the one where $\sigma = \lambda$. Equation 2.45 can be simplified and becomes:

$$\Gamma^{\lambda}_{\mu\nu} = \frac{1}{2} g^{\lambda\lambda} \left(\frac{\partial g_{\lambda\mu}}{\partial x^{\nu}} + \frac{\partial g_{\lambda\nu}}{\partial x^{\mu}} - \frac{\partial g_{\mu\nu}}{\partial x^{\lambda}} \right) \tag{2.46}$$

3. **Space and Time Isometries**: the metric coefficients $g_{\mu\nu}$ depend only on the coordinate r. This comes from two assumptions of Schwarzschild metric:

   - Assumption of static environment: $\partial_t g_{\mu\nu} = 0$, all the derivatives with respect to coordinate time are equal to 0.
   - Assumption of Axial and Spherical Symmetry: $\partial_\phi g_{\mu\nu} = 0$ and $\partial_\theta g_{\mu\nu} = 0$, all the derivatives with respect to the latitude and azimuthal angle are equal to zero.

The combination of these three properties makes the majority of the partial derivatives equal to zero. The only Christoffel symbols that do not vanish are the ones that involve the radial coordinate r or the latitude θ. Table 2.2 depicts the 13 Christoffel symbols not equal to zero with their physical meaning:

Component	**Physical Meaning**
Temporal Connection Components $\Gamma^{t}_{\mu\nu}$	
$\Gamma^{t}_{tr} = \Gamma^{t}_{rt}$	Coupling between radial motion and time dilation
Radial Connection Components $\Gamma^{r}_{\mu\nu}$	
Γ^{r}_{tt}	Newtonian and relativistic gravitational attraction
Γ^{r}_{rr}	Radial acceleration term
$\Gamma^{r}_{\theta\theta}$, $\Gamma^{r}_{\phi\phi}$	Centrifugal inertial forces
Angular Connection Components	
$\Gamma^{\theta}_{r\theta} = \Gamma^{\theta}_{\theta r}$	Radial-angular coupling
$\Gamma^{\theta}_{\phi\phi}$	Angular curvature contribution
$\Gamma^{\phi}_{r\phi} = \Gamma^{\phi}_{\phi r}$	Radial-angular coupling
$\Gamma^{\phi}_{\theta\phi} = \Gamma^{\phi}_{\phi\theta}$	Spherical geometry contribution

Table 2.2: Non-vanishing Christoffel symbols in Schwarzschild spacetime

In the code developed for this thesis, the symbols $\Gamma^{\lambda}_{\mu\nu}$ are evaluated in their analytical expressions at each integration step. This makes it possible to solve the geodesic equation in its most general formulation. The complete list of Christoffel symbols equations defined

for the project can be found in Appendix A. Once the connection coefficients are known, the equations of motion can be explicitly constructed.

2.5.3 The Motion Equations

The fundamental equation of dynamics for a body subject to an external four-force F^μ, such as the thrust of a propulsion system, is given by the absolute covariant derivative operator:

$$\frac{Du^\mu}{d\tau} = \frac{F^\mu}{m} \tag{2.47}$$

In the absence of external forces (i.e., if $F^\mu = 0$), the equation reduces to the geodesic equation, expressing the relativistic law of inertia: free bodies move along curves that extremize proper time. The system of second-order ordinary differential equations that govern motion is evaluated by expressing the covariant derivative in terms of the ordinary derivative and the affine connection:

$$\frac{du^\mu}{d\tau} = -\Gamma^\mu_{\alpha\beta} u^\alpha u^\beta \tag{2.48}$$

In equation 2.48, by expanding the summation over the indices α and β for each μ component, the scalar motion equations are obtained, of which the most relevant for the trajectory description are explained below.

Time Evolution Equation, $\mu = u^t$

A critical aspect of General Relativity is the distinction between the two time variables that appear in the equations: proper time τ and coordinate time t. The conceptual difference between the two has been described in section 2.4.2. The mathematical dependency between τ and t is differential and it depends on the gravitational potential positioning. The conversion factor is indeed the temporal component of the 4-velocity vector u^t:

$$\frac{dt}{d\tau} \equiv u^t \tag{2.49}$$

In a circular orbit with radius r this relation simplifies into the gravitational redshift factor 2.33. The differential equation for u^t has to be integrated simultaneously with the other equations in order to evaluate the mission duration for a terrestrial observer.

This equation describes how the time coordinate varies along the trajectory. Using the first Christoffel symbol A and its symmetry, equation 2.48 becomes:

$$\frac{du^t}{d\tau} = -\frac{R_s}{r(r - R_s)} u^r u^t \tag{2.50}$$

Physically, this term relates radial velocity with time dilation. If the vehicle descends toward the black hole, the derivative is positive, indicating that u^t increases: coordinate time flows faster and faster than proper time as the vehicle approaches the horizon. This

phenomenon makes the use of τ as the integration independent parameter numerically advantageous choice to avoid computational singularities.

Radial Dynamics Equation ($\mu = r$)

This is the most complex equation, and it balances gravitational attraction, inertia, and centrifugal forces. Substituting in 2.48 the Christoffel symbols derived:

$$\frac{du^r}{d\tau} = -\frac{R_s(r-R_s)c^2}{2r^3}(u^t)^2 + \frac{R_s}{2r(r-R_s)}(u^r)^2 + (r-R_s)(u^\theta)^2 + (r-R_s)\sin^2\theta(u^\phi)^2 \quad (2.51)$$

The structure of this equation clearly shows the non-linear nature of relativistic gravity: unlike Newtonian mechanics, the velocity components themselves contribute to the effective gravitational interaction. However, it is notable how the leading term R_s/r^3 reduces to the Newtonian gravitational acceleration in the weak-field limit.

The most significant terms are:

- Gravitational term ($-\Gamma^r_{tt}$): it is proportional to c^2/r^2 and it is the dominant term, as it represents the inexorable attraction of the black hole.
- Centrifugal Term ($+\Gamma^r_{\phi\phi}$): it represents the centrifugal barrier. In classical mechanics, to prevent falling, the centrifugal force increases proportionally to $1/r^3$ as it approaches the center. In Schwarzschild, the factor $(r - R_s)$ causes the centrifugal force to vanish at the horizon ($r = R_s$): this explains why, under the ISCO[3], no amount of angular momentum can prevent collapse.

Angular Dynamics Equations ($\mu = \theta, \phi$)

The latitude and longitude equations describe the conservation of angular momentum and the precession of the orbital plane.

$$\frac{du^\theta}{d\tau} = -\frac{2}{r}u^r u^\theta + \sin\theta\cos\theta(u^\phi)^2 \quad (2.52)$$

$$\frac{du^\phi}{d\tau} = -\frac{2}{r}u^r u^\phi - 2\cot\theta u^\theta u^\phi \quad (2.53)$$

The term $-2/r(u^r u^\phi)$ is the relativistic manifestation of angular momentum conservation, or the geometrical coupling between radial and angular motion: if the radius decreases, the angular velocity u^ϕ must increase to compensate. These terms enforce conservation of angular momentum and couple radial and angular motion geometrically.

The complete system constitutes a coupled, non-linear set of ordinary differential equations. Their numerical integration provides the relativistic trajectory of the spacecraft, consistently accounting for spacetime curvature and propulsion forces, which will be explained in the next section and considered in the equations.

[3]Innermost Stable Circular Orbit - See Section 2.4.5

2.6 Thrust and Propulsive Model

The analysis carried out in Section 2.5 described the dynamics of a passive test mass, exclusively subject to the geometric curvature of spacetime induced by the black hole. However, the central objective of this thesis is the optimization of trajectories for an active spacecraft, capable of modifying its dynamic state thanks to the use of a propulsion system.

The introduction of non-gravitational thrust breaks the symmetry of geodesics: the trajectory in this case is an accelerated curve determined by the competitive interaction between the attractive gravitational field and the force exerted by the engines. Section 2.6 provides the mathematical model used to include the thrust term in the field equation.

2.6.1 Perturbed Motion Equations and Covariant Acceleration

A space vehicle that uses its thrusters and propulsion system does not follow a free geodesic and the four-velocity u^μ does not follow the curve. When an external force is introduced, equation 2.48 takes the form:

$$\frac{Du^\mu}{d\tau} \equiv \frac{du^\mu}{d\tau} + \Gamma^\mu_{\alpha\beta} u^\alpha u^\beta = a^\mu_{thrust} \tag{2.54}$$

The term a^μ_{thrust} that appears in the equation is the true **four-acceleration**, defined in spacetime and not in ordinary three-dimensional space and defined as the ratio between the four-force F^μ and the instantaneous rest mass of the vehicle $m(\tau)$.

By isolating the ordinary derivative, which is what the numerical integrator must calculate, we obtain the system of ordinary differential equations that governs the evolution of the velocity components:

$$\frac{du^\mu}{d\tau} = -\Gamma^\mu_{\alpha\beta} u^\alpha u^\beta + \frac{F^\mu_{thrust}}{m} \tag{2.55}$$

Substituting the forcing term in the geodesic equations derived, and using the calculated Christoffel symbols, the complete set of scalar equations implemented in the dynamic model is defined.

2.6.1.1 The Orthogonality Constraint

A fundamental physical property of relativistic propulsion, often overlooked in simplified discussions but essential to the consistency of the model, is that the thrust force acts purely in the three-dimensional space of the vehicle's instantaneous reference frame and it cannot alter the intrinsic rest mass of the vehicle or violate the geometric structure of spacetime.

This translates into the fact that the four-velocity u^μ must maintain a constant norm along the entire trajectory, even during propulsive maneuvers:

$$u_\mu u^\mu = g_{\mu\nu} u^\mu u^\nu = -c^2 = \text{constant} \tag{2.56}$$

Deriving this condition with respect to proper time τ, the following relation is obtained:

$$\frac{d}{d\tau}(u_\mu u^\mu) = 2u_\mu \frac{du^\mu}{d\tau} = 2u_\mu a^\mu_{total} = 0 \tag{2.57}$$

Since the total acceleration is the sum of the gravitational acceleration, which is orthogonal to the velocity by definition of geodesics, and of the propulsive acceleration, the consequence is that there is an orthogonality constraint between the four-velocity and the propulsive four-acceleration:

$$u_\mu a^\mu_{thrust} = g_{\mu\nu} u^\mu a^\nu_{thrust} = 0 \tag{2.58}$$

This constraint implies that in 4-dimension spacetime, the acceleration vector is always perpendicular to the velocity vector.

2.6.1.2 Thrust Components Calculation

The orthogonality constraint has a critical operational implication for numerical simulation.

While the three spatial components of thrust (F^r, F^θ, F^ϕ) are controllable degrees of freedom determined by the orientation of the engine nozzle in physical space, the temporal component F^t is not a free variable. It represents the energy variation necessary to maintain the relativistic consistency of motion and must be calculated algebraically at each step.

Explicitly expressing the scalar product (2.58) in the Schwarzschild diagonal metric:

$$g_{tt} u^t F^t + g_{rr} u^r F^r + g_{\theta\theta} u^\theta F^\theta + g_{\phi\phi} u^\phi F^\phi = 0 \tag{2.59}$$

From this linear relation, the analytical expression for the temporal component of the force implemented in the simulation software becomes:

$$F^t = -\frac{g_{rr} u^r F^r + g_{\theta\theta} u^\theta F^\theta + g_{\phi\phi} u^\phi F^\phi}{g_{tt} u^t} \tag{2.60}$$

Two characteristic situations can be highlighted:

1. If the vehicle is spatially stationary ($u^i = 0$), then $F^t = 0$ and the thrust acts only in space.
2. If the vehicle is in rapid motion ($u^i \neq 0$), part of the thrust is spent to change the time dilation and maintain the four-velocity on the mass shell ($u^2 = -c^2$).

The remaining variables of the force vector are:

- The direct radial thrust F^r directly counteracts the attractive gravitational term
- F^θ allows the inclination of the orbital plane to be changed, which is essential for three-dimensional transfers
- F^ϕ increases or decreases the angular momentum of the vehicle, allowing the orbit to be raised or lowered

In the system the vector $\mathbf{F} = (F^r, F^\theta, F^\phi)$ acts as an active control that allows the vehicle to escape from its natural free-fall trajectory, enabling complex maneuvers such as stationary hovering or escape from the inner region near the event horizon.

The detailed and complete set of motion equations defined for the project is listed in Appendix B.

2.6.2 Mass Variation and Propellant Dynamics

For the interstellar missions analyzed, a relativistic ΔV comparable to the speed of light is required and the application of significant thrust necessarily involves the ejection of matter at high speed, causing a continuous variation in the inertial mass of the system. In an optimal control context, the mass $m(\tau)$ ceases to be a fixed parameter and becomes a fundamental dynamic state variable, whose evolution is coupled nonlinearly to the equations of motion.

The law governing propellant consumption is the differential form of Tsiolkovsky's rocket equation[4]

In relativistic dynamics, the rest mass is not conserved when propellant is expelled, and its evolution must be explicitly modeled. In the vehicle's instantaneous reference frame, the conservation of momentum requires the mass variation to be proportional to the applied thrust and inversely proportional to the effective exhaust velocity.

The mass state equation is:

$$\frac{dm}{d\tau} = -\frac{F_T(\tau)}{c_e} = -\frac{|\mathbf{F}_{thrust}|}{I_{sp} \cdot g_0} \tag{2.61}$$

In the equation $m(\tau)$ is the instantaneous mass of the vehicle at time τ, $F_T(\tau)$ is the magnitude of the thrust applied at time τ, c_e is the Effective Exhaust Velocity and I_{sp} is the Specific Impulse of the propulsion system. g_0 is the standard acceleration due to gravity on Earth ($9.80665\,\mathrm{m/s^2}$), conventionally used to convert c_e to seconds. It is essential to note that, in this model, the derivative is calculated with respect to proper time τ: since all physical processes inside the vehicle occur according to the onboard clock, the consumption rate $\dot{m}$ is defined invariantly in the vehicle's reference frame.

2.6.2.1 Final State Vector and Operational Constraints

In the simulation software, the state vector is extended to include mass as the ninth component:

$$\mathbf{X} = \begin{bmatrix} ct \\ r \\ \theta \\ \phi \\ c\frac{dt}{d\tau} \\ \frac{dr}{d\tau} \\ \frac{d\theta}{d\tau} \\ \frac{d\phi}{d\tau} \\ m \end{bmatrix} \tag{2.62}$$

During numerical integration, the solver calculates the value of $m(\tau)$ instant by instant. The coupling between decreasing mass and increasing acceleration introduces stiffness in the system when high thrust-to-mass ratios are reached The optimal control problem must

[4] $\Delta v = c_e \ln\left(\frac{m_0}{m_f}\right)$

respect physical constraints on mass to ensure the feasibility of the solution: the physical lower limit of the mass, which includes the structure, payload, and engines, but excludes propellant is the dry mass m_{dry} and the trajectory is valid only if:

$$m(\tau_{final}) \geq m_{dry}$$

Violation of this constraint would imply the use of non-existent propellant. In conclusion, the variation in mass is not a simple accounting detail, but a primary driver of the vehicle's dynamics, determining the temporal evolution of its manoeuvrability within the gravitational well.

2.6.2.2 Dynamic Coupling and Thrust-to-Weight Ratio

The inclusion of equation (2.61) in the state system $\mathbf{X}$ introduces a critical dynamic coupling.

The equations of motion (2.55) depend on the acceleration a^μ, which is related to the force F^μ by the relation:

$$a^\mu(\tau) = \frac{F^\mu(\tau)}{m(\tau)}$$

Since $m(\tau)$ is a monotonically decreasing function as the mass can only decrease, with constant thrust provided by the engines ($F_T = \text{const}$), the resulting acceleration increases over time. This phenomenon has operational implications for the mission:

1. Final Efficiency: in the final phases of the maneuver, when the vehicle is almost empty and its mass almost equals the dry mass, the available acceleration is maximum.

2. Optimization: the optimal control solver will exploit this feature, tending to place the most expensive maneuvers (requiring high ΔV) in the phases when the vehicle is lightest, maximizing the effectiveness of the thrust.

The propulsion model therefore transforms the problem from pure geodesic motion into a fully controlled relativistic optimal control system.

2.6.3 Advanced Propulsion: Magnetic Confinement Fusion

The selection of the propulsion system for an interstellar mission in the Galactic Center cannot be based on conventional chemical technologies. To achieve a relativistic ΔV, it is necessary to access energy densities six orders of magnitude higher (TJ/kg), which are exclusive domain of nuclear reactions. This is because chemical bonds release energies on the order of $\sim 10^6$ J/kg, which is insufficient to accelerate macroscopic spacecraft to relativistic velocities. Nuclear reactions, on the other hand, release energies on the order of $\sim 10^{12}$ J/kg, making interstellar missions theoretically feasible. The physical model adopted in this thesis hypothesizes the use of a Magnetic Confinement Fusion (MCF) propulsion system, based on a Direct Fusion Drive (DFD) architecture.

Reactor Architecture and Plasma Physics

The Direct Fusion Drive (DFD) is designed to extract kinetic energy from charged fusion products directly using a magnetic nozzle, avoiding intermediate energy conversion to electricity. Magnetic Confinement Fusion (MCF) uses strong magnetic fields to confine a high-temperature plasma, typically above 10^8 K, preventing contact with reactor walls and sustaining the fusion reaction.

The heart of the propulsion system is a cylindrical reaction chamber where the fuel plasma is heated to temperatures of approximately 10^8 K. To prevent destructive contact between the plasma and the structural walls, a high-intensity magnetic field generated by high-temperature superconducting (HTS) coils is used. The magnetic configuration, typically a mirror configuration or a field reversed configuration (FRC), traps the charged particles along the field lines. The nuclear reaction of reference for space propulsion is aneutronic, preferably Deuterium-Helium3 (D-^3He):

$$^2H +^3 He \rightarrow^4 He\,(3.6\,\mathrm{MeV}) + p\,(14.7\,\mathrm{MeV})$$

This choice is dictated by two physical advantages over Deuterium-Tritium fusion:

- Charged Products: The reaction products (alpha particles and protons) are both electrically charged. This means that their kinetic energy can be manipulated directly by magnetic fields to generate thrust, without going through intermediate thermal cycles.
- Reduced Neutron Radiation: The low neutron production reduces the need for heavy shielding mass, improving the vehicle's thrust-to-weight ratio.

Despite such advantages, it is important to note that ^{3}He is scarce on Earth, so practical implementation would require extraterrestrial sourcing.

Magnetic Nozzle

The component that transforms the reactor into a rocket engine is the Magnetic Nozzle. While in a chemical rocket, the de Laval nozzle converts the thermal energy of a neutral gas into kinetic energy via solid walls, in a fusion engine, the million-degree plasma temperatures would vaporize any solid material. Instead, the magnetic nozzle uses diverging magnetic field lines to guide the expansion of the plasma. The process occurs in three stages:

1. **Confinement**: In the throat of the nozzle, the magnetic field is at its maximum, compressing the plasma.
2. **Expansion**: The hot particles spiral along the expanding field lines, converting their perpendicular thermal energy ($W_\perp$) into parallel kinetic energy ($W_\parallel$) thanks to the conservation of adiabatic magnetic momentum ($\mu = W_\perp/B = \text{const}$).
3. **Detachment**: For the thrust to be effective, the plasma must detach from the closed magnetic field lines of the vehicle. This occurs through magnetic reconnection

mechanisms or high-speed inertial effects. Plasma detachment has been demonstrated only in small-scale laboratory experiments (e.g., FRC experiments at the Princeton Plasma Physics Laboratory) and remains a critical technical challenge.

To translate these complex plasma physics mechanisms into an engineering architecture, Figure 2.8 illustrates the conceptual schematic of a Direct Fusion Drive (DFD) based on a Field-Reversed Configuration (FRC), highlighting the magnetic nozzle geometry.

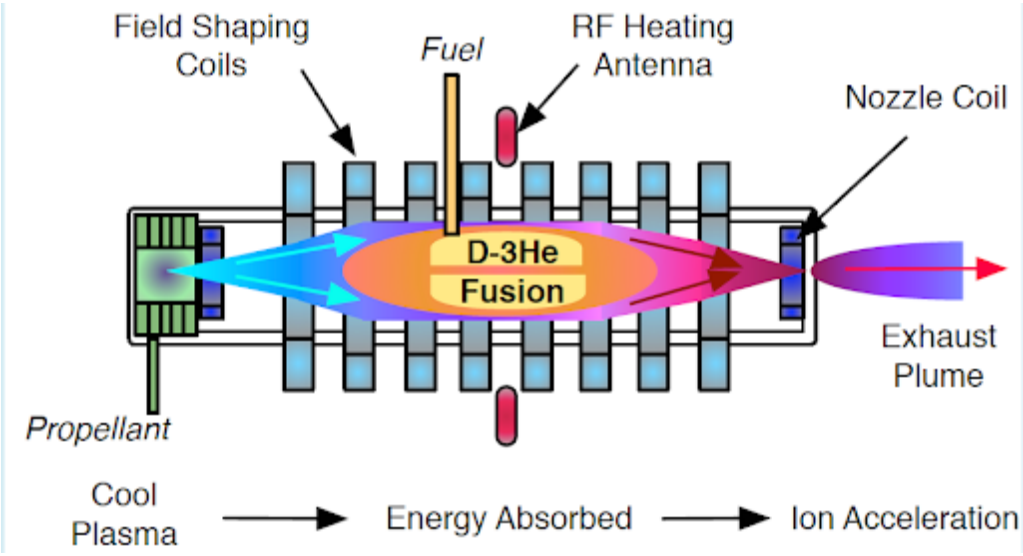

Figure 2.8: Conceptual schematic of a Direct Fusion Drive utilizing a Field-Reversed Configuration

The diagram illustrates the closed magnetic field lines confining the high-temperature fusion plasma in the central core, and the open field lines forming the magnetic nozzle. Thrust is generated as the charged reaction products are directed axially outwards through the nozzle, converting thermal energy into directed kinetic energy. Image adapted from Princeton Plasma Physics Laboratory (PPPL) research.

Performance Parameters

The performance of the propulsion system is not unlimited, but is determined by the physical constraints of nuclear reaction and the engineering limitations of the confinement system. Based on the data implemented in the simulation model, the following operating parameters are defined:

Effective Exhaust Velocity (c_e)
Ejection velocity is determined by the thermal energy of the fusion particles. The direct products of the reaction have velocities of approximately of the order of $0.08c$ for alpha ions in D-^{3}He, however, the model assumes an optimal compromise value for the interstellar mission in exam:

$$c_e = 0.05, c \tag{2.63}$$

This value, equal to 5% of the speed of light, represents the theoretical upper limit for controlled thermonuclear fusion systems intended for human flight, ensuring a balance between propulsive efficiency and power density.

Specific Impulse (I_{sp})

The specific impulse, that is the primary indicator of propellant efficiency, is derived directly from the exhaust velocity:

$$I_{sp} = c_e/g_0 \approx 1.53 \times 10^6, \mathrm{s} \tag{2.64}$$

This value, which is three orders of magnitude higher than that of electric ion thrusters is the sine qua non for making relativistic rocket equations feasible. A lower I_{sp} would require prohibitive initial mass ratios (m_0/m_f), tending exponentially towards infinity.

Maximum Acceleration (a_{thrust})

Unlike chemical propulsion, capable of high acceleration for short periods, fusion propulsion is limited by the specific power of the cooling system and the mass of the superconducting magnets. The vehicle is modeled as a continuous low thrust system, with a maximum design acceleration set at:

$$a_{max} = 0.05\mathrm{m/s}^2 \quad (\approx 5 \times 10^{-3}, g) \tag{2.65}$$

Although modest, this acceleration is sufficient to accumulate relativistic velocity over interstellar timescales. The integration of a constant acceleration of $0.05\,\mathrm{m/s}^2$ over time allows a significant ΔV to be reached, making the deep regions of the gravitational potential of Sgr A* accessible.

To provide a clear reference for the numerical simulations presented in the following chapters, Table 2.3 summarizes the nominal performance specifications assumed for the spacecraft's fusion propulsion system.

Propulsion Parameter	**Symbol**	**Design Value**
Propulsion Architecture	-	Direct Fusion Drive (MCF / FRC)
Nuclear Reaction	-	D-^{3}He (Aneutronic)
Effective Exhaust Velocity	c_e	$0.05\,c$
Specific Impulse	I_{sp}	$\approx 1.53 \times 10^6\,\mathrm{s}$
Maximum Continuous Acceleration	a_{max}	$0.05\,\mathrm{m/s}^2$

Table 2.3: Nominal performance parameters for the advanced fusion propulsion system used in the astrodynamics simulation.

Experimental Basis and Limitations

The propulsion concepts described here are based on the following experimental and conceptual researches:

- MIT Plasma Science and Fusion Center (PSFC) studies on DFD and aneutronic fusion
- Princeton Plasma Physics Laboratory (PPPL) experiments on FRC demonstrating high-temperature plasma confinement and preliminary magnetic nozzle concepts
- NASA concept studies on Direct Fusion Drive for deep-space missions

While theoretically robust, the system remains hypothetical, as net-positive power from aneutronic fusion has not yet been achieved. This chapter therefore presents an informed framework for interstellar propulsion, rather than an immediately realizable design.

Chapter 3

Optimal Control Theory

When trying to connect an initial spacetime state to a final one, there exists an infinite number of trajectories that are mathematically valid and capable of doing so. However, the real challenge is to find the solution that not only gets to the target, but that also takes into account all the aspects that distinguish an inefficient sub-optimal transfer from an optimal one. The optimization and evaluation of low-thrust trajectories necessary to complete an interstellar mission will remain a main pillar in astrodynamics research, in particular due to strong constraints imposed by propellant limitations during a mission.

An Optimal Control Problem (OCP) has the objective of finding the specific control law capable of optimizing a merit index that can provide a maximization or minimization of the imposed objective. In the mission scenario studied in this thesis, the optimal trajectory is defined as the one that minimizes propellant consumption during the transfer, and, because of the mass conservation principle, this is equivalent to saying that one wants to maximize the spacecraft's final mass, given an initial mass m_i. The principle lies in the fact that certain active parameters, such as magnitude or three-dimensional orientation of the thrust vector, directly influence the dynamic evolution of the system and therefore, such parameters must be appropriately and continuously adjusted along the entire trajectory. The scope of the OCP is to determine the optimal evolution of the control variables which satisfies the physical and geometrical boundary constraints, while maximizing the performance index. The whole set of time variables takes the name of "optimal control law" and to ensure that the solution found is the optimal solution, the work draws on the fundamentals of Optimal Control Theory (OCT).

3.1 Numerical approach: Direct vs Indirect Methods

To solve an optimal control problem in analytical form is generally limited to linear or extremely simplified dynamic systems. When considering space trajectory optimization, with its highly nonlinear gravitational models and operational constraints, the use of numerical procedures becomes necessary and such numerical solution strategies can be divided into two large families: direct and indirect methods. Although years of algorithmic developments and international competitions have demonstrated that both can successfully solve highly complex mission scenarios, statistically and according to literature reviews,

there is a neat preference for direct approaches. In fact, in contemporary trajectory optimization practice, direct methods are widely adopted and implemented in many software packages, while just few implement indirect methods. This trend is justified by the greater architectural accessibility and flexibility of the first approach. Direct Methods transform the Optimal Control Problem into a Non-Linear Programming (NLP) Problem by discretizing on a temporal mesh both the evolution of state variables and the time-history of controls. The nodes on the grid represent the optimization variables and then the NLP problem is solved with the advantage of being extremely robust because they avoid the explicit derivation of adjoint equations from the calculus of variations. This mathematical simplicity generates high computational costs because in order to obtain a solution that closely approximates the real dynamics the discretization grid must be refined, leading to problems with tens or hundreds of thousands of variables. Furthermore, the direct approach returns purely numerical and parametric results, typically providing less physical insight of the nature and causes of the solution's optimality.

On the other hand, Indirect Methods (IM) are based on the application of Calculus of Variations (CoV) and the Optimal Control Theory and, instead of discretizing it, the problem is transformed into a Two-Point Boundary Value Problem (TPBVP) by introducing auxiliary variables, named adjoint variables. There are several advantages in using this approach: first, the solutions obtained are very accurate, computational cost and time of execution are lower compared to direct methods and, above all, theoretical insights that help to understand the examined problem and guide the user toward the globally optimal solution are provided. However, indirect methods involve mathematical, numerical and implementation challenges as well: the analytical derivation of the added differential equations and control laws is demanding and dependent on the specific problem. Moreover, the nature of the TPBVP drastically restricts the convergence range and makes the solution very sensitive to the initial guess values provided for the adjoint variables and this initialization requires several attempts and considerable user experience.

3.1.1 The Choice of Indirect Methods for Relativistic Regimes

Academic research and studies published over the years have led to the development of robust indirect architectures. One of the key innovations has been the ability to manage control discontinuities by introducing internal temporal boundaries and structuring the problem as a Multi-Point Boundary Value Problem (MPBVP). This hybrid approach has extended the applicability of indirect methods to scenarios that were previously exclusive domain of direct methods.

The choice of using an indirect method for the subject of this thesis is not dictated just by methodological continuity, but by physical necessity: in fact, the integration of trajectories in curved space-time around a supermassive black hole such as Sagittarius A* requires mathematical precision, primarily because of the highly non-linear quantities that vary with extreme gradients as they approach the event horizon. In such a strong-field gravity regime, a direct method may introduce approximation errors between one node and another that could result in discretization errors and poor preservation of the postulates of

General Relativity, like the failure to conserve the four-velocity norm.

The indirect method, on the other hand, by coupling the complete 9-component state vector with its respective 9 added variables, requires the dynamics to be evaluated using pure and continuous step-by-step differential integration. The use of variable-step integration algorithms ensures that spacetime curvature is followed in a strictly continuous manner with respect to proper time τ. In this framework, the optimality of the control law is not the product of a numerical approximation, but an analytical result, linked to the tensor architecture of the Schwarzschild metric.

3.2 Optimal Control Theory

The Optimal Control Theory applied to the resolution of Optimal Control Problems for space trajectories has been deeply analyzed in literature, with the first formulations applied to astrodynamics in the 1950s attributed to Lawden, and followed by the treatises on optimal control written by Kirk, Bryson, and Burghes. The key principles of Optimal Control Theory have their roots in the Calculus of Variations, a branch of mathematics whose origins are attributed to Euler with his publication "Elementa Calculi Variationum" in 1766. Although variational fundamentals represent milestones in the scientific area, in recent times they have been readapted and extended to fully use the computational power of modern computers and manage increasingly sophisticated numerical architectures.

As briefly mentioned, an Optimal Control Problem aims at defining the control law that minimizes (or maximizes) a specific performance index. This search does not happen in a free space, but it has to identify the optimal trajectory among all the physical possible ones, that satisfies a set of dynamic constraints and that governs the evolution of a system from an initial state to the final target. Unlike static optimization, OCT operates in an infinite-dimensional function space, since the unknown quantity of the problem is a continuous function. The following sections outline the general mathematical framework of OCT, formulated independently of the specific relativistic dynamics that will be addressed later.

3.2.1 Dynamic System and Constraints Definition

An OCP preliminary defines a set of Ordinary Differential Equations (ODE) of first order to describe the temporal evolution of the system. At each instant, the state vector $\mathbf{x}(t) \in \mathbb{R}^n$ determines the system's state. The ODEs depend on the state vector itself between initial and final state, but they also depend on a specific control vector $\mathbf{u}(t) \in \mathbb{R}^m$, that has m different active variables that are the degree of freedom on which one can intervene. The evolution of the dynamic system, with t being the independent variable, is expressed by the following system of non-linear differential equations:

$$\dot{\mathbf{x}}(t) = \mathbf{f}(\mathbf{x}(t), \mathbf{u}(t), t) \tag{3.1}$$

In general, a space trajectory does not evolve in an open domain but is instead defined by imposed temporal conditions. The trajectory extremes, evaluated at the initial time t_0

and final instant t_f, are the problem's external boundaries and the optimal trajectories between such points is subject to geometric and temporal restrictions. Rigid conditions on the state quantities at the extremes, such as the position and velocity to guarantee rendez-vous, as well as constraints on the epochs may be imposed. The full set of Boundary Conditions (BC) can be mathematically grouped into a vector $\boldsymbol{\chi}$:

$$\boldsymbol{\chi}(\mathbf{x}_0, \mathbf{x}_f, t_0, t_f) = 0 \tag{3.2}$$

In equation 3.2 the operator $\boldsymbol{\chi} : [\mathbb{R}^n, \mathbb{R}^n, \mathbb{R}, \mathbb{R}] \rightarrow \mathbb{R}^q$ established all the different constraints q imposed to the problem. The control vector $\mathbf{u}(t)$ may also be constrained, as some of its quantities may be bounded in a specific range of admissible controls, or minimum and maximum values. Such limits define a closed space of acceptable controls, stated as $\mathfrak{U}$ ($\mathbf{u} \in \mathfrak{U}$). The optimality of the OCP, and so the criteria according to which a particular trajectory and control law are the best among the others, is evaluated through the merit index $\mathcal{J}$. The problem becomes the research of relative maximum or minimum values of the function. The most complete and general formulation is known as the Bolza Problem

$$\mathcal{J} = \varphi(\mathbf{x}_0, \mathbf{x}_f, t_0, t_f) + \int_{t_0}^{t_f} \left[\Phi(\mathbf{x}(t), \mathbf{u}(t), t)\right] dt \tag{3.3}$$

The merit index is composed of two terms:

- A scalar function φ, named cost or **Mayer function**, that depends on the values of the state variables and time evaluated at the external boundaries. This function quantifies how much the final state reached is close to the target.
- The second is an integral term of the scalar function Φ, called the **Lagrange term**, which depends continuously on the values that the state variables, the controls and time itself take throughout the maneuver. It calculates the cost, for example the propellant consumption, over the entire trajectory that connects initial and final state.

The following notation is introduced for the sake of brevity:

$$\begin{aligned} \varphi &\triangleq \varphi(\mathbf{x}_0, \mathbf{x}_f, t_0, t_f) \\ \boldsymbol{\chi} &\triangleq \boldsymbol{\chi}(\mathbf{x}_0, \mathbf{x}_f, t_0, t_f) \end{aligned} \tag{3.4}$$

3.2.2 Augmented Merit Index and Hamiltonian

At this point the basis of Indirect Methods become relevant, as minimizing the equation directly is not convenient. For this reason, the optimality conditions are established by defining an **augmented merit function** $\mathcal{J}^*$, that adds to the original functional a measurement of how much the geometric boundary constraints and the differential equations are satisfied.

This operation is completed by introducing two sets of unknown multipliers

1. The **adjoint variables** grouped in the continuous vector $\boldsymbol{\lambda}(t) \in \mathbb{R}^n$, are univocally associated to the differential state equations

2. The **Lagrange multipliers**, grouped in the constant vector $\boldsymbol{\mu} \in \mathbb{R}^q$, are associated to the algebraic-geometric boundary constraints $\boldsymbol{\chi}$

The augmented merit index takes the form written in equation 3.5

$$\mathcal{J}^* = \varphi + \boldsymbol{\mu}^T \boldsymbol{\chi} + \int_{t_0}^{t_f} \left[\Phi + \boldsymbol{\lambda}^T (\mathbf{f} - \dot{\mathbf{x}}) \right] dt \tag{3.5}$$

Both functionals depend on the state variables $\mathbf{x}(t)$, on their time derivatives $\dot{\mathbf{x}}(t)$ and on the control variables $\mathbf{u}(t)$. If one considers a non-converging generic solution, with the motion equations and limits not respected, the added terms do not vanish. However, when the solution is dynamically coherent and it respects both the boundary conditions and the state equations, so $\boldsymbol{\chi} = 0$ and $\mathbf{f} = \dot{\mathbf{x}}$, the difference between $\mathbf{f}$ and $mat\dot{h}bfx$ is equal to zero at each instant and the two merit indexes are equivalent ($\mathcal{J} = \mathcal{J}^*$). As a consequence, solving the non-bounded problem for the augmented index is equal to solving the original bounded problem.

Since the time derivatives of the state variables $\dot{\mathbf{x}}$ are integrated at each step of the optimization and they represent unknown elements, their presence inside the integral is an obstacle to the evaluation of variational conditions, so it is useful to isolate and eliminate them by integrating by parts the linear term $-\boldsymbol{\lambda}^T \dot{\mathbf{x}}$

$$\int_{t_0}^{t_f} -(\boldsymbol{\lambda}^T \dot{\mathbf{x}}) dt = -(\boldsymbol{\lambda}_f^T \mathbf{x}_f) + (\boldsymbol{\lambda}_0^T \mathbf{x}_0) + \int_{t_0}^{t_f} \left(\dot{\boldsymbol{\lambda}}^T \mathbf{x} \right) dt \tag{3.6}$$

By substituting the result of 3.6 inside equation 3.5, the following is obtained:

$$\mathcal{J}^* = \varphi + \boldsymbol{\mu}^T \boldsymbol{\chi} + (\boldsymbol{\lambda}_0^T \mathbf{x}_0 - \boldsymbol{\lambda}_f^T \mathbf{x}_f) + \int_{t_0}^{t_f} \left(\Phi + \boldsymbol{\lambda}^T \mathbf{f} - \dot{\boldsymbol{\lambda}}^T \mathbf{x} \right) dt \tag{3.7}$$

An essential quantity for the entire Optimal Control Theory architecture appears inside equation 3.7: the system's Hamiltonian $\mathcal{H}$.

$$\mathcal{H} \triangleq \Phi + \boldsymbol{\lambda}^T \mathbf{f} \tag{3.8}$$

The Hamiltonian 3.8 depicts the Lagrange cost term and the product between the adjoint variable vector and the dynamic equations and its introduction allows to write the final compact form of the augmented merit index

$$\mathcal{J}^* = \varphi + \boldsymbol{\mu}^T \boldsymbol{\chi} + (\boldsymbol{\lambda}_0^T \mathbf{x}_0 - \boldsymbol{\lambda}_f^T \mathbf{x}_f) + \int_{t_0}^{t_f} (\mathcal{H} - \dot{\boldsymbol{\lambda}}^T \mathbf{x}) dt \tag{3.9}$$

Maximizing (or minimizing) the merit index $\mathcal{J}^*$ implies strict imposition of the mathematical condition necessary for optimality, which states that the function $\mathcal{J}^*$ must be stationary at the optimum point. Its first-order variation $\delta\mathcal{J}^*$ generated by arbitrary perturbations on states, controls, and times must be strictly equal to zero. The application of the variational operator δ to the entire expression of $\mathcal{J}^*$ is a long and complex process, governed by Leibniz's rule for differentiation under the integral sign with variable limits.

The complete first-order differentiation is obtained by performing the necessary algebraic steps and collecting similar terms:

$$\begin{aligned}\delta\mathcal{J}^* = &\left(\frac{\partial\varphi}{\partial t_0} + \boldsymbol{\mu}^T\frac{\partial\boldsymbol{\chi}}{\partial t_0} - \mathcal{H}_0\right)\delta t_0 + \\ &+ \left(\frac{\partial\varphi}{\partial t_f} + \boldsymbol{\mu}^T\frac{\partial\boldsymbol{\chi}}{\partial t_f} + \mathcal{H}_f\right)\delta t_f + \\ &+ \left(\frac{\partial\varphi}{\partial \mathbf{x}_0} + \boldsymbol{\mu}^T\frac{\partial\boldsymbol{\chi}}{\partial \mathbf{x}_0} + \boldsymbol{\lambda}_0^T\right)\delta\mathbf{x}_0 + \\ &+ \left(\frac{\partial\varphi}{\partial \mathbf{x}_f} + \boldsymbol{\mu}^T\frac{\partial\boldsymbol{\chi}}{\partial \mathbf{x}_f} - \boldsymbol{\lambda}_f^T\right)\delta\mathbf{x}_f + \\ &+ \int_{t_0}^{t_f}\left[\left(\frac{\partial\mathcal{H}}{\partial\mathbf{x}} + \dot{\boldsymbol{\lambda}}^T\right)\delta\mathbf{x} + \frac{\partial\mathcal{H}}{\partial\mathbf{u}}\delta\mathbf{u}\right]dt\end{aligned} \tag{3.10}$$

The mathematical and physical meaning behind equation 3.10 is that, when choosing adequate adjoint variables $\boldsymbol{\lambda}$ and Lagrange multipliers $\boldsymbol{\mu}$ the global variation $\delta\mathcal{J}^*$ vanishes for every independent and arbitrary choice of the virtual variaton $\delta t_0, \delta t_f, \delta\mathbf{x}_0, \delta\mathbf{x}_f, \delta\mathbf{x}, \delta\mathbf{u}$. The only possibility so that the sum results equal to zero for independent variation is that all the coefficients that multiply such variations are simultaneously equal to zero. The annulment of each specific term in the equation generates a distinct and well-defined set of differential and algebraic conditions that completely govern the optimization problem. In the following sections, the so-called transversality and boundary optimality conditions that result from setting the terms evaluated at the extreme boundaries to zero and the Euler-Lagrange equations and control conditions resulting from setting the integral to zero will be analyzed.

3.2.3 Boundary Conditions for Optimality and Transversality

The boundary conditions are formed by the set of equations that rule how time and states behave at the extreme points of the trajectory. They derive from the systematic cancellation of the multiplication coefficients of the boundary variations $\delta t_0, \delta t_f, \delta\mathbf{x}_0$ and $\delta\mathbf{x}_f$ in the variational equation 3.10. This procedure produces four key equations:

$$\frac{\partial\varphi}{\partial t_0} + \boldsymbol{\mu}^T\frac{\partial\boldsymbol{\chi}}{\partial t_0} - \mathcal{H}_0 = 0 \tag{3.11a}$$

$$\frac{\partial\varphi}{\partial t_f} + \boldsymbol{\mu}^T\frac{\partial\boldsymbol{\chi}}{\partial t_f} + \mathcal{H}_f = 0 \tag{3.11b}$$

$$\frac{\partial\varphi}{\partial \mathbf{x}_0} + \boldsymbol{\mu}^T\frac{\partial\boldsymbol{\chi}}{\partial \mathbf{x}_0} + \boldsymbol{\lambda}_0^T = 0 \tag{3.11c}$$

$$\frac{\partial\varphi}{\partial \mathbf{x}_f} + \boldsymbol{\mu}^T\frac{\partial\boldsymbol{\chi}}{\partial \mathbf{x}_f} - \boldsymbol{\lambda}_f^T = 0 \tag{3.11d}$$

Equation 3.11a and 3.11b represent the **Transversality Conditions** for the time variable and one can see that if time does not appear within the terminal cost function φ and is not constrained within the vector $\boldsymbol{\chi}$, then the partial derivatives are zero. It follows

that the value of the Hamiltonian evaluated at that point, for both the initial and final time, must be strictly zero. In this scenario, the value of time assumed at the edges will depend directly on the optimization algorithm that will determine the ideal value to maximize performance. On the other hand, if time is physically constrained, i.e., if equations of the type $t_0 = a$ and/or $t_f = b$ exist in the vector $\boldsymbol{\chi}$, the presence of the multiplier $\boldsymbol{\mu}$ prevents the sum from being canceled. In this case, the associated Hamiltonian is free, and its value will be determined solely by optimization.

A classic application example is that of missions with a rigidly fixed duration Δt: in these, there is an assigned initial epoch t_0 and a consequent final epoch $t_f = t_0 + \Delta t$ that is equally rigid. In a similar scenario, $\mathcal{H}_0 \neq 0$ and $\mathcal{H}_f \neq 0$ will necessarily result. For a mission with an unconstrained end time, where only t_0 is assigned, we will have $\mathcal{H}_0 \neq 0$ while the free end time t_f will result in $\mathcal{H}_f = 0$.

The last two equations 3.11c and 3.11d define the **Optimality Conditions** on the bounds. They establish that if a given i-th state variable $\mathbf{x}_i$ does not appear in the function φ nor in any operational constraint, its associated variation is free and, for the sum to be zero, the corresponding added variable must be zero at the same point, $\lambda_{\mathbf{x}_i} = 0$. Otherwise, if the state $\mathbf{x}_i$ is rigidly imposed, its associated adjoint variable will be unconstrained at the extreme.

3.2.4 Adjoint Variables Equations and Control Variables

The set of ordinary differential equations obtained by nullifying the multiplying coefficients in the last line of equation 3.10 describes how adjoint variables and controls evolve over time. By imposing that the coefficient $\delta\mathbf{x}$ is equal to zero, one finds the Eulero-Lagrange equations for the adjoint variables:

$$\dot{\boldsymbol{\lambda}} = -\left(\frac{\partial \mathcal{H}}{\partial \mathbf{x}}\right)^T \tag{3.12}$$

Since the adjoint variable are univocally associated to the respective dynamic state variable, the adjoint variable' derivative vector is of the same size, so $\dot{\boldsymbol{\lambda}} \in \mathbb{R}^n$. These equations define the adjoint variable as sensitivity indexes: the time variation of the marginal cost is dictated by how much the local Hamiltonian depends on the state at that precise moment.

At the same time, by nullifying the multiplicative coefficient of the control variation $\delta\mathbf{u}$, a set of m fundamental algebraic equations is identified for the optimization of the controls themselves:

$$\frac{\partial \mathcal{H}}{\partial \mathbf{u}} = 0 \tag{3.13}$$

In its most general form, one or more elements of the control vector cannot assume infinite values, but must be confined within specified admissibility limits, indicated by $\mathfrak{U}$. In the space propulsion scenario, for example, only explicit constraints are taken into consideration: a specific control quantity u must be strictly maintained within the structural boundaries $\mathfrak{U}_{min} \leq u \leq \mathfrak{U}_{max}$.

From this point, the standard minimization formulation of the functional $\mathcal{J}$ is assumed; therefore, the point maximization of the Hamiltonian is imposed. In fact, in the presence of explicit admissibility constraints, the optimal control $u^* \in \mathfrak{U}$ sought to generate the ideal trajectory is solely that which, for each individual point belonging to the trajectory, locally maximizes the value of the Hamiltonian function at that precise space-time instant.

This universal principle is known in literature as the **Pontryagin Maximum (or minimum) Principle (PMP)**. The PMP does not imply that a control must always be pushed and maintained at the extreme limits of its admissibility spectrum; the generic optimal control value is the analytical value provided if the latter respects $\mathfrak{U}_{min} < u < \mathfrak{U}_{max}$, thus unbounded, otherwise it is coercively set at the operating extremes allowed by $\mathfrak{U}$.

It is worth noting that there is a critical exception: the classical differential condition of stationarity for control cannot hold if the Hamiltonian function is intrinsically linear with respect to the control variable analyzed. In this mathematical architecture, the partial derivative degenerates, generating two conceptually distinct cases:

$$\frac{\partial \mathcal{H}}{\partial u_i} = \begin{cases} k_{u_i} & \text{if } \mathcal{H} \text{ is affine wrt } u_i \\ f(u_i) & \text{otherwise} \end{cases} \tag{3.14}$$

Where k_{u_i} represents a parameter depending only on states and adjoint variables, but not on the control. If the Hamiltonian is affine to the control, the equality to zero cannot be reached in any case inside the operation interval, with the exception of $k_{u_i} = 0$. In such scenario, the solution strategy becomes one that depends on the sign and entity of the coefficient k_{u_i}.

In particular, if $k_{u_i} \neq 0$ the Hamiltonian is maximized by forcing the control to continuously acquire the maximum technically admissible value, $u_i = \mathfrak{U}_{i,max}$ if the coefficient is positive ($k_{u_i} > 0$, or the minimum conceivable value, $u_i = \mathfrak{U}_{i,min}$ if the coefficient is negative ($k_{u_i} < 0$).

This condition is internationally recognized as **Bang-Bang** control and represents the behavior of low-thrust propulsion in an OCP. The Hamiltonian is affine to the selected control variable (the thrust magnitude T), and the algorithm will impose the sudden switching between the extreme admitted values for T_{min} (i.e., shutdown, 0) and the nominal peak T_{max} according to the evolution of the function.

Finally, in the event that $k_{u_i} = 0$ for a finite time interval, it is necessary to pursue an analytical strategy of a differential nature suitable for deriving the so-called switching function with respect to time. Such eventualities involve the physical occurrence of singular arcs, which, however, do not occur in the interstellar regime under consideration and will therefore not be discussed further.

3.3 Multi-Point Optimal Control Problem

The classic formulation discussed in section 3.2 reduces the trajectory optimization to a Two-Point Boundary Value Problem. If one has q boundary conditions on the external bound $\boldsymbol{\chi}$, the problem generates a closed system of equations derived from the transversality,

optimality and control conditions, which determine the initial and final time, the initial values for the ODEs and the adjoint variables associated to the Lagrange multipliers.

However, the direct application of a TPBVP to a realistic space mission, and in particular to a dynamically extreme environment such as the gravitational potential of Sagittarius A*, presents severe numerical challenges. The presence of inequality constraints on the thrust modulus induces a Bang-Bang control law. If the numerical integrator were tasked with discovering moment by moment whether to switch the thruster on or off by evaluating the sign of the switching function $\mathcal{S}_F$, the solver would find itself dealing with discontinuities. If $\mathcal{S}_F$ oscillates around zero, the gradients calculated during optimization would be ill-conditioned, preventing the indirect method from converging. This criticality is not theoretical but purely numerical, as the presence of discontinuities in the control law degrades the regularity properties required by indirect shooting algorithms.

To avoid this intrinsic instability and improve the robustness of the software architecture, the TPBVP is reformulated using a multiple shooting approach, which leads to a Multi-Point Boundary Value Problem (MPBVP).

This formulation corresponds to the multiple shooting method, in which the trajectory is segmented into several arcs whose initial conditions are treated as optimization variables and enforced to satisfy continuity constraints. The fundamental assumption of MPBVP is that the control structure is preset while the durations and transition states remain unknown. The entire trajectory is divided into a discrete number n_p of sub-intervals, referred to as arcs, and, within each arc, the state variables and adjoint variables evolve in a strictly continuous manner, while at the internal boundaries, jumps, discontinuities, or specific constraints can be managed. In the context of this thesis, the internal boundaries physically coincide with thrust on/off events.

From a notational point of view, the generic j-th arc begins at the time $t_{(j-1)_+}$ and ends at time t_{j_-}. Consequently, the state vectors evaluated at the ends of this specific arc are denoted as $\mathbf{x}_{(j-1)_+}$ and $\mathbf{x}_{j_-}$, respectively.

Each arc j extends for its own time duration Δt_j, which is not a fixed parameter but constitutes an optimization variable of the problem:

$$\Delta t_j = t_{j_-} - t_{(j-1)_+} \tag{3.15}$$

The resulting system is therefore not a simple TPBVP replicated for each arc, but a nonlinear coupled system and it comprises: the state and adjoint variable ODEs on each phase, the jump conditions at the internal nodes, the external boundary constraints, and the unknown time durations.

In this architecture the boundary conditions, which acquire a mixed and nonlinear nature as they can be imposed not only at the external points but also at any internal boundary, take the expanded vector form

$$\boldsymbol{\chi}\left(\mathbf{x}_{(j-1)_+}, \mathbf{x}_{j_-}, t_{(j-1)_+}, t_{j_-}\right) = 0 \quad \text{for } j = 1, \ldots, n_p \tag{3.16}$$

These equations include, for example, physical continuity constraints: the state of the spacecraft at the end of the thrust arc must coincide exactly with the state at the beginning

of the next arc ($\mathbf{x}_{j_-} - \mathbf{x}_{j_+} = 0$).

3.3.1 The Functional and Variations in the Multi-Point Domain

The extension to the multi-point domain requires a reformulation of the cost functional $\mathcal{J}$. The merit index is no longer a single integral from end to end, but becomes the sum of the cost integrals evaluated arc by arc:

$$\mathcal{J} = \varphi\left(\mathbf{x}_0, \mathbf{x}_f, t_0, t_f\right) + \sum_{j=1}^{n_p} \int_{t_{(j-1)_+}}^{t_{j_-}} \Phi\left(\mathbf{x}(t), \mathbf{u}(t), t\right) dt \tag{3.17}$$

Following the same variational paradigm outlined for TPBVP, the augmented merit function $\mathcal{J}^*$ incorporates the multipoint constraints through the Lagrange multipliers $\boldsymbol{\mu}$, and the equations of dynamics through the added vectors $\boldsymbol{\lambda}(t)$, defined on each individual arc:

$$\mathcal{J}^* = \varphi + \boldsymbol{\mu}^T \boldsymbol{\chi} + \sum_{j=1}^{n_p} \int_{t_{(j-1)_+}}^{t_{j_-}} \left[\Phi + \boldsymbol{\lambda}^T \left(\mathbf{f} - \dot{\mathbf{x}}\right)\right] dt \tag{3.18}$$

To obtain the optimality conditions, it is necessary to integrate by parts the differential term $-\boldsymbol{\lambda}^T \dot{\mathbf{X}}$:

$$\mathcal{J}^* = \varphi + \boldsymbol{\mu}^T \boldsymbol{\chi} + \sum_{j=1}^{n_p} \left(\boldsymbol{\lambda}_{(j-1)_+}^T \mathbf{x}_{(j-1)_+} - \boldsymbol{\lambda}_{j_-}^T \mathbf{x}_{j_-}\right) + \sum_{j=1}^{n_p} \int_{t_{(j-1)_+}}^{t_{j_-}} \left(\mathcal{H} - \dot{\boldsymbol{\lambda}}^T \mathbf{x}\right) dt \tag{3.19}$$

where the Hamiltonian $\mathcal{H}$ maintains its definition $\mathcal{H} = \Phi + \boldsymbol{\lambda}^T \mathbf{f}$ unchanged for every point in the arc.

Within each open interval $(t_{(j-1)_+}, t_{j_-})$, the state and adjoint variables satisfy the canonical Hamiltonian equations:

$$\begin{aligned} \dot{\mathbf{x}} &= \frac{\partial \mathcal{H}}{\partial \boldsymbol{\lambda}} \\ \dot{\boldsymbol{\lambda}} &= -\frac{\partial \mathcal{H}}{\partial \mathbf{x}} \end{aligned} \tag{3.20}$$

Applying the stationarity principle and calculating the first-order differentiation $\delta\mathcal{J}^*$ for the multi-phase structure, the variational equation breaks down into several contributions evaluated near each junction. The overall variation for each j-th arc becomes:

$$
\begin{aligned}
\delta\mathcal{J}^* = &\left(\frac{\partial\varphi}{\partial t_{(j-1)_+}} + \boldsymbol{\mu}^T\frac{\partial\boldsymbol{\chi}}{\partial t_{(j-1)_+}} - \mathcal{H}_{(j-1)_+}\right)\delta t_{(j-1)_+} + \\
&+\left(\frac{\partial\varphi}{\partial t_{j_-}} + \boldsymbol{\mu}^T\frac{\partial\boldsymbol{\chi}}{\partial t_{j_-}} + \mathcal{H}_{j_-}\right)\delta t_{j_-} + \\
&+\left(\frac{\partial\varphi}{\partial \mathbf{x}_{(j-1)_+}} + \boldsymbol{\mu}^T\frac{\partial\boldsymbol{\chi}}{\partial \mathbf{x}_{(j-1)_+}} + \boldsymbol{\lambda}^T_{(j-1)_+}\right)\delta\mathbf{x}_{(j-1)_+} + \\
&+\left(\frac{\partial\varphi}{\partial \mathbf{x}_{j_-}} + \boldsymbol{\mu}^T\frac{\partial\boldsymbol{\chi}}{\partial \mathbf{x}_{j_-}} - \boldsymbol{\lambda}^T_{j_-}\right)\delta\mathbf{x}_{j_-} + \\
&+\sum_{j=1}^{n_p}\int_{t_{(j-1)_+}}^{t_{j_-}}\left[\left(\frac{\partial\mathcal{H}}{\partial\mathbf{x}} + \dot{\boldsymbol{\lambda}}\right)\delta\mathbf{x} + \frac{\partial\mathcal{H}}{\partial\mathbf{u}}\delta\mathbf{u}\right]dt, \quad \text{for } j = 1,\ldots,n_p
\end{aligned}
\tag{3.21}
$$

The explicit form of equation (3.21) has an important theoretical value for the development of the numerical algorithm. Since the variations of the variables in the internal nodes are intrinsically independent unless they are connected by a constraint, the cancellation of $\delta\mathcal{J}^*$ generates the so-called Jump Conditions. More precisely, in the absence of explicit connection constraints, the variations $\delta\mathbf{X}_{j_-}$ and $\delta\mathbf{X}_{j_+}$ must be treated as independent in the variational development; any continuity relations are subsequently imposed via the constraint equations $\boldsymbol{\chi} = 0$. By grouping the terms in a manner more convenient for computational implementation, instead of considering the single arc from $t_{(j-1)_+}$ to t_{j_-}, the boundary itself is considered and values immediately before and after the boundary are written as

$$
\begin{aligned}
&\frac{\partial\varphi}{\partial t_{j_+}} + \boldsymbol{\mu}^T\frac{\partial\boldsymbol{\chi}}{\partial t_{j_+}} - \mathcal{H}_{j_+} = 0 \quad \text{for } j = 0,\ldots,n_p-1 \\
&\frac{\partial\varphi}{\partial t_{j_-}} + \boldsymbol{\mu}^T\frac{\partial\boldsymbol{\chi}}{\partial t_{j_-}} + \mathcal{H}_{j_-} = 0 \quad \text{for } j = 1,\ldots,n_p \\
&\frac{\partial\varphi}{\partial \mathbf{x}_{j_+}} + \boldsymbol{\mu}^T\frac{\partial\boldsymbol{\chi}}{\partial \mathbf{x}_{j_+}} + \boldsymbol{\lambda}^T_{j_+} = 0 \quad \text{for } j = 0,\ldots,n_p-1 \\
&\frac{\partial\varphi}{\partial \mathbf{x}_{j_-}} + \boldsymbol{\mu}^T\frac{\partial\boldsymbol{\chi}}{\partial \mathbf{x}_{j_-}} - \boldsymbol{\lambda}^T_{j_-} = 0 \quad \text{for } j = 1,\ldots,n_p
\end{aligned}
\tag{3.22}
$$

These equations govern how the states, and even more critically the adjoint variables $\boldsymbol{\lambda}$, must behave at the instant when the thruster is turned on or off. Considerations on Euler-Lagrange equations for the adjoints and control equations remain valid in the MPBVP domain. It is worth noting that the set of differential equations on each arc, together with the jump conditions, external boundary conditions, and time constraints, constitutes a system of coupled nonlinear equations whose solutions satisfy the necessary conditions for first-order optimality in the sense of Pontryagin's Maximum Principle.

3.4 The Implemented Boundary Value Problem

This section describes the numerical implementation of the Boundary Value Problem (BVP) using the fundamentals of Optimal Control Theory outlined. Optimizing the trajectory of a spacecraft governed by a low-thrust continuous propulsion system within

an extreme gravitational field, described by the Schwarzschild metric, poses formidable computational challenges. When using Indirect Methods, particular care is needed to ensure the robustness of the code due to the extremely high sensitivity of the solution to variations in the initial conditions. The dynamic system is in fact very sensitive and highly non-linear and slight perturbations in the starting parameters can lead to trajectories that rapidly diverge. As discussed, subdividing the trajectory into operational arcs (MPBVP) offers great advantages, stabilizing the management of thrust magnitude and fixing the Bang-Bang control structure. The application of OCT converts the original problem into an augmented BVP, in which the physical state variables $\mathbf{x}(t)$ are coupled to the unknown adjoint variables $\boldsymbol{\lambda}(t)$. The objective of the solver is to find the optimal augmented initial state $\mathbf{y}_0^* = \left\{ (\mathbf{x}^*)^T \, (\boldsymbol{\lambda}^*)^T \right\}^T$ that allows the trajectory to evolve dynamically until it reaches the desired final condition $\mathbf{y}_f^*$, simultaneously satisfying all BCs, both the imposed and the optimality ones. The numerical method chosen for this thesis is a differential single shooting algorithm, appreciated for its straightforward implementation, speed of execution, and low computational cost once up and running. One of the most insidious numerical obstacles of indirect methods applied to multiphase problems comes from handling arc boundaries. Since the duration of each phase Δt_j is an unknown parameter subject to optimization, the integration limits for each arc vary continuously with each iteration of the solver. If this non-linearity is not handled properly, the problem becomes severely ill-conditioned, quickly leading to singularities in the Jacobian matrix. To bypass this obstacle and normalize the integration domain, a new independent variable is introduced: the non-dimensional time t_ϵ. For the generic j-th arc the linear transformation is defined as:

$$t_\epsilon = (j-1) + \frac{t - t_{(j-1)}}{t_j - t_{(j-1)}} = (j-1) + \frac{t - t_{(j-1)}}{\Delta t_j} \tag{3.23}$$

Where

$$\Delta t_j = t_j - t_{j-1} \quad \text{for } j = 1, \ldots, n_p \tag{3.24}$$

While the physical interval Δt_j remains an unknown to be optimized, the adoption of t_ϵ fixes the boundaries of numerical integration to exact integer values. This particular parameterization makes the solution process more robust and flexible, decoupling the numerical advancement of the integrator from the actual duration in seconds of the spatial maneuver.

The general form of the complete set of Ordinary Differential Equations for the indirect method, combining states and adjoint variables in the vector $\mathbf{y}(t)$, is:

$$\frac{d\mathbf{y}}{dt} = \mathbf{f}(\mathbf{y}(t), t) \tag{3.25}$$

However, the problem may also include constant parameters that have to be optimized and, by introducing a global design vector $\mathbf{z} = \left\{ \mathbf{y}^T, \mathbf{c}^T \right\}^T$ that also includes the constants vector $\mathbf{c}$ and performing a variable change independent of t to t_ϵ, the new set of ODEs to be integrated becomes:

$$\frac{d\tilde{\mathbf{z}}}{dt_\epsilon} = \mathbf{f}\left(\tilde{z}(t_\epsilon), t_\epsilon\right) \tag{3.26}$$

and

$$\frac{d\tilde{\mathbf{y}}}{dt_\epsilon} = \Delta t_j \cdot \frac{d\mathbf{y}(t)}{dt} \tag{3.27}$$

$$\frac{d\tilde{\mathbf{c}}}{dt_\epsilon} = 0 \tag{3.28}$$

The new complete set of boundary conditions, which includes the constraints imposed by the mission, the internal continuity constraints, and the optimality conditions, can be expressed in compact form as:

$$\boldsymbol{\chi}(\tilde{\mathbf{s}}) = 0 \tag{3.29}$$

where $\tilde{\mathbf{s}}$ is a vector containing the values assumed by all variables at each internal and external boundary (e.g., at $t_\epsilon = 0, 1, \ldots, n_p$):

$$\tilde{\mathbf{s}} = \left[\tilde{\mathbf{y}}_0^T, \tilde{\mathbf{y}}_1^T, \ldots, \tilde{\mathbf{y}}_{n_p-1}^T, \tilde{\mathbf{y}}_{n_p}^T, \tilde{\mathbf{c}}^T\right]^T \tag{3.30}$$

The core of the problem consists in finding the optimal initial values of the unknown design vector $\tilde{\mathbf{q}}_0^*$ such that the integration of the system produces final conditions that cancel the error vector, thus $\boldsymbol{\chi}(\tilde{\mathbf{q}}^*) = 0$. The single shooting algorithm proceeds iteratively: at the r-th step, a guess vector $\tilde{\mathbf{q}}_r = \tilde{\mathbf{z}}_0$ is provided to the system, the system is integrated and the error at the boundaries $\boldsymbol{\chi}(\tilde{\mathbf{q}}_r)$ is evaluated.

To update the starting vector and get closer to the solution, the error at the next step $r+1$ is expanded using a first-order Taylor series:

$$\boldsymbol{\chi}(\tilde{\mathbf{q}}_{r+1}) = \boldsymbol{\chi}\left(\tilde{\mathbf{q}}_r\right) + \frac{\partial \boldsymbol{\chi}(\tilde{\mathbf{q}}_r)}{\partial \tilde{\mathbf{q}}_{r+1}}\left(\tilde{\mathbf{q}}_{r+1} - \tilde{\mathbf{q}}_r\right) \tag{3.31}$$

The matrix of partial derivatives of the constraint vector with respect to the initial free variable vector is called the Jacobian matrix $\tilde{\mathbf{J}}$. Isolating $\tilde{\mathbf{q}}_{r+1}$, the classic Newton-Raphson iterative update rule is obtained

$$\tilde{\mathbf{q}}_{r+1} = \tilde{\mathbf{q}}_r - \left[\tilde{\mathbf{J}}\left(\boldsymbol{\chi}\left(\tilde{\mathbf{q}}_r\right)\right)\right]^{-1} \boldsymbol{\chi}(\tilde{\mathbf{q}}_r) \tag{3.32}$$

The Jacobian is calculated by applying the chain rule:

$$\tilde{\mathbf{J}}\left(\boldsymbol{\chi}\left(\tilde{\mathbf{q}}_r\right)\right) = \frac{\partial \boldsymbol{\chi}\left(\tilde{\mathbf{q}}_r\right)}{\partial \tilde{\mathbf{q}}_r} = \frac{\partial \boldsymbol{\chi}\left(\tilde{\mathbf{q}}_r\right)}{\partial \tilde{\mathbf{s}}_r}\frac{\partial \tilde{\mathbf{s}}_r}{\partial \tilde{\mathbf{q}}_r} \tag{3.33}$$

The first matrix on the right side of the equal sign is a simple algebraic calculation, since it only involves the derivatives of the constraints with respect to the states at the nodes. The second matrix, which is computationally expensive, describes how an infinitesimal variation in the initial conditions propagates over time and influences the states at subsequent nodes. This matrix is known as the State Transition Matrix (STM), denoted by $\tilde{\boldsymbol{\Phi}}$. Let t_{ϵ_0} be the initial nondimensional time and $t_\epsilon \geq t_{\epsilon_0}$ a generic forward-in non-dimensional time value.

The STM has the form

$$\tilde{\mathbf{\Phi}}(t_\epsilon, t_{\epsilon_0}) = \frac{\partial \tilde{\mathbf{z}}_r}{\partial \tilde{\mathbf{q}}_{r+1}} \tag{3.34}$$

It is not a constant but evolves dynamically along with the trajectory and is governed by its own differential equation:

$$\begin{aligned} \frac{d}{dt_\epsilon}\tilde{\mathbf{\Phi}}\left(t_\epsilon, t_{\epsilon_0}\right) &= \frac{d}{dt_\epsilon}\left(\frac{\partial \tilde{\ddagger}}{\partial \tilde{\ddagger}_0}\right) \\ &= \frac{\partial}{\partial \tilde{\mathbf{z}}_0}\left(\frac{d\tilde{\mathbf{z}}}{dt_\epsilon}\right) \\ &= \frac{\partial \dot{\tilde{\ddagger}}}{\partial \tilde{\ddagger}}\frac{\partial \tilde{\ddagger}}{\partial \tilde{\ddagger}_0} \\ &= \mathbf{A}(t_\epsilon)\tilde{\mathbf{\Phi}}(t_\epsilon, t_{\epsilon_0}) \end{aligned} \tag{3.35}$$

The STM is an identity matrix at the initial time $\tilde{\mathbf{\Phi}}(t_\epsilon, t_{\epsilon_0}) = \mathbf{I}$. The matrix $\tilde{\mathbf{A}}$ contains the complete Jacobian of the dynamic system, and includes the cross partial derivatives of the states $\mathbf{x}$ with respect to the variables $\boldsymbol{\lambda}$ and vice versa. The simultaneous integration of the set of basic equations (3.26) and the STM tensor (3.35) constitutes the computational core of the solver. The integration implements an implicit multi-step numerical method with variable step size and order based on the Adams-Moulton formulations as described by Shampine and Gordon.

The use of linear mapping provided by STM inevitably generates errors during the iterative process of the Differential Corrector (DC). To increase robustness, two techniques are implemented within the iterative cycle:

1. Relaxation Factor (κ_1): The update of the starting vector is damped by introducing a coefficient $\kappa_1 \in (0, 1]$, suitable to guarantee convergence:

$$\tilde{\mathbf{z}}_{r+1} = \tilde{\mathbf{z}}_r - \kappa_1 \cdot \left[\tilde{\mathbf{J}}\left(\boldsymbol{\chi}\left(\tilde{\mathbf{q}}_r\right)\right)\right]^{-1} \boldsymbol{\chi}(\tilde{\mathbf{q}}_r) \tag{3.36}$$

   Low values of κ_1 prevent the solver from "exploding" when the initial guess is rough, ensuring more conservative steps. As the solution enters a stable neighbourhood of the global optimum, the value of κ_1 is increased toward unity to accelerate convergence.

2. Error Control and Bisection: at each update attempt, the maximum error on the constraints $E_{max} = \max_i(\chi_i)$ is evaluated. To accept the new step, it is required that the error must not grow uncontrollably with respect to the previous iteration:

$$E_{max,r+1} < \kappa_2 \cdot E_{max,r} \tag{3.37}$$

   where $\kappa_2 \in [2, 3]$ allows the algorithm to cross temporary increases in the residual, if necessary to find the descent direction. If this safeguard condition is violated, the step just taken is rejected and a bisection is imposed on the correction factor κ_1, forcing the solver to advance more conservatively along the surface of the Hamiltonian.

3.5 OCP in Relativistic Regimes

Until now, Optimal Control Theory was presented in its most general form, defining the conditions necessary for optimality regardless of the underlying dynamic system. In this concluding section, the variational mathematical framework is explicitly applied to the astrodynamics domain core of this thesis: the optimization of low-thrust propelled interstellar trajectories within the extreme gravitational field described by the Schwarzschild metric. Unlike classical Newtonian orbital mechanics, in which time is an absolute parameter and the state vector has 7 components (position, velocity, and mass), relativistic navigation imposes a dimensional leap. The evolution of the spacecraft occurs along proper time τ and is governed by a 9-component state vector $\mathbf{X}(\tau)$: the four space-time coordinates, the four components of four-velocity, and the inertial mass. The solution to this specific Optimal Control Problem requires the formulation of the Hamiltonian Boundary Value Problem (HBVP): first it is necessary to derive the optimal control law, defining the temporal evolution of the thrust magnitude F and its optimal spatial direction $\mathbf{d}$, so as to maximize the final mass at the convergence of the TPBVP.

3.5.1 Augmented State Vector and Relativistic Hamiltonian

The primary dynamic system is defined by the state vector:

$$\mathbf{X} = \begin{bmatrix} t \\ r \\ \theta \\ \phi \\ u^t \\ u^r \\ u^\theta \\ u^\phi \\ m \end{bmatrix} \tag{3.38}$$

Applying the Indirect Method, each physical variable is uniquely associated with an additional variable, generating the vector of adjoint variables $\boldsymbol{\lambda}(\tau) \in \mathbb{R}^9$:

$$\boldsymbol{\lambda} = \begin{bmatrix} \lambda_t \\ \lambda_r \\ \lambda_\theta \\ \lambda_\phi \\ \lambda_{u^t} \\ \lambda_{u^r} \\ \lambda_{u^\theta} \\ \lambda_{u^\phi} \\ \lambda_m \end{bmatrix} \tag{3.39}$$

Thus, the augmented vector $\mathbf{y}(\tau) \in \mathbb{R}^{2n}$ is

$$\mathbf{y} = \Big\{t,\, r,\, \theta,\, \phi,\, u^t,\, u^r,\, u^\theta,\, u^\phi,\, m,\, \lambda_t,\, \lambda_r,\, \lambda_\theta,\, \lambda_\phi,\, \lambda_{u^t},\, \lambda_{u^r},\, \lambda_{u^\theta},\, \lambda_{u^\phi},\, \lambda_m\Big\}^T \tag{3.40}$$

In accordance with Mayer's formulation of maximizing the final mass only, with integral cost term $\Phi = 0$, the Hamiltonian function $\mathcal{H}$ of the system is defined as the scalar product between vector 3.39 and the time derivatives with respect to τ of the state vector 3.38

$$\mathcal{H} = \boldsymbol{\lambda}^T \dot{\mathbf{X}} = \lambda_t \dot{t} + \lambda_r \dot{r} + \lambda_\theta \dot{\theta} + \lambda_\phi \dot{\phi} + \lambda_{u^t} \dot{u}^t + \lambda_{u^r} \dot{u}^r + \lambda_{u^\theta} \dot{u}^\theta + \lambda_{u^\phi} \dot{u}^\phi + \lambda_m \dot{m} \tag{3.41}$$

By substituting the equation obtained in chapter 2, one can derive the explicit form of equation 3.41.

Unlike Newtonian models in which the three spatial thrust components are completely free, in General Relativity the applied force must preserve the invariance of rest mass and the norm of four-velocity. This imposes the orthogonality constraint $u_\alpha f^\alpha = 0$, which, when applied to the Schwarzschild metric, determines an unavoidable algebraic link for the temporal component of the thrust:

$$f^t = -\frac{g_{rr} u^r f^r + g_{\theta\theta} u^\theta f^\theta + g_{\phi\phi} u^\phi f^\phi}{g_{tt} u^t} \tag{3.42}$$

Substituting this exact expression into the Hamiltonian, considering only the terms subject to thrust, and grouping the terms with respect to the three independent spatial components of the force (f^r, f^θ, f^ϕ), one has

$$\begin{aligned} \mathcal{H}_{thrust} = & \frac{1}{m}\Bigg[f^r \left(\lambda_{u^r} - \lambda_{u^t} \frac{g_{rr} u^r}{g_{tt} u^t}\right) \lambda_{u^r} + \\ & + f^\theta \left(\lambda_{u^\theta} - \lambda_{u^t} \frac{g_{\theta\theta} u^\theta}{g_{tt} u^t}\right) \lambda_{u^\theta} + \\ & + f^\phi \left(\lambda_{u^\phi} - \lambda_{u^t} \frac{g_{\phi\phi} u^\phi}{g_{tt} u^t}\right) \lambda_{u^\phi} \Bigg] - \\ & - \lambda_m \frac{F}{c_e} \end{aligned} \tag{3.43}$$

The terms in square brackets, which pair the velocity components with the mixed terms resulting from time dilation, constitute the covariant components of the **Relativistic Primer Vector**, denoted as $\lambda_V = [\lambda_{u^r}, \lambda_{u^\theta}, \lambda_{u^\phi}]^T$. The Primer Vector, originally introduced by Lawden for classical gravity, takes on a generalized form here that incorporates curved geometry and it represents the direction towards which it is most convenient, in terms of mass savings, to accelerate.

3.5.2 Optimal Direction and Switching Function

If the spatial force vector is expressed as the product of its modulus F (limited between 0 and T_{max}) and a directional unit vector $\mathbf{d}$ ($f^i = Fd^i$), the control Hamiltonian becomes

$$\mathcal{H}_{thrust} = F\left[\frac{1}{m}(\lambda_{\mathbf{V}} \cdot \mathbf{d}) - \frac{\lambda_m}{c_e}\right] \tag{3.44}$$

To maximize this quantity in accordance with the PMP, the thrust direction $\mathbf{d}$ must be perfectly aligned and parallel to the Primer Vector λ_V at every instant. Under these conditions of optimal alignment, the scalar product $\lambda_V \cdot \mathbf{d}$ collapses into the modulus of the Primer Vector itself, which is indicated by the variable Pv ($Pv \equiv \|\lambda_V\|$). Replacing the optimal orientation condition, the Hamiltonian evaluated for the optimal direction becomes a function purely affine to the magnitude of the thrust F and one can define the Switching Function $\mathcal{S}_\mathcal{F}$

$$\mathcal{S}_\mathcal{F} = \frac{1}{m}\lambda_V - \frac{\lambda_m}{c_e} \tag{3.45}$$

Since $\mathcal{H}^*_{thrust}$ is linear with respect to F, the PMP imposes the strict Bang-Bang control logic discussed:

- **Thrust Arc**: If $\mathcal{S}_\mathcal{F} > 0$, the Hamiltonian is maximized by setting $F = T_{max}$. The gravitational benefit measured by Pv/m exceeds the cost associated with mass consumption λ_m/c_e.
- **Coast Arc**: If $\mathcal{S}_\mathcal{F} < 0$, the Hamiltonian is maximized by setting $F = 0$. Propellant consumption would penalize the mission more than thrust in that region of space would help the trajectory.

3.5.3 Differential Equations for Relativistic Adjoint Variables

The BVP architecture concludes with the identification of the ordinary differential equations for the evolution of the adjoint variables, derived using the variational relation $\dot{\lambda}_i = -\frac{\partial \mathcal{H}}{\partial x_i}$. The differential equations for the adjoint variables are deeply coupled and highly nonlinear. Their calculation, implemented explicitly in the simulation algorithm, requires the analytical evaluation of the gradients of the Christoffel symbols with respect to the spatial coordinates.

The complete list of adjoint equations can be found in Appendix C The final system, consisting of 9 equations for the states and 9 equations for the adjoint variables, evaluated iteratively using the shooting method described, constitutes the "physical-mathematical engine" that guides the propelled vehicle in search of the optimal transfer trajectory through the deformed space-time of Sagittarius A*. Strict implementation of Pontryagin's Maximum Principle requires the propulsion system to be switched on or off as soon as the switching function $\mathcal{S}_\mathcal{F}$ (Eq. 3.45) crosses zero. However, if during numerical integration the value of $\mathcal{S}_\mathcal{F}$ were to exhibit small fluctuations around zero, or change sign multiple times in rapid succession, severe numerical instabilities could arise. Slight perturbations in the initial conditions, generated during the differential correction process, could shift the switching function, potentially eliminating a necessary thrust phase or introducing an

undesirable ballistic arc. If this were to occur even for just a few integration steps, the error gradients calculated by the State Transition Matrix would be corrupted, precluding the convergence of the solver.

The management of such discontinuities represents one of the most debated open challenges in indirect optimization. Modern literature proposes various techniques to avoid the problem, including smoothing approaches, homotopy and continuation methods, or control regularization techniques. In this study, a different operational strategy has been adopted to preserve the absolute precision of the metric. The switching structure is specified a priori, intrinsically transforming the problem into the MPBVP. Initially, the simplest operational structure is assumed (e.g., a single thrust arc followed by a coasting arc), and the algorithm does not decide whether to turn on the engine but only optimizes the unknown durations $\Delta\tau_j$ of the preset phases. Additional boundary conditions force the function $\mathcal{S}_\mathcal{F}$ to be exactly zero at the predefined internal nodes (the switch points). This structural constraint becomes an indispensable requirement in the strong gravity regime of Sagittarius A* and the extremely high non-linearity of Christoffel symbols greatly increases computational times in the case of structural uncertainties.

By fixing the logical sequence, the algorithm becomes exponentially more robust, avoiding infinite loops if the trajectory is, for example, at the decision boundary between a single or double ignition maneuver. Operationally, the search for the global optimum proceeds through a posteriori validation: once the solver has provided the convergent trajectory for the imposed structure, the trend of the function $\mathcal{S}_\mathcal{F}$ is inspected. If the calculated function complies with the logic imposed by the PMP (i.e., $\mathcal{S}_\mathcal{F} > 0$ only during the declared thrust arcs), the solution obtained is strictly optimal. If, on the other hand, $\mathcal{S}_\mathcal{F}$ suggests a violation and inspection suggests modifying the initial strategy, adding a new thrust phase to the MPBVP and quickly relaunching the simulation towards the true optimum.

3.6 Computational Framework: OCULUS

The computational implementation of the Optimal Control Theory, particularly when working with non-linear relativistic equations, requires a robust software architecture. As explained in this chapter, the weak point of Indirect Methods is the sensitivity of the solver with respect to the initial guesses for the adjoint variables. With no physical meaning as for position or mass, the incorrect initialization of these variables makes the STM diverge, with the consequent possibility of setting off a trial-and-error process.

To definitively overcome this operational bottleneck and ensure rapid and reliable convergence, the entire numerical apparatus and validation of the models developed in this thesis made use of OCULUS (Optimal Control with User-friendly Layout Unified Solver), an advanced unified and visual solver developed by Dr. Luigi Mascolo, designed specifically to address Optimal Control Problems using Indirect Methods.

3.6.1 Architecture and Automation of Initial Guess

The OCULUS architecture was created with the aim of breaking down the historical rigidity of variational methods, providing an interactive interface capable of drastically streamlining the configuration and resolution of both Two-Point Boundary Value Problems and Multi-Point Boundary Value Problems. The software is structured to handle dynamic models featuring Bang-Bang controls or predefined sequences of switching arcs. A key feature of OCULUS lies in its dynamic self-populating database: during simulation campaigns, the software systematically stores every single convergent solution obtained. Using this historical data as a basis for interpolation and numerical continuation (homotopy) techniques, the solver is able to autonomously generate extremely accurate initial guesses for the new boundary conditions. This mechanism transforms an originally unstable problem into a fluid and quasi-automated process, allowing entire families of trajectories to be explored and mapped with minimal computational cost.

3.6.2 Validation of the Relativistic Model

In the specific context of this master's thesis, OCULUS was not relegated to the role of a simple "black box," but was chosen as a fundamental test bed for the algorithm and physical model developed. The integration of the 9-state Schwarzschild metric dynamics, plus the related 9 adjoint variables, fulfilled three crucial tasks in the OCULUS environment:

1. Variational Validation (Euler-Lagrange Equations): The ordinary differential equations governing the evolution of the adjoint variables require the analytical calculation of the spatial gradients of the Christoffel symbols ($\partial\Gamma/\partial x^i$). The OCULUS infrastructure allowed for a rigorous comparison of manual algebraic derivations with the propagation of the solver's gradients, certifying the absolute correctness of the mathematical framework.

2. Stability in Strong Gravity Regime: The profound non-linearity of space-time near the event horizon of Sagittarius A* was tamed by exploiting OCULUS' robust algorithms for the calculation and iterative updating of the Jacobian in the Single Shooting Method, preventing the numerical divergences typical of the relativistic domain.

3. Verification of Pontryagin's Principle: The visual interface of the solver allowed for immediate and graphical inspection of the evolution of the Switching Function $\mathcal{S}_{\mathcal{F}}$ and the Primer Vector. This unequivocally confirmed that the calculated thrust orientation effectively maximizes the Hamiltonian over the entire proper time interval τ.

The use of OCULUS was, therefore, the key to the application of the entire project. It made it possible to translate a theoretical exercise in astrophysics and analytical mechanics into an operational and certified engineering tool capable of producing optimal interstellar flight solutions that will be presented and analyzed in detail in Chapter 4.

Chapter 4

Numerical Simulation and Results

The previous chapters have rigorously outlined the theoretical framework underlying this work, beginning with the geometric modeling of spacetime in General Relativity (See Chapter 2) and continuing with the derivation of the analytical conditions for optimization under strong gravity (See Chapter 3). This chapter represents the engineering and applied culmination of the research: the transition from the abstract mathematical model to a numerical laboratory. The objective of this section is to present, analyze, and interpret the results obtained from the integration of the 18-dimensional differential system within the simulation environment developed and interfaced with the unified OCULUS solver. Computational work in the potential well of Sagittarius A* poses significant numerical challenges: the extremely strong gravitational gradients, the strong nonlinearity of the relativistic equations of motion, and the divergences introduced by time dilation require careful calibration of the algorithm. To address this complexity methodically, the work has been divided into two phases:

1. **Dynamic Model Validation** (4.1): before introducing active control of the thrust, there is the need to demonstrate that the numerical integrator is capable of correctly simulating natural geodesic motion. To do so, pure free-fall trajectories have been analyzed to verify that the spacecraft's motion along the geodesics complies with the fundamental postulates of General Relativity.

2. **Interstellar transfer Optimization** (4.2): once the reliability of the physics engine has been verified, the actual Optimal Control Problem has been solved. An extreme mission scenario has been studied: continuous low-thrust space transfer between the highly eccentric orbits of stars S29 and S31 in the S-cluster. This section will show the convergence process of Indirect Methods and will analyze the effects that curved spacetime introduces.

The presented results prove how Optimal Control Theory, when properly managed through robust numerical algorithms, is capable of determining the path of minimum energy consumption even in the most hostile gravitational environment.

4.1 Dynamic Model Validation: Free-fall trajectories

Before introducing the complexities of Optimal Control Theory and subjecting the dynamic system to the variational solver for the search for optimal trajectories, a rigorous validation process of the numerical propagator is essential. The mathematical framework developed in Chapter 2, based on the equations of perturbed motion in the Schwarzschild metric, significantly increases the dimensionality and nonlinearity of the problem compared to classical astrodynamics. If the set of ordinary differential equations governing the evolution of states contained inaccuracies in the definition of the metric or the Christoffel symbols, the physical consistency of the optimal control formulation would be compromised. The gradients calculated for the evolution of the states would lose all physical meaning, inevitably leading the algorithm toward divergences or local optima. To avoid this possibility, the first computational step has been to integrate the dynamic system in the total absence of propulsive thrust (i.e. $F = 0$), with the goal of simulating a passive free-fall trajectory in space, verifying that the vehicle spontaneously follows the geodesics of curved spacetime generated by the mass of the supermassive black hole Sagittarius A*. This forward integration step was performed using the scientific library implemented in Python, thus outside the OCULUS environment. To manage the chaotic nature of the differential equations under strong gravity, the high-order explicit Runge–Kutta integrator DOP853 developed by Ernst Hairer was chosen, as this solver is particularly suited for high-precision integration of non-stiff problems. To ensure the absolute conservation of orbital energy and the four-velocity norm during the rapid fall into the potential well, the integration tolerances were tightened to limit values, imposing a relative error $r_{tol} = 10^{-11}$ and an absolute error $a_{tol} = 10^{-12}$.

4.1.1 Normalization and Reference Units

The numerical simulation of extreme astrophysical scenarios poses a computational challenge even before integration begins: the severe mathematical ill-conditioning caused by the use of International System (SI) units. Operating simultaneously with central masses on the order of 10^{36} kg, distances of 10^{10} meters, and velocities approaching the speed of light leads to the loss of the computer's floating-point precision and the rounding and truncation errors would quickly destroy the calculation of the system's Jacobian matrix. To protect the algorithm against these instabilities, the entire dynamic model was **normalized**. In standard interplanetary astrodynamics, normalization typically involves scaling distances by the radius of the starting orbit or the radius of the primary celestial body (e.g., the Earth's radius). However, in the context of General Relativity and for the specific case of free-fall, the very topology of spacetime suggests a natural reference metric: the Schwarzschild radius $R_s = \frac{2GM}{c^2}$. Assuming the estimated mass of SgrA* equal to $M_{Sgr} = 4.297 \times 10^6 M_\odot$, the Schwarzschild Radius, and consequently the basic Distance Unit (DU) of the framework, could be calculated:

$$DU \equiv R_s = 1.269 \times 10^{10}\text{m} \tag{4.1}$$

This parametric design choice yields an algebraic and numerical advantage: in the normalized space, the event horizon is confined to the exact dimensionless radial coordinate $Rs_{nd} = 1$. The critical term of the spacetime metric $(1 - \frac{R_s}{r})$, present in countless denominators within the Christoffel symbols, contracts into the elegant, simplified form $(1 - 1/r_{nd})$. From the definition of the unit distance, the remaining fundamental quantities follow logically through the laws of celestial mechanics. The Velocity Unit (VU), defined as the theoretical circular velocity at a distance of one DU, amounts to:

$$VU = \sqrt{\frac{\mu_{sag}}{DU}} = 2.1199 \times 10^8 m/s \tag{4.2}$$

It is interesting to note that the magnitude of the gravitational field in this region is such that it sets the reference velocity unit at approximately 70% of the speed of light in a vacuum ($c \approx 2.99 \times 10^8$ m/s). The kinematic variables processed by the solver are thus reduced to manageable dimensionless fractions. Finally, for proper time, the Time Unit (TU) derives from the ratio between DU and VU and is equal to

$$TU = \frac{DU}{VU} = 59.86s \tag{4.3}$$

Thanks to this normalization system, the spacecraft's 9-dimensional state vector, despite representing relativistic motion at significant fractions of c and in the vicinity of a supermassive black hole, is processed by the CPU using floating-point numbers whose order of magnitude is consistently close to unity. This ensures maximum numerical stability for the Runge-Kutta integrator, laying a solid foundation for the analysis.

4.1.2 Scenario Setup and Initial Conditions

The free-fall scenario structured to validate the numerical solver's response to the perturbed motion equations is fully explained in this section. The starting position was fixed at a radial distance $r_0 = 20\,R_s$, which corresponds to 20 Distance Units in the normalized system. Thanks to the perfect spherical symmetry of the Schwarzschild metric, which describes a non-rotating mass, the entire dynamics has been confined, without loss of analytic generality, to the equatorial plane. This results in the imposition of the initial colatitude $\theta_0 = \frac{\pi}{2}$ and the cancellation of its time derivative: $u_0^\theta = 0$. The phenomenological objective of this test is not the observation of a stable circular orbit, but to trigger an orbital decay geodesic and to induce this behaviour, the initial state vector has been perturbed by deliberately subtracting angular momentum from the system. Specifically, the azimuthal component of the four-velocity has been set to a suborbital value, equal to exactly 80% of the Keplerian tangential velocity required for equilibrium at the specific altitude:

$$u_0^\phi = 0.8 \cdot u_{circ}^\phi = 0.0063\,\mathrm{VU} \tag{4.4}$$

This deficit in centrifugal force was coupled with a weak initial radial velocity directed towards the center of attraction

$$u_0^r = -0.05\,\mathrm{VU} \tag{4.5}$$

The definition of the time component of the four-velocity, u^t, deserves a separate discussion, as it represents one of the pillars of relativistic mechanics. In a four-dimensional framework, u^t quantifies the initial dilation factor $dt/d\tau$ and does not represent an independent degree of freedom, but is rigidly constrained by the condition of invariance of the norm of the velocity four-vector for particles with mass: $g_{\mu\nu}u^\mu u^\nu = -c^2$. By expanding this tensor expression for the Schwarzschild diagonal metric and solving algebraically for the time component, the code must autonomously calculate the value of u_0^t so that the physical state is admissible. The equation implemented in the simulator is as follows:

$$u_0^t = \sqrt{\frac{1 + \left(1 - \frac{1}{r_0}\right)^{-1} (u_0^r)^2 + r_0^2 (u_0^\phi)^2}{1 - \frac{1}{r_0}}} \tag{4.6}$$

Entering the input kinematic data, the algorithm initialized this component to the exact value of:

$$u^t = 1.0355$$

The complete, normalized nine-dimensional state vector, passed as the initial condition to the DOP853 integrator, is therefore:

$$\mathbf{X}_0 = \begin{bmatrix} t \\ r \\ \theta \\ \phi \\ u^t \\ u^r \\ u^\theta \\ u^\phi \\ m \end{bmatrix} = \begin{bmatrix} 0 \\ 20 \\ \frac{\pi}{2} \\ 0 \\ 1.0355 \\ -0.05 \\ 0 \\ 0.0063 \\ 1 \end{bmatrix} \tag{4.7}$$

To ensure the stability of the integration, a boundary condition has been introduced. The mathematical singularity at the event horizon $r = 1\,DU$ causes the Christoffel symbols to diverge to infinity, due to the term $(1 - \frac{1}{r})$ in the denominator. To avoid reaching the NaN condition, the integration was controlled by an event function programmed to instantly halt the propagator as soon as the probe reached the safety threshold $r_f = 1.01\,DU$.

4.1.3 Kinematics of the Spiral and Transition to ISCO

The numerical evolution of the state vector has produced results that faithfully reflect the exact analytical solutions of General Relativity in the strong-field regime.

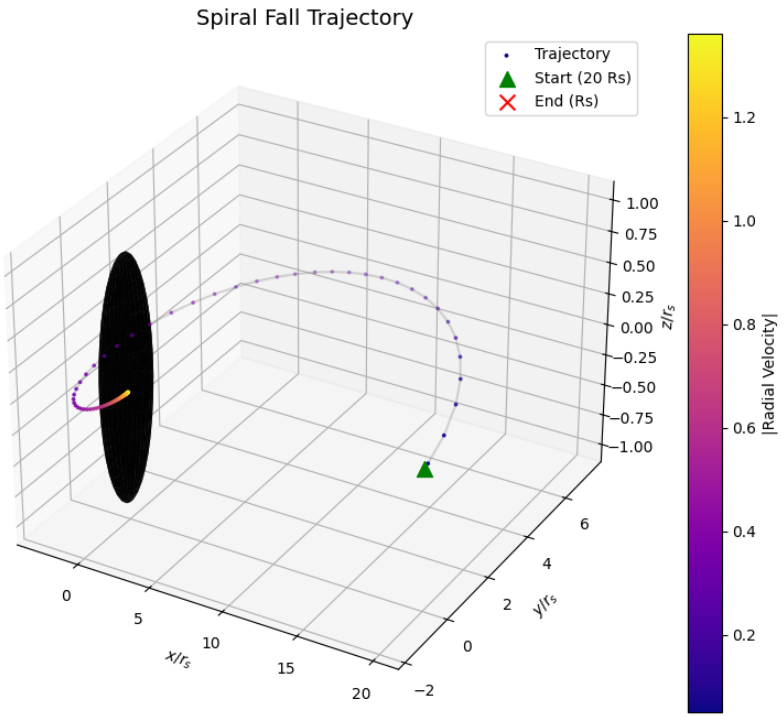

Figure 4.1: Spiral Fall Trajectory

The tree-dimensional spatial output (shown in the Spiral Fall Trajectory graph 4.1) visually illustrates the probe's spiral descent: due to the initial angular momentum deficit, the vehicle is unable to maintain its orbit and follows a spiral path converging toward the central mass. The color mapping associated with the trajectory highlights a drastic and non-linear increase in the magnitude of the radial velocity $|u^r|$ as the distance from Sgr A* decreases.

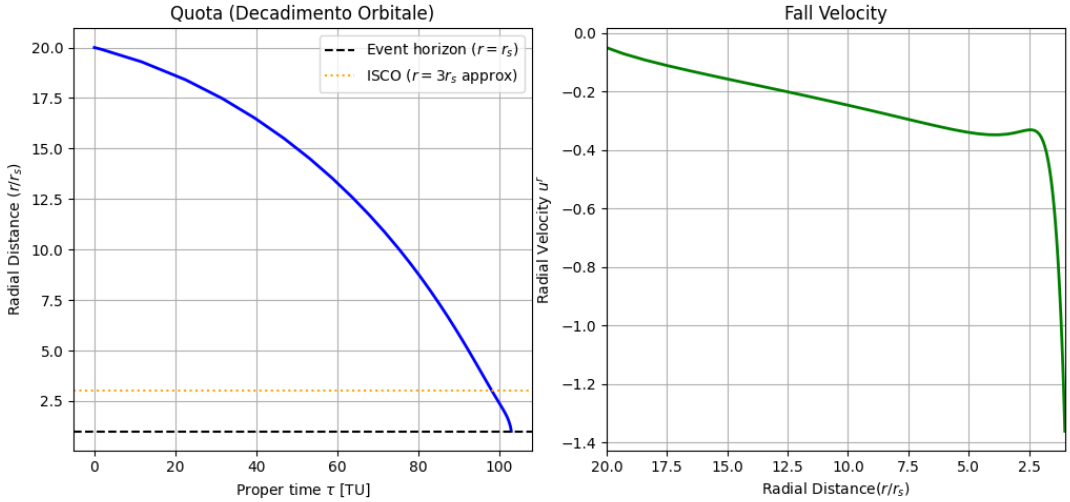

Figure 4.2: Free fall Trajectory results

A quantitative analysis of the temporal history of the decay, as shown in the "Quota" plot (radial distance r as a function of proper time τ), reveals that the trajectory spans the space separating the 20 Schwarzschild radii from the event horizon over a proper time interval calculated by the solver equal to $102.95\,TU$. Applying the previously derived dimensionless conversion factors, this duration is equivalent to 6163.31 seconds in the International System, or just under 1.71 hours. This specific numerical result elegantly resolves one of the most famous perspective effects of relativity: while a distant observer would see the object slow down asymptotically until it "freezes" on the horizon in an infinite coordinate time, the equations integrated confirm that, for the onboard clock in free fall, the journey has a strictly finite duration. The crossing of the critical threshold occurs within a determinable and, given the gravitational acceleration, extremely short proper time interval.

However, the depth and accuracy of the dynamic model are fully revealed by examining the kinematic profile in the "Fall Velocity" graph 4.2, which plots the evolution of the radial velocity u^r as altitude varies. In a simulation governed by Newtonian classical mechanics, the fall profile would describe a smooth, unbroken asymptotic curve, dictated by the potential proportional to $-\frac{1}{r}$. In the Schwarzschild model, the effective potential $V_{eff}(r)$ to which the particle is subject features an additional attractive term, proportional to $-\frac{1}{r^3}$, induced by the relativistic coupling with angular momentum. Examining the curve generated by the integrator, it can be observed that the spacecraft's radial velocity, initially equal to -0.05, decreases smoothly, becoming progressively more negative during the first segment of the transfer. As the free-fall progresses, at the exact moment when the radial coordinate intersects the value $|r| = 3\,DU$ (indicated analytically and graphically as critical boundary), the derivative of the curve undergoes a marked discontinuity, transforming into a nearly vertical inflection point. This boundary coincides mathematically with the ISCO. In the geometry of a non-rotating black hole, a distance of 3 Schwarzschild radii represents the ultimate limit of orbital stability: below this radius, the distortion of spacetime is so severe that the repulsive component of the centrifugal force ceases to be effective. No amount of angular momentum is sufficient to maintain a circular trajectory, and the centrifugal force itself paradoxically contributes to drawing the body towards the center. The Runge-Kutta integrator has captured this phenomenological collapse with precision: once the ISCO barrier is crossed, the spacecraft plunges into an inexorable fall, with the slope of u^r plummeting to values close to $-1.38\,VU$ just beyond the horizon.

4.1.4 Metric Divergence and Time Dilation

The final, and in some aspects most extreme, test for validating the dynamic model lies in the quantitative measurement of gravitational time dilation. In the mathematical framework developed for this thesis, the chronological decoupling between the vehicle's onboard clock and the time of an inertial observer located at the infinite distance is not an a posteriori calculation, but rather an active and constantly propagated state variable: the temporal component of the four-velocity $u^t = \frac{dt}{d\tau}$.

From an analytical point of view, the evolution of u^t is dominated by the coefficient g_{tt}

of the Schwarzschild covariant metric tensor, which contains the spatial term $(1 - \frac{R_s}{r})$ in its denominator. This geometric architecture dictates that, in asymptotically flat regions of space ($r \to \infty$), the ratio $\frac{dt}{d\tau}$ tends to unity and time flows as one can measure it on planet Earth. Conversely, as the radial coordinate approaches the event horizon ($r \to R_s$), the denominator tends to zero, forcing the variable u^t towards a divergent vertical asymptote. The numerical goal is to verify that the Runge-Kutta integrator can track this non-linearity without incurring instability or violations of the four-dimensional norm.

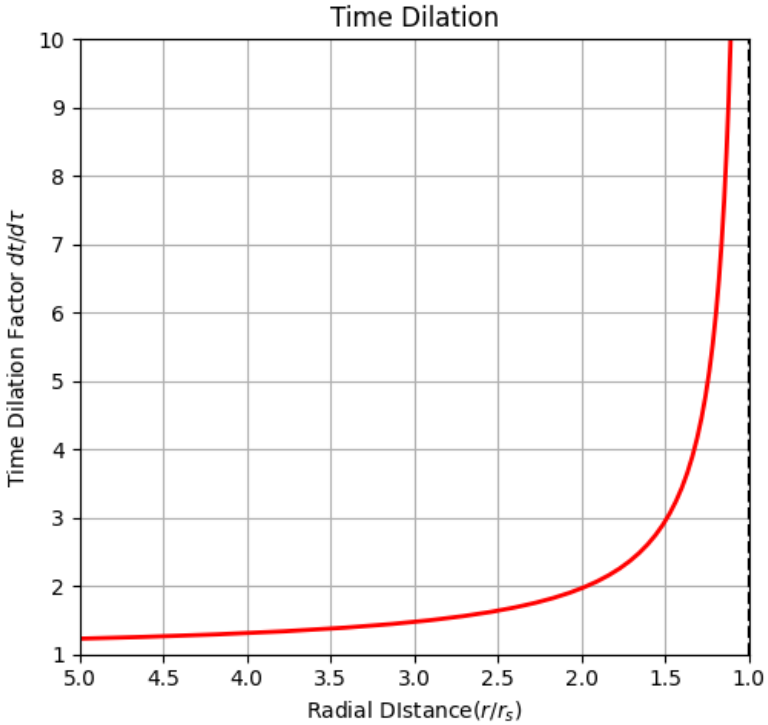

Figure 4.3: Time Dilation in Free-fall

Looking at the graph labeled 'Time Dilation' 4.3, the solver's behavior proves to be flawless. At the moment the vehicle is released, at an initial radial altitude of $20R_s$, the gravitational field of Sagittarius A* already exerts a perceptible distortion on the fabric of spacetime: the value recorded for the variable u^t is 1.0355. Although the proximity to a supermassive black hole is evident, in this initial phase proper time flows at a rate still comparable to that on Earth, slowed by a modest 3.5%. However, as the curve shifts to the left, that is as the spacecraft spirals inexorably downward, the time distortion ceases to be a negligible disturbance and becomes the dominant macroscopic effect. The curve plotted by the simulator rises sharply along an exponential gradient. The moment the code reaches the preset stop condition at the cutoff coordinate $r_f f = 1.01R_s$, the calculated dilation factor skyrockets to a value of **99.36**. The physical interpretation of this single numerical value describes an extreme scenario: in the spacetime layer adjacent to the event horizon, for every single second ticked by the onboard clock or processed by the spacecraft's navigation computer, 99.36 seconds elapse in the rest if the universe, and specifically in distant reference frames such as our Solar System.

Variable	Value
r_0	$20R_s$
r_f	$1.01R_s$
Flight Proper Time τ	$6136.31s = 1.71hrs$
Time Dilation at r_0	$u_0^t = 1.0035$
Time Dilation at r_f	$u_f^t = 99.36$

Table 4.1: Free-fall simulation data

As shown by the simulation data and outputs in Table 4.1, the practical implications for a hypothetical mission are staggering: if the vehicle were to orbit or remain in free fall within that specific portion of space for a local duration of just 4 days (measured in proper time τ), the Coordinate Universal Time on Earth would advance by more than 397 days. This translates to the loss of more than a year of external history for a handful of days spent near the singularity. The fact that the DOP853 solver managed to map a gradient of such magnitude while maintaining the stringent convergence tolerances intact demonstrates that the normalized formulation of the problem was a crucial modeling insight for computational success. These results collectively confirm that the numerical framework is capable of reproducing both the qualitative and quantitative features of relativistic motion in strong gravitational fields, validating its suitability for optimal control applications in curved spacetime.

4.2 Interstellar Transfer Optimization: the S29-S31 Mission

Following the successful validation of the dynamic model, the study proceeded to the core of the research: applying the Optimal Control Theory to plan a propelled interstellar transfer. The mathematical model developed, based on the variational application of Pontryagin's Principle, finds its expression in an extreme astrophysical environment in the Galactic Center: the S-cluster. This swarm of young massive stars, orbiting close to the event horizon of Sagittarius A*, constitutes a "relativistic laboratory" for testing advanced spaceflight architectures. Before proceeding with the mathematical formulation of the Boundary Value Problem and the presentation of the numerical results, it is essential to justify the selection of the specific mission scenario addressed. Among the dozens of celestial bodies cataloged in the cluster, the optimal control study focused on the design of a propelled rendezvous between star S29 and star S31. This choice is not arbitrary but is dictated by a rigorous engineering and computational investigation strategy based on four fundamental criteria:

1. **Orbital Plane Alignment** (Minimization of Normal ΔV):

   In interplanetary astrodynamics, orbital plane-changing maneuvers are notoriously the most propellant-intensive, requiring thrust to be applied in a direction perpendicular to the inertial velocity vector. In strong gravitational fields, the inertia associated with such maneuvers quickly becomes prohibitive. The stars S29 and S31 share very similar orbital planes, with inclinations of $i_{S29} = 105.8°$ and $i_{S31} = 109.03°$,

respectively. The small spatial misalignment ($\Delta i \approx 3.2°$) ensures that the solver does not need to saturate the thrust due to excessive out-of-plane corrections, allowing the variational algorithm to focus the Primer Vector on optimizing radial energy and temporal phasing.

2. **Energetic Affinity and Radial Distance**:

   The two targets occupy a neighboring spatial "shell" within the gravitational well. S29 has a semi-major axis $a = 3500\,\text{AU}$, while S31 has $a = 3670\,\text{AU}$. Since the orbital energy levels are comparable, the transfer does not require the spacecraft to perform unrealistic gravitational jumps as would be the case, for example, when departing from the innermost orbits to reach a star at the outer edge of the cluster. This keeps the flight time and mass consumption within physically feasible limits for the hypothetical nuclear propulsion technology.

3. **Exploitation of the Relativistic Oberth Effect**:

   Both stars exhibit high eccentricities: $e_{S29} = 0.728$ and $e_{S31} = 0.5497$. This marked ellipticity results in velocities reaching a few percent of the speed of light when at the pericenter. This kinematic configuration provides the perfect test bed for evaluating the indirect solver's ability to identify and exploit the Oberth Effect: applying thrust at the moment of maximum velocity to maximize the maneuver's energy efficiency.

4. **Numerical Treatability and Proof of Concept**:

   The numerical solution of an 18-dimensional TPBVP in Schwarzschild topology is inherently prone to catastrophic divergences, due to the severe stiffness of the perturbed geodesics. Selecting two spatially close and kinematically similar orbits represents the ideal Proof of Concept: it provides the OCULUS algorithm and the continuation method with a sufficiently well-posed problem to isolate and validate the family of optimal solutions.

Having defined and justified the mission's operational environment, it is possible to translate these astronomical premises into a confined and normalized mathematical framework, an essential prerequisite for the solver's convergence.

4.2.1 Scenario, Boundary Conditions and Numerical Normalization

Formulating a Boundary Value Problem requires a rigorous translation of the physical scenario into a bounded mathematical domain. As mentioned, the transfer addressed in this study involves the departure of a spacecraft from S29's orbit, and consequent realization of an orbital rendezvous with the target being star S31. As evidenced by the classical Keplerian parameters summarized in Table 4.2, the two celestial bodies share a neighboring gravitational environment, but follow highly eccentric and kinematically misaligned trajectories in three-dimensional space.

To visually appreciate the spatial relationships that justify this mission architecture, Figure 4.4 illustrates the three-dimensional rendering of the two unperturbed orbits around Sagittarius A*. The plot highlights the proximity of the orbital planes and the shared

Keplerian Parameter	**Starting Star (S29)**	**Destination Star (S31)**
Semi-major axis (a)	3500 AU	3670 AU
Eccentricity (e)	0.728	0.5497
Inclination (i)	105.8°	109.03°
Ascending node (Ω)	161.96°	137.16°
Argument of Pericenter (ω)	346.5°	308°

Table 4.2: Classical orbital parameters of the stars relative to the focus in Sagittarius A*

depth within the gravitational well, which are crucial factors for maintaining the ΔV within physically feasible limits.

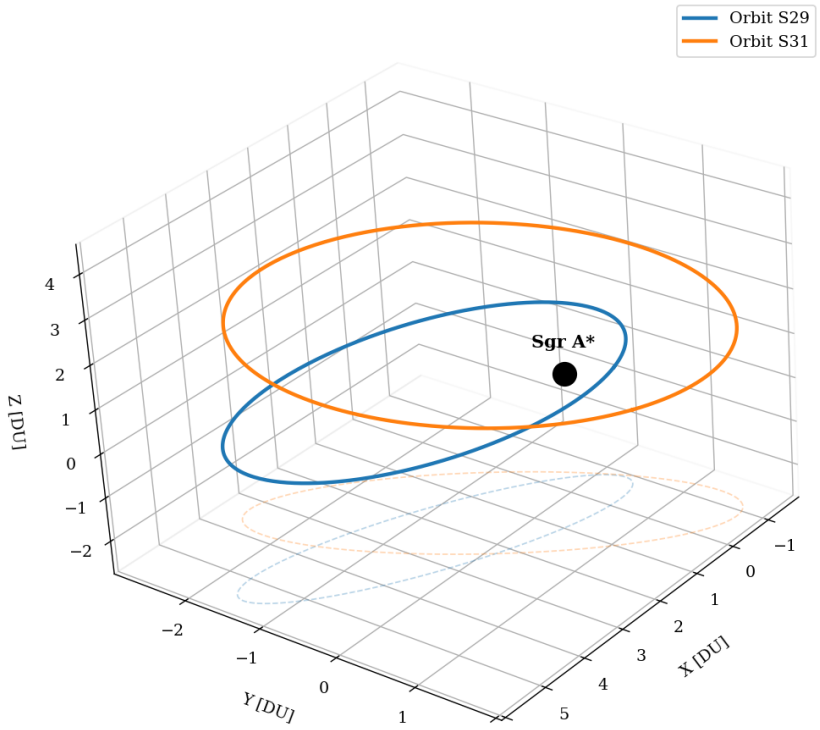

Figure 4.4: 3D spatial configuration of the departure orbit (S29) and the target orbit (S31)

The search for the global optimal trajectory was not conducted by arbitrarily fixing the starting and ending points on the respective orbits in advance. The search for the global optimal trajectory was not conducted by arbitrarily fixing the starting and ending points on the respective orbits in advance. Instead, the developed framework involved the implementation of a rigorous grid-search based on the parameterization of the true anomalies, f_0 for star S29 and f_{tgt} for star S31. The objective of this parameterization is to map an entire space of possible configurations in order to identify the specific launch window capable of absolutely minimizing propellant consumption. The details of this extensive iterative simulation campaign in the OCULUS environment, the subsequent topological analysis of the solution families, and the identification of the mission's global optimum will be discussed in depth in Sections 4.2.4, 4.2.5 and 4.2.6

Normalization Procedure

As for the free-fall case, it is of fundamental importance to proceed with the normalization of the problem to avoid having an ill-conditioned system, as using the standard measure units of the SI could lead to failure in the convergence of the solver. The chosen scenario has heterogeneous and huge physical parameters: the gravitational constant is on the order of 10^{-11}, the mass of the black hole is approximately 10^{36} kg, the orbital distances of the S-type stars span scales of hundreds of billions of meters (10^{14} m), while the control variables, such as mass consumption or the dilation factor u^t, hover around unity. Including quantities separated by many orders of magnitude within the same set of differential equations triggers two main issues:

- Machine Precision Saturation: When calculating the Jacobian matrix of the 18-dimensional system, subtraction between very large numbers or division by infinitesimally small numbers triggers fatal round-off errors.
- Sensitivity of the Constraints: The adjoint variables λ rule the optimality of the system by dictating the orientation of the Primer Vector. If the physical state variables are unbalanced, the associated cost terms undergo disproportionate fluctuations, making the problem "stiff" and causing the optimization algorithm to diverge from the first iterations.

To overcome this mathematical obstacle, the entire dynamic model has been mapped to a confined dimensionless domain. A base Distance Unit has been established, proportional to the S-cluster environment, in particular it was set equal to the major semi-axis of the S2 star, which represents the best-characterized orbit in the S-cluster thanks to long-term observations. Then, from this quantity, the Velocity Unit and the Time Unit were analytically derived. The values obtained are the following:

$$DU \equiv a_{s2} = 1025\,\text{AU} \tag{4.8a}$$

$$VU = \sqrt{\frac{\mu_{sag}}{DU}} = 1.928 \times 10^{6}\,\text{m/s} \tag{4.8b}$$

$$TU = \frac{DU}{VU} = 7.95 \times 10^{7}\,\text{s} \tag{4.8c}$$

The vehicle's mass was also normalized, setting $m_0 = 1.0\,[\text{adim}]$ at the start. This normalization ensures that the state and adjoint variables evolve within comparable numerical magnitudes, improving the conditioning of the indirect optimization problem. Consequently, errors in convergence tolerances, set to 10^{-9}, take on a proportional and uniform magnitude across all equations. An error of 10^{-9} on a dimensionless distance implies uniform kilometer-scale precision, preventing gradients from exploding. Additionally, the OCULUS solver is capable of recalibrating initial guesses with regular increments, exploring the intricate solution space with stability and speed.

After completing this process, the actual optimization began.

4.2.2 State Vector: from Keplerian Elements to Relativistic Vectors

The correct formulation of a boundary-value problem requires the exact and consistent definition of the spacecraft's state at the initial time τ_0 and of the target's state at the final time τ_f. The differential solver based on the Schwarzschild metric developed for this thesis cannot operate directly with classical orbital elements, and it was therefore necessary to develop a computational pre-processing architecture capable of translating these observational data into the vector format required by the relativistic model. This chain of geometric and kinematic transformations consists of four sequential steps:

1. Conversion to Physical Cartesian Coordinates: Given the orbital parameters of the initial and target star (See section 4.2.1) and a parametric value for the true anomaly (f) as input, the algorithm first calculates the position vector $\mathbf{r}_{phys}$ and velocity vector $\mathbf{v}_{phys}$ in the three-dimensional inertial Cartesian reference frame centered on the black hole's singularity. In this first phase, the quantities are strictly expressed in International System (SI) units, using the standard gravitational mass μ_{sag} and converting Astronomical Units (AU) to meters.

2. Normalized System: As discussed in Section 4.2.1, to avoid severe under-conditioning, the Cartesian physical vectors are normalized. The three spatial components are divided by the Distance Unit, while the three velocity components are normalized with respect to the Velocity Unit.

3. Relativistic Mapping into Spherical Coordinates: The normalized Cartesian vectors are projected into the spherical coordinate system specific to the adopted spacetime topology. The algorithm computes the radial coordinate r, the colatitude θ, taking care to correctly map the inclination of the orbital plane in the polar angle formalism measured from the Z-axis, and the azimuthal angle ϕ. Simultaneously, the Cartesian velocities are transformed into the spatial components of the vehicle's four-velocity.

4. Constraint on the Four-Velocity and State Closure: The final and most delicate step involves initializing the scalar variables of the 9-dimensional state vector: coordinate time, the mass (m) and the time dilation factor (u^t). Coordinate time was normalized using the TU defined, while the mass at the start is set to unity, representing the vehicle fully loaded with propellant. The time component $u^t = dt/d\tau$, on the other hand, cannot be derived from classical kinematics but must exactly satisfy the normalization constraint of the four-vector in General Relativity:

$$g_{\mu\nu} u^\mu u^\nu = -c^2$$

   By algebraically solving this tensor equation for the term u^t, the algorithm determines the complete state vector, ensuring that the initial and final conditions provided to the solver belong to physically admissible trajectories

Since the search for the global optimum of the mission involves the parametric exploration of countless departure and arrival points, the architecture described was used to dynamically generate the boundary conditions for each exploratory iteration.

After the extensive simulation and optimization campaign, discussed in-depth in the following sections, the global optimum for minimum propellant consumption was identified for a launch from S29 at a true anomaly of $f_0 = -5°$ and a rendezvous at S31 at an anomaly of $f_{tgt} = 135°$.

Dynamic Variable		**S29** ($\tau = 0$)	**S31** ($\tau = \tau_f$)
Coordinate Time	t	0.000000	Free
Radial Coordinate	r	0.930271	4.087285
Colatitude	θ	1.881066	0.353110
Azimuth Angle	ϕ	2.917588	1.183240
Time Dilation	u^t	1.000082	Free (derived from motion)
Radial Velocity	u^r	-0.050088	0.245907
Colatitude Velocity	u^θ	-1.402888	-0.031522
Azimuthal Velocity	u^ϕ	-0.439600	-0.257981
Vehicle Mass	m	1.000000	To be maximized

Table 4.3: Normalized state vectors for the optimal mission configuration

By way of example and for completeness, Table 4.3 shows the exact configuration of the dimensionless state vectors calculated for this specific optimal configuration, which constituted the rigid boundaries of the Boundary Value Problem.

4.2.3 The BVP Challenge: Numerical Solution via Homotopy in OCULUS

The application of Pontryagin's Maximum Principle to a dynamic system governed by the Schwarzschild metric transforms the trajectory optimization problem into a challenging Two-Point Boundary Value Problem. The mathematical framework requires the simultaneous integration of 18 highly nonlinear ordinary differential equations: 9 equations for the evolution of the spacetime physical states $\mathbf{X}$ and 9 additional equations for the evolution of the constraints $\boldsymbol{\lambda}$. The problem of extreme sensitivity to the initial guess lies in the intrinsically mixed nature of the boundary conditions: at the starting time τ_0, the spatial and kinematic state vector $\mathbf{X}_0$ is perfectly known and fixed by the position of star S29, while, in contrast, the nine initial values of the adjoint variables, grouped in the vector $\boldsymbol{\lambda}_0$, are entirely unknown quantities. These parameters do not possess a direct physical interpretation but represent the sensitivity of the Hamiltonian to state variations, dictating the temporal evolution of the Primer Vector and, consequently, the instantaneous orientation and firing logic of the space thruster. Due to the chaotic geometric topology introduced by the metric tensor of a supermassive black hole, the domain of attraction for iterative methods is microscopically small. Providing the solver with a random or zero vector $\boldsymbol{\lambda}_0$ would result in the instantaneous divergence of the trajectory: an error of even just the fourth decimal place in one of the velocity components would deflect the Primer

Vector to such an extent as to plunge the vehicle beyond the event horizon or scatter it into unbound escape trajectories, inevitably missing the rendezvous with the target.

The Homotopy Strategy: Progressive Construction of the Solution

Blindly identifying the set of parameters capable of simultaneously satisfying all final constraints and driving the solver to convergence constitutes a numerically huge challenge. To overcome this mathematical rigidity, the operational strategy adopted is based on the homotopy (or continuation) method. This numerical approach involves initially formulating a simplified problem, and then gradually reintroducing the complexity of the astrodynamics constraints. The key to the method lies in using the convergent adjoint variables obtained at continuation step k as the initial hypothesis (i.e. the new guess for the vector $\boldsymbol{\lambda}_0$ for continuation step $k+1$. Operationally, OCULUS' unified and visual environment allowed to orchestrate the homotopy through a precise sequence of tightening the Boundary Conditions:

1. **Phase 1**: Radial Intersection, One-Dimensional Convergence: In the first attempt, the TPBVP was stripped of almost all its structural complexity. The solver was instructed to ignore colatitude, azimuth angle, and the entire kinematic configuration velocities. The only mathematical constraint imposed at the end of the integration was reaching the same radial altitude as the target star S31, imposing the residual equation $r(\tau_f) - r_{S31} = 0$. Thanks to the high number of degrees of freedom left unbound, the nonlinear optimization algorithm was able to explore a sufficiently large attractor set, converging in just a few cycles toward a first, rough set of initial conditions.

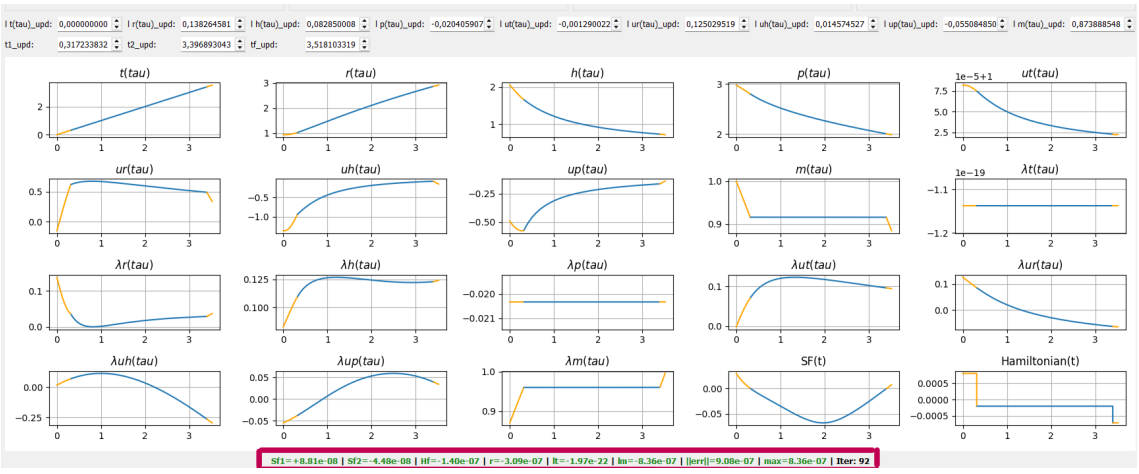

Figure 4.5: One-dimensional Convergence

2. **Phase 2**: Complete Spatial Rendezvous, Three-Dimensional Position Match: Once the first family of solutions $\boldsymbol{\lambda}_0$ was isolated, these vectors were saved and reused as initial conditions for the second level of homotopy. In this phase, the residuals on the angular coordinates were reactivated. By providing an initial guess that already ensured the correct gravitational separation from the black hole having previously

fixed the radius, OCULUS required only minimal iterative corrections to lock onto the exact point in curved space, though still reaching the target with entirely arbitrary orbital energy and velocity vectors.

3. **Phase 3**: Kinematic Rendezvous, Four-Velocity Match: The third step represents the computationally most delicate phase for the mission's physics. Using the results from Phase 2, the problem was severely constrained by requiring the elimination of residuals on the three spatial components of the four-velocity (u^r, u^θ, u^ϕ). This phase forces the solver to radically restructure the temporal framework of the integration: the algorithm must calibrate the logic for engine ignition and shutdown, or Bang and Coast phases, not only to arrive at the exact point, but to reach it while tracking the target with the velocity vector aligned.

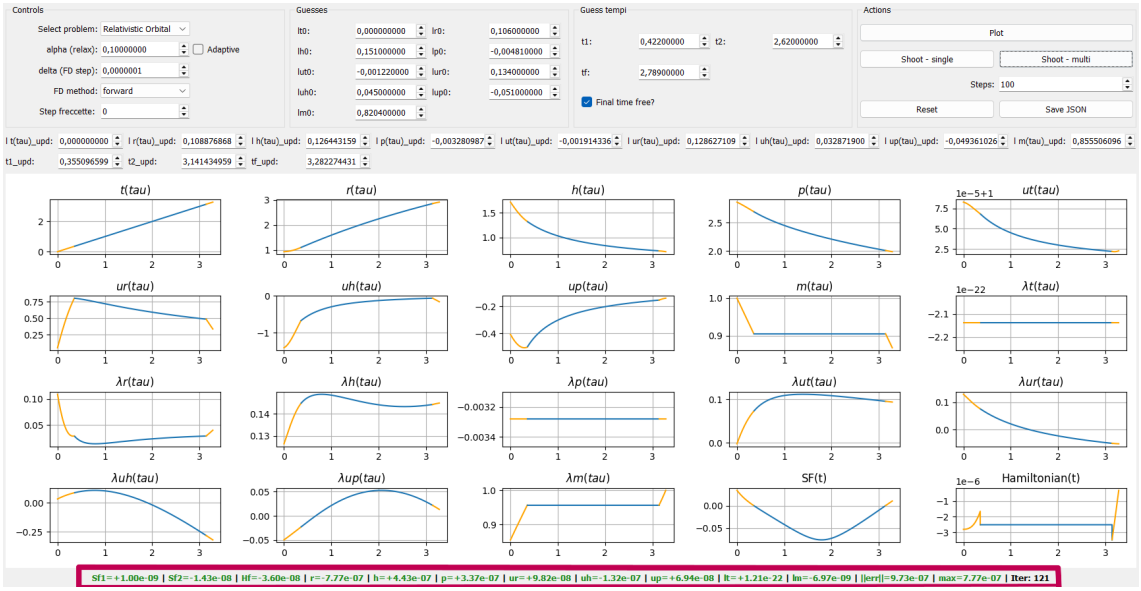

Figure 4.6: Complete Optimized Solution

Optimal Control Structure: Switching Function and Hamiltonian Analysis

Imposing the condition of transversality on the mass formally resolves the Optimal Control Problem, allowing the algorithm to actively shape the thrust profile. The firing and shutdown of the thruster are mathematically governed by the sign of the Switching Function $\mathcal{S}_\mathcal{F}$. This function balances the kinematic benefit of turning on the engine against the cost in terms of mass consumption.

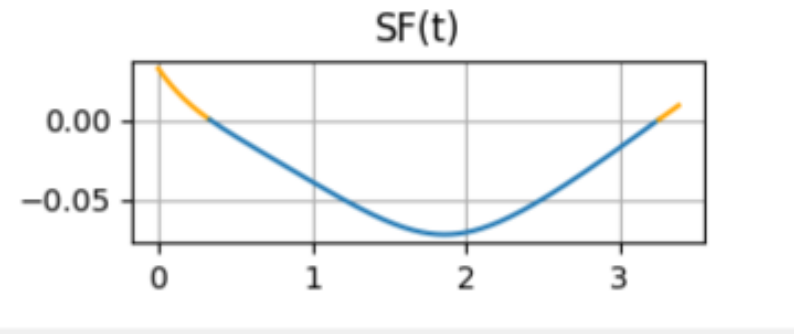

Figure 4.7: Switching Function

Analysis of the time evolution of $\mathcal{S}_\mathcal{F}$ for the family of convergent solutions obtained, well illustrated in Figure 4.7, reveals that the solver has spontaneously and rigorously identified an optimal Bang-Coast-Bang control structure. The trend of the curve takes on a characteristic U-shaped form, parabolic and concave upward, defining three distinct flight phases:

1. **Initial Bang** $\mathcal{S}_\mathcal{F} > 0$: At the moment of departure, the switching function is strictly positive. The vehicle fires its thrusters at maximum thrust to generate the ΔV required to break free from the original orbit of star S29, overcome the local gravitational gradient, and enter the transfer geodesic.

2. **Coasting Arc** $\mathcal{S}_\mathcal{F} < 0$: Upon reaching the cutoff time τ_1, the curve crosses zero and takes on negative values. The solver enforces the complete shutdown of the thruster, thus $F = 0$. In this extended central interval, the spacecraft passively traverses the curved spacetime, conserving propellant and allowing the Schwarzschild metric to naturally curve the trajectory towards the target.

3. **Final Bang** $\mathcal{S}_\mathcal{F} > 0$: Near arrival, at time τ_2, the switching function becomes positive again. The thruster is reactivated for braking or final kinematic adjustment, canceling the residual relative velocity to achieve a perfect rendezvous with star S31 at time τ_f.

The final and definitive validation of the quality of the optimization is confirmed by analyzing the system's Hamiltonian $\mathcal{H}$. Since this is a final time free problem, and the mission duration τ_f is itself a variable optimized by the solver to minimize propellant consumption, Optimal Control Theory dictates that the Hamiltonian must remain identically zero along the trajectory

$$\mathcal{H}(\tau) = 0$$

As can be seen in Figure 4.8 the value of the Hamiltonian calculated instant by instant remains flat and confined within a numerical tolerance band of 10^{-13}.

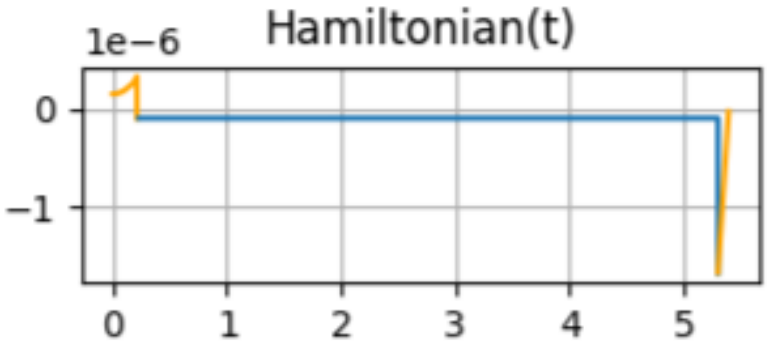

Figure 4.8: Hamiltonian

This exceptional stability, approaching the limit of double-precision machine accuracy, mathematically certifies that the Bang-Coast-Bang sequence found is, to all intents and purposes, a valid solution to the Boundary Value Problem in the relativistic regime.

4.2.4 Orbital Parametrization and Solution Mapping

The homotopy approach described serves as the mathematical tool for ensuring the convergence of the variational solver. However, once a set of initial conditions $\boldsymbol{\lambda}_0$ capable of satisfying all rendezvous constraints and minimizing propellant consumption has been obtained, the solution is optimal only in a local sense, so it represents the best possible control law exclusively for those two specific geometric points of initial state and arrival point fixed in space. In the context of celestial mechanics and relativistic astrodynamics, celestial bodies are not static targets. The stars S29 and S31 follow highly eccentric orbits, moving at speeds that reach significant fractions of the speed of light as they pass through their pericenters. Consequently, the energy cost of the transfer, and thus the engineering feasibility of the mission, is critically dominated by the orbital phasing. A transfer trajectory that is computationally optimal for a given launch date could prove energetically prohibitive, or even physically unfeasible, if delayed by even a few days, due to the changed mutual arrangement and gravitational gradients of the black hole. To go beyond the local optimum and aim instead for the global optimum of the mission, a single convergent TPBVP is not sufficient. It was therefore necessary to implement a large-scale structured parameterization campaign, transforming the problem from a single instance into a family of problems parameterized with respect to the initial and arrival orbital positions. The domain of investigation was defined by isolating two fundamental degrees of freedom: the true anomaly f_0 of star S29 at the start of the mission and the true anomaly f_{tgt} of star S31 at the end of the mission. The combined exploration of these two parameters defines a two-dimensional grid, that depicts the space of possible mission configurations. If one were to attempt to provide the solver with random orbital configurations within this grid, the solver would again encounter numerical collapse due to the lack of an adequate initial guess for the constraints. The solution to this impasse consisted of applying the homotopy logic no longer to the activation of the constraints, but directly to the displacement of the boundary conditions in space. The algorithmic logic

applied is as follows:

1. First, a known convergent configuration is set, defined by (f_0, f_{tgt}) and its validated set of convergent guesses $\boldsymbol{\lambda}_0$.

2. A small spatial perturbation is applied, increasing or decreasing the starting or target angle by a discrete step Δf. The new set of data for four-position and four-velocity is calculated.

3. The vector $\boldsymbol{\lambda}_0$ from the previous step represents an exceptionally accurate initial guess for the new problem.

4. With this initial guess, OCULUS rapidly converges to the new orbital configuration in a few iterations.

This chain-continuation process made it possible to smoothly track the stars as they moved around Sagittarius A*. By repeating the angular sweep for different starting and ending positions, the framework automatically populated a vast database of convergent solutions. The process ended when the solver converged to a solution belonging to a new family of results, in which the switching function changed its shape, going for example from a Bang-Coast-Bang solution to a Bang-Coast-Bang-Coast-Bang one.

The result of this computational architecture is not a single trajectory, but rather a full-fledged multidimensional data matrix. For each explored pair of (f_0, f_{tgt}), the algorithm stored the corresponding vector of converged initial adjoint variables, the optimal engine on/off times (τ_1, τ_2), and the total flight time (τ_f).

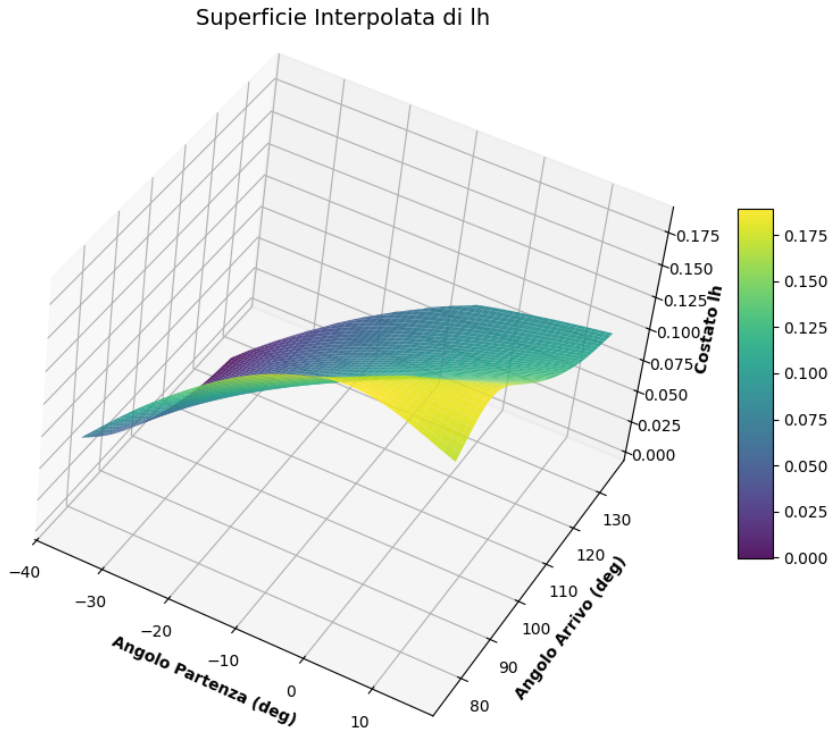

Figure 4.9: 3D graphs examples

Upon examining the surfaces generated for the entire set of multipliers (as in the example shown in Figure 4.9), the first and most significant engineering observation is the absolute morphological smoothness. In nonlinear optimization problems, the strong nonlinear sensitivity of the differential equations often causes solvers to jump chaotically between uncorrelated local minima, generating parametric graphs rich in discontinuities, peaks, or numerical noise. In contrast, the surfaces extracted by OCULUS appear as smooth, fluid manifolds devoid of local asymptotes or singularities. This smoothness is not only a qualitative feature, but also a numerical validation of the continuation strategy. The absence of discontinuities indicates that the solver consistently converged to neighboring solutions without jumping between unrelated local minima, confirming the robustness and stability of the indirect optimization process across the parameter space. The algorithm did not simply guess a series of independent solutions but successfully traced a single coherent family of active geodesics, where each rendezvous configuration evolves continuously and differentiably into the adjacent one. The regularity of these three-dimensional surfaces constitutes a double validation of the work performed:

1. From a mathematical standpoint, it certifies that the solver did not jump arbitrarily between distant and uncorrelated local minima, but successfully traced a coherent family of Optimal Control solutions.

2. From a physical standpoint, it demonstrates the high sensitivity of the thrusting

strategy to the curvature of spacetime: as the exact position within the gravitational potential changes, the adjoint variables adapt non-linearly to navigate the complex map of Christoffel symbols.

The systematic mapping of this solution space has paved the way for the final phase of the research. With the entire spectrum of valid constraints available for countless rendezvous configurations, the final procedural step consists of dynamically propagating each of these initial conditions. Finally, extracting the mass consumption for each grid node will make it possible to identify the single orbital architecture that guarantees the minimum overall propulsive expenditure for the interstellar mission.

4.2.5 Analysis of the Adjoint Variables Mapping

The intensive simulation campaign, guided by the continuation and cross-parameterization approach, yielded a dataset of optimal trajectories corresponding to combinations of launch and arrival windows between the stars S29 and S31. Even before focusing on the extraction of the global optimum, that is the trajectory with minimum absolute propellant consumption, an analysis of the solution space identified by the OCULUS algorithm can be done. From this perspective, the three-dimensional visualization of the initial guesses of the adjoint variables as a function of the initial and final anomalies becomes a tool of "relativistic diagnostics". Although the variational adjoint functions are conjugate mathematical quantities lacking immediate direct physical measurability, they represent the sensitivities of the system's Hamiltonian with respect to perturbations of the states. Mapping their evolution means capturing the way in which Pontryagin's Principle bends the control logic to adapt to the severe topology of the gravitational well of Sagittarius A*. Some of the graphs obtained are shown, explained and discussed in detail below.

The Effect of the Gravitational Well: The Radial Variable λ_r

The multiplier associated with the radial coordinate constitutes the measure of the work required to escape the gravitational well of Sagittarius A*. To understand the morphology of this three-dimensional surface, one must look directly at the heart of the Euler-Lagrange equations governing the indirect optimization. The time derivative of the radial adjoint variable is given by the equation:

$$\dot{\lambda}_r = -\frac{\partial \mathcal{H}}{\partial r} \tag{4.9}$$

Unlike the angular coordinates, the partial derivative of the Hamiltonian with respect to r is a term of large proportions and extreme non-linearity. The Hamiltonian (See Appendix C), in fact, contains within it the components of the covariant and contravariant metric tensor (e.g., $g_{tt} = -(1 - R_s/r)$ and $g_{rr} = (1 - R_s/r)^{-1}$) and the entire set of Christoffel symbols $\Gamma^{\alpha}_{\beta\gamma}$. Since the star S29 has a very high eccentricity, varying the initial proper anomaly f_0 means varying the initial distance r_0 from the black hole.

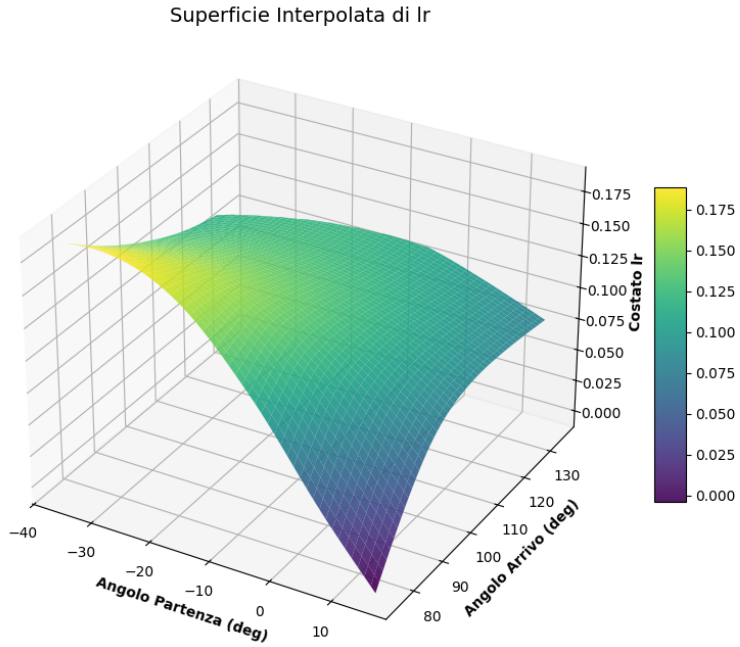

Figure 4.10: $\lambda_{r,0}$ vs (f_0, f_{tgt})

The topological and physical analysis of the surface $\lambda_{r,0}$ reveals the following astrodynamics features:

- The Spacetime Curvature Gradient: the most striking visual feature of Figure 4.10 is the presence of an extremely steep and sharp diagonal gradient. The values rapidly decrease from the light-yellow areas, where the curvature reaches its positive maximum, to the deep purple valleys. This steep decline reflects how spacetime curvature influences the optimal solution: shifting the launch window by even a few degrees means forcing the spacecraft to depart from a radial altitude where the slope of the gravitational potential $(1 - \frac{R_s}{r})$ is radically different. The λ_r term severely penalizes these variations, forcing the algorithm to aggressively correct the Primer Vector to prevent the trajectory from collapsing.

- The "Penalty" of Gravitational Climbing: the highest and most positive values of $\lambda_{r,0}$ occur for misaligned geometric configurations, for example for launches significantly ahead of the pericenter coupled with arrivals that are also early. In these suboptimal scenarios, the vehicle lacks the kinetic energy needed to exploit the Oberth effect. The algorithm is "aware" that to reach the distant orbit of S31 starting from a disadvantaged position, it will have to expend enormous amounts of energy solely to climb out of the steepest portion of the gravitational potential well. The radial cost rises to signal to the Hamiltonian the extreme sensitivity and prohibitive cost of this change in altitude.

- Relaxation at the Pericenter: in contrast, when the analysis shifts toward the area of optimal solutions, the surface of the radial gradient tends to stabilize at less extreme gradients. Starting near the pericenter, the spacecraft has very high orbital velocity and is already moving along the natural geodesic that will "slingshot" it toward the outer reaches of the S-cluster. In this configuration, the radial increase is largely guaranteed by celestial mechanics and inertia: the solver no longer has to fight against the black hole to gain altitude, and consequently the sensitivity of the Hamiltonian to the coordinate r relaxes.

Figure 4.10 is thereby not only a spatial map, but it is the mathematical representation of the Schwarzschild gravitational field and suggests that the control algorithm does not simply draw straight lines between two points, but senses the weight, distortion, and depth of the potential well through which it is navigating.

The Relativistic Steering Wheel: λ_{u^r}, λ_{u^θ}, and λ_{u^ϕ}

While spatial parameters $(\lambda_r, \lambda_\theta, \lambda_\phi)$ measure the geometric deformation of the mission, the parameters associated with the four-velocity components play an operational role. In Optimal Control Theory, these three multipliers define the vector components of the Primer Vector. Therefore, the adjoint variables are not merely abstract sensitivities, but directly determine the thrust direction through the Primer Vector. At each instant, the control law aligns the thrust vector with the direction that maximizes the Hamiltonian, making the adjoint variable the fundamental link between the system dynamics and the propulsion strategy. The joint analysis of the surfaces of the three kinematic sides reveals the complex propulsive plan for the Initial Bang:

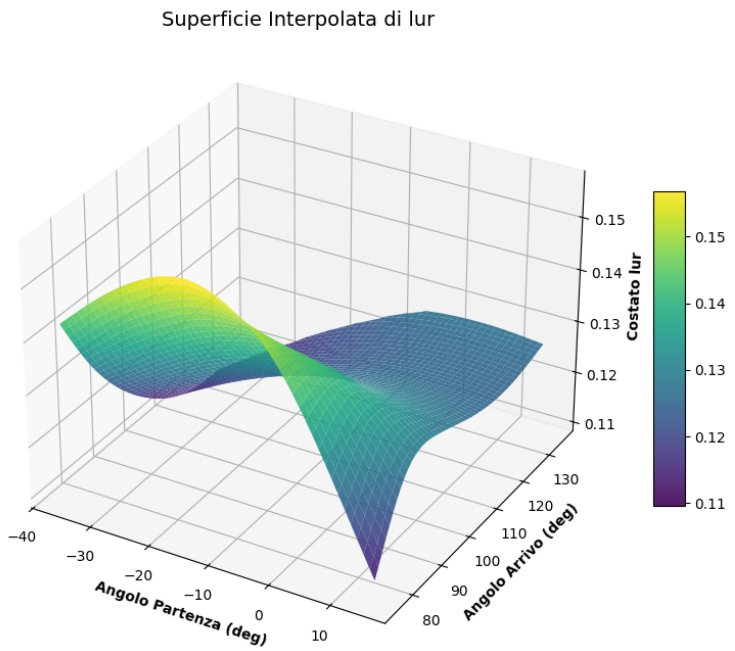

Figure 4.11: λ_{u^r} vs (f_0, f_{tgt})

Observing Figure 4.11, the most interesting feature is the sign of the surface: the values are strictly positive across the entire explored domain. This means that, regardless of the launch window, the initial vector always imparts a strong thrust component directed outward, or towards the positive radial direction. The algorithm determines that, to reach the outer orbit of S31, the absolute priority is to provide kinetic energy to counteract the Schwarzschild gradient. The intensity of this thrust varies in waves: the highest values are recorded far from the pericenter, forcing the engine to compensate for the lack of the Oberth Effect with a much more violent radial force.

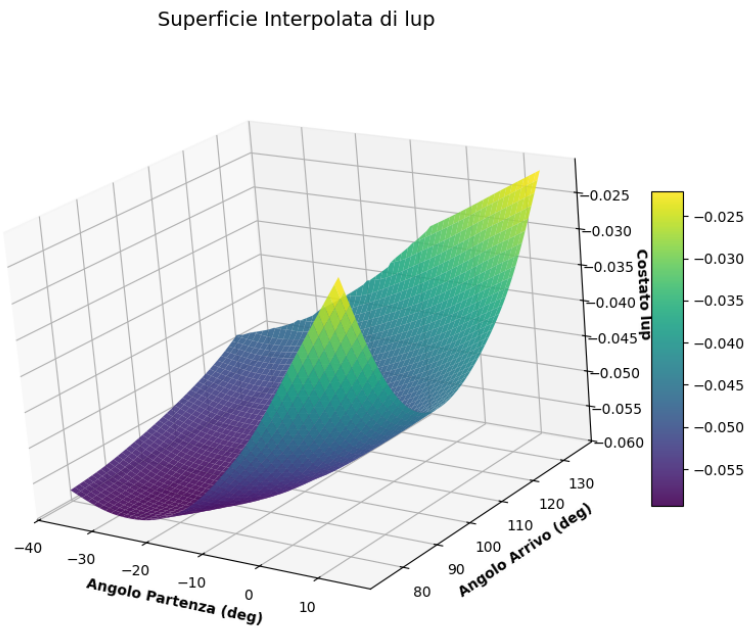

Figure 4.12: λ_{u^ϕ} vs (f_0, f_{tgt})

While radial thrust is used to gain altitude, azimuthal thrust is used to aim at the target. The graph of the azimuthal velocity adjoint variable λ_{u^ϕ} (Figure 4.12 presents a surface entirely characterized by negative values. This reveals a counterintuitive but locally optimal control strategy: the Primer Vector commands the thruster to apply a thrust that partially opposes the vehicle's azimuthal rotation. By reducing the specific angular momentum, the transfer trajectory momentarily tends to fall into a narrower, faster spatial arc, allowing the spacecraft to complete its longitudinal re-phasing, realigning with S31, while the simultaneous massive radial thrust prevents it from plunging into the black hole.

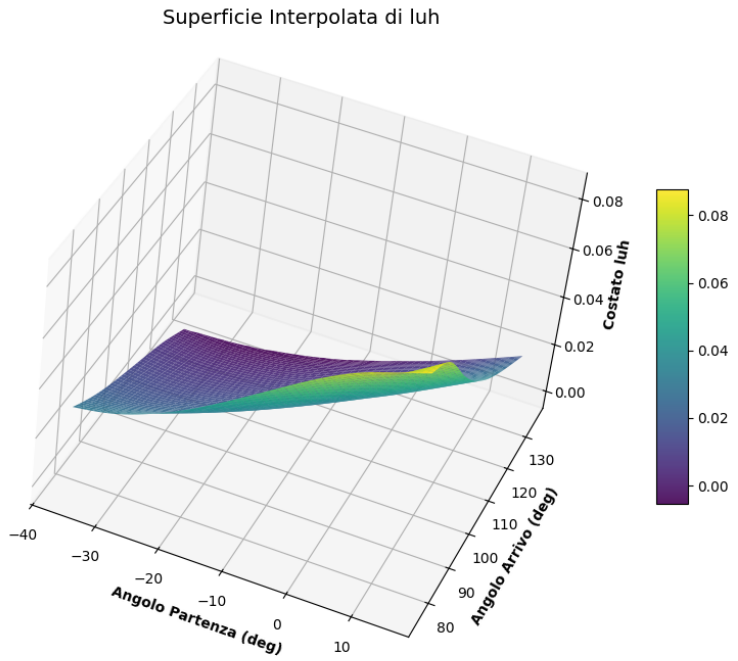

Figure 4.13: λ_{u^θ} vs (f_0, f_{tgt})

Completing the set of three guiding parameters is the component associated with the colatitude velocity, λ_{u^θ}. This parameter governs out-of-plane maneuvers, which are essential for canceling out the three-dimensional spatial misalignment. Unlike the radial and azimuthal components, as can be observed in Figure 4.13 the surface of $\lambda_{u^\theta,0}$ crosses zero, oscillating smoothly between negative and positive values. This alternation of sign is the representation of the correction of the orbital nodes. Although the inclination difference Δi between the stars is small ($\approx 3.2°$), the deviation in the ascending node anomaly forces the spacecraft to perform a targeted plane change. The sign of the polar component at the initial instant depends on where the spacecraft is located relative to the line of the common nodes of the two orbits. The thrust will be directed towards positive or negative values depending on which quadrant the departure occurs. The algorithm spreads the propulsive load of this plane change by integrating it perfectly with the altitude variation, using the natural geometric waves visible in the graph.

The Mass Adjoint Variable λ_m

While the positional and kinematic variables define the geometry of navigation in curved spacetime, the multiplier associated with the vehicle's mass represents its "economic balance". This surface is, quite simply, the most anticipated engineering outcome of the entire variational mapping, as it directly reflects the performance index of the Optimal Control Problem: the maximization of payload or, equivalently, the minimization of propellant consumption (Δm).

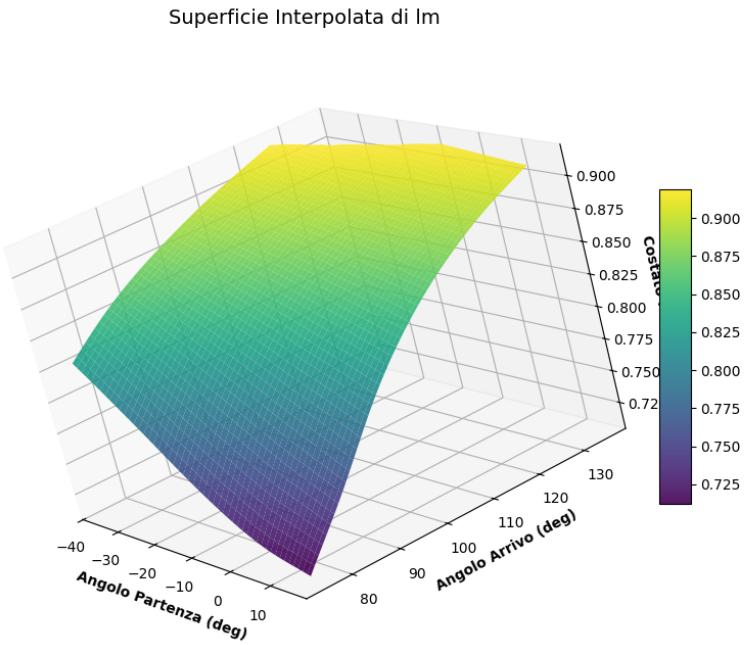

Figure 4.14: λ_m vs (f_0, f_{tgt})

To decode the physical meaning of the graph in Figure 4.14, one has to recall the mathematical framework of Pontryagin's Principle. Optimal Control Theory dictates that, for a problem in which one wishes to maximize the mass state at the final instant, the adjoint variable function must satisfy the transversality condition: at the arrival instant τ_f, its value must be exactly equal to one, thus $\lambda_m(\tau_f) = 1$. However, the graph under consideration does not map the final value, which would be a flat plane at elevation 1 for every convergent simulation, but rather captures $\lambda_{m,0}$, the initial value at the moment of departure. A critical analysis of the three-dimensional surface in 4.14 reveals three levels of advanced astrodynamics:

– Monotonic Integration: The temporal evolution of the mass along the trajectory is not arbitrary, but is strictly governed by its own differential equation.

$$\dot{\lambda}_m = \boldsymbol{\lambda_v} \cdot \frac{F}{m^2} \tag{4.10}$$

Analyzing the terms on the right-hand side of equation 4.10 it is noticeable that: the thrust is zero or positive, the magnitude of the Primary Vector is strictly positive, the square of the mass is positive. Consequently, the derivative $\dot{\lambda}_m$ is always positive. This means that, while the total mass of the spacecraft can only decrease, its adjoint variable can only increase during engine ignition phases (Bang) and remains perfectly frozen and constant during passive inertial flight phases (Coasting).

– Peaks and Valleys: In light of differential equation 4.10, the graph of $\lambda_{m,0}$ turns

out to be an inverse topographic map of consumption. Examining the vertical axis, one notes that the initial values vary gently within a range between ≈ 0.70 and ≈ 0.92. If a specific geometric configuration shows a peak, it means that the solver has calculated an extremely high initial estimate. Starting from 0.92, the variable will need to increase by a mere 0.08 to reach the final constraint of 1. This minimal increase mathematically confirms that the thrust integral will be very small: the engine will be on for only a very short time, the trajectory will make use of natural geodesics, and fuel consumption will be minimal. Conversely, the "valleys", where $\lambda_{m,0} \approx 0.70$, indicate scenarios in which the solver is forced to start from very low values. To bridge a gap of 0.30 and reach 1, the algorithm must accumulate a large derivative, which translates into extended and costly thruster firings.

– Oberth Effect and Orbital Phasing: The smoothness with which the surface transitions from peaks to valleys demonstrates that the mission's efficiency is not the result of algorithmic discontinuities, but instead of an orbital harmony. The ridge of highest values of $\lambda_{m,0}$ runs along a specific diagonal of the domain and represents the set of points where perfect convergence occurs between two astrodynamics factors: the exploitation of kinetic energy at the pericenter and the correct longitudinal alignment with the S31 target. When the departure and arrival angles deviate from this ridge, the gravity of Sagittarius A* ceases to be an ally and becomes an obstacle, forcing the vehicle to expend mass to unnaturally bend its orbit.

To conclude, without the specific need to explicitly calculate or propagate flight time or individual propulsion burns, the inspection of this surface allows for the immediate identification of optimal launch windows, demonstrating the incredible elegance and predictive power of the indirect method applied to astrodynamics.

The Relativistic Imprint $\lambda_{u^t,0}$

From the perspective of theoretical physics, the most fascinating graph is undoubtedly the one relative to the Lagrangian multiplier associated with the temporal component of the four-velocity. In classical space mechanics, time is an absolute, universal parameter independent of motion; consequently, the Euler-Lagrange equations do not include any term for it. In General Relativity, as widely explained, the term $u^t = dt/d\tau$ is the dilation factor linking the coordinate time t of the observer at infinity to the proper time τ marked by the onboard clock and it is, to all intents and purposes, a state variable dynamically coupled to the geometry of spacetime, governed by its own geodesic differential equation and associated with its adjoint variable λ_{u^t}.

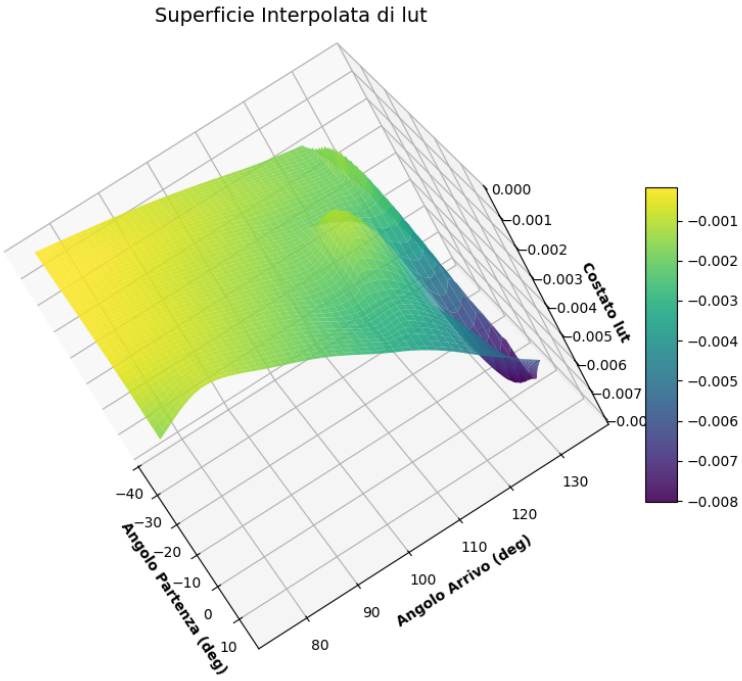

Figure 4.15: λ_{u^t} vs (f_0, f_{tgt})

Analyzing the surface in Figure 4.15 obtained from the parametrization, it reveals several main peculiarities, as it is tangible proof that the algorithm is optimizing the trajectory by taking into account the time dilation predicted by Einstein:

- Magnitude and Variational Sensitivity: The first aspect that catches the eye is the order of magnitude of the vertical axis. The values of $\lambda_{u^t,0}$ are in the range of $10^{-3} \div 10^{-4}$, which is two or three orders of magnitude smaller than other costates, such as λ_r or λ_{u^r}. This discrepancy is not a numerical scaling error, but rather the manifestation of the normalization constraint on the four-vector $g_{\mu\nu}u^\mu u^\nu = -c^2$ (2.43). Since the spacecraft travels at subluminal speeds and at distances where the Schwarzschild field is not yet an extreme black hole ($r \gg R_s$), the term u^t deviates from unity by only decimal fractions. Consequently, the Hamiltonian is numerically less sensitive to a perturbation on u^t than to one on r or u^ϕ. However, the smoothness of the surface demonstrates that the solver consistently incorporates this variable as numerical noise, but actively integrated it into the energy balance of the problem.

- Geodetic Coupling and Christoffel Symbols: The evolution equation for time dilation depends on the Christoffel symbols, specifically $\dot{u}^t = -2\Gamma^t_{tr}u^t u^r$. The variation in proper time is therefore linked to the vehicle's radial velocity u^r and the depth within the gravitational well via Γ^t_{tr}. Observing the graph, one notices a dip and a diagonal rise that almost perfectly mirror the map of the true anomalies. When the spacecraft departs from f_0 near the pericenter, where the gravity of Sgr A* is strongest and u^t reaches its local maximum, the variational penalty imposed by the adjoint variable

changes abruptly: applying thrust in that region will modify trajectory entering regions that will cause the onboard time to lag behind universal time.

- The Hamiltonian Balance $\mathcal{H} = 0$: From a perspective purely related to Free-End-Time Optimal Control Theory, the Hamiltonian of the system must remain identically zero throughout the entire trajectory. The λ_{u^t} function acts as the balancing mechanism of this equation. Its smooth yet clearly structured variation along the grid (f_0, f_{tgt}) ensures that the optimality condition $\mathcal{H} = 0$ is perfectly satisfied at the initial instant τ_0, absorbing any micro-variations induced by time dilation.
- Physical Trade-off on Consumption: Propellant consumption Δm is calculated by integrating the mass flow rate with respect to proper time τ. If the spacecraft maneuvers in a region of extremely high curvature, where dt is much longer than $d\tau$, the relationship between geometric orbital progress and fuel burned becomes distorted. The three-dimensional surface of $\lambda_{u^t,0}$ precisely represents the penalty that the solver assigns to this phenomenon: the algorithm penalizes trajectories that require long propulsion burn times in regions of extremely high time dilation, unless the increase in velocity at pericenter compensates for this distortion.

The visual and mathematical synthesis of these surfaces confirms the total variational dominance of the developed algorithm. Having exposed the hidden anatomy of the indirect solutions, the study prepares for its final act: the finding of the single combination (f_0, f_{tgt}) capable of guaranteeing the maximum efficiency peak.

4.2.6 The Optimum Transfer of the S29–S31 Mission

Following the rigorous mapping of space and the morphological analysis of variational manifolds, the final procedural step involved the computation of propellant cost for each node of the explored grid. The minimum of the cost metric and so the maximization of the final mass m_f occurs at a departure from star S29 at a true anomaly $f_0 = -5.0°$ and a rendezvous with star S31 at an anomaly $f_{tgt} = 135.0°$. The exact physical parameters, recorded by the solver at the moment of interception, outline a mission profile of exceptional efficiency:

Parameter	**Value**
Departure True Anomaly f_0	$-5.0°$
Target True Anomaly f_{tgt}	$135.0°$
Flight Time τ_f	5.937120 TU
Time Dilation u_f^t	1.000014
Final Mass m_f	0.921697
Propellant consumed Δm	0.078303 (7.83%)

Table 4.4: Physical and performance normalized parameters of the global optimum for mission S29–S31

Analysis of this specific trajectory (whose complete graphical output is shown in Figure 4.16) allows to examine the physical and astrodynamic reasons that make this configuration the most advantageous of all possible solution families.

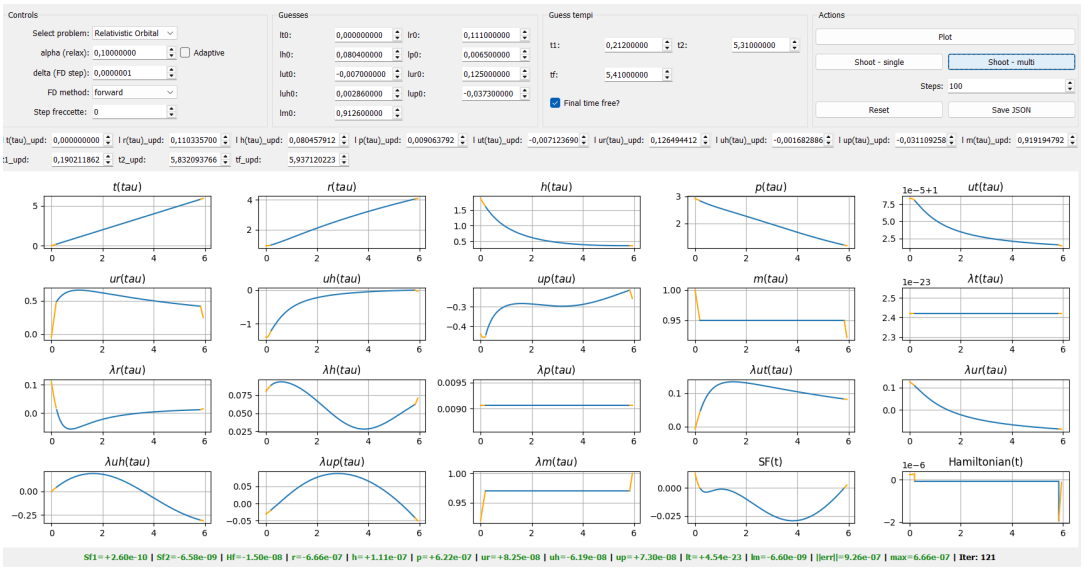

Figure 4.16: Full Convergence of the $-5° \rightarrow 135°$ Transfer

To immediately grasp the spatial architecture of this optimal solution, Figure 4.17 translates the numerical convergence into a three-dimensional map. The plot highlights the actual trajectory connecting the departure from S29 to the rendezvous with S31, visually distinguishing the active thrust phases (Initial and Final Bang, in red) from the extended relativistic geodetic flight (Coasting arc, in dotted gray).

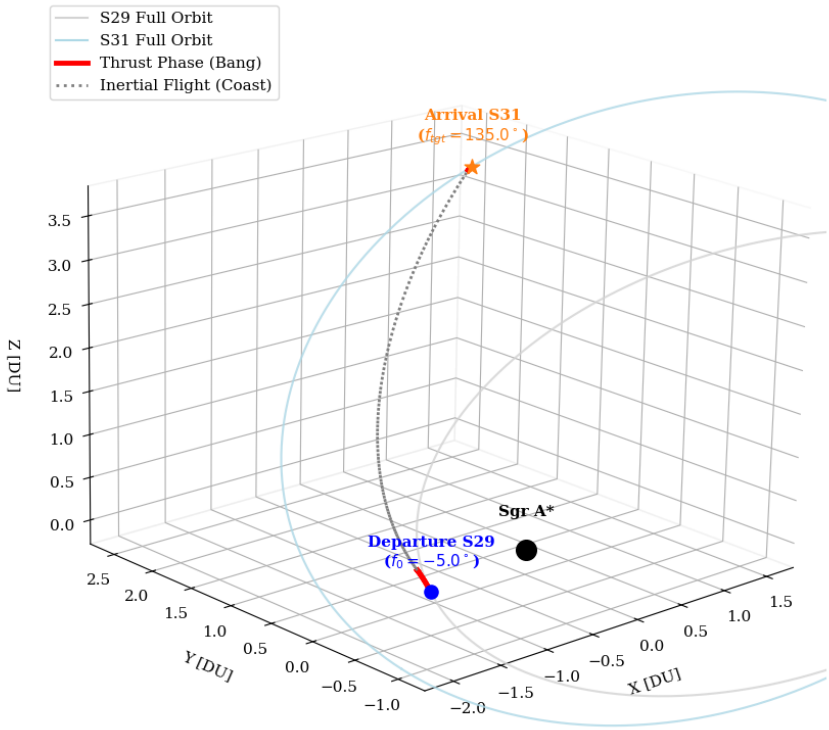

Figure 4.17: 3D map of the true optimal transfer trajectory

The mathematical core of the entire work lies in the identification of the initial adjoint variables vector $\boldsymbol{\lambda}_0$. Convergence of the indirect method solver for the optimum was achieved by isolating the following exact sequence of Lagrange multipliers:

Adjoint Variable	Initial Guess for Convergence
$\lambda_{t,0}$	0.0
$\lambda_{r,0}$	0.1103357
$\lambda_{\theta,0}$	0.080457912
$\lambda_{\phi,0}$	0.009063792
$\lambda_{u^t,0}$	-0.00712369
$\lambda_{u^r,0}$	0.126494412
$\lambda_{u^\theta,0}$	-0.001682886
$\lambda_{u^\phi,0}$	-0.31109258
$\lambda_{m,0}$	0.919194792

Table 4.5: Adjoint Variables Initial Guesses Vector $\boldsymbol{\lambda}_0$ for the Optimal Trajectory

These values do not represent just algebraic coefficients but encode the entire navigation strategy. Their extreme numerical sensitivity reveals the highly nonlinear nature of the coupled geodesic equations in the Schwarzschild metric. The string shown in Table 4.5 therefore constitutes the exact key for reproducing the ideal interstellar transfer S29-S31 targeted.

Orbital Synchronization and the Relativistic Oberth Effect

The first point of investigation concerns the geometric and kinematic timing of the departure. Escaping the gravity of S29 at $f_0 = -5°$ means firing the thrusters instants before passing through the pericenter of the orbit, which is not a fortuitous numerical coincidence, but rather the computational manifestation of the famous Oberth Effect translated into a strong-field relativistic regime. In astrodynamics, the increase in specific orbital energy provided by a propulsive impulse is directly proportional to the instantaneous velocity of the vehicle. Near the pericenter, the star S29 and consequently the vehicle orbiting around it, travels at its maximum orbital velocity, plunging into the minimum point of Sagittarius A*'s gravitational potential. Delivering the ΔV at this exact moment maximizes thrust efficiency: the mechanical work performed by the engine adds up to the velocity already possessed. The algorithm independently identified this intrinsic "gravitational slingshot": the energy gained at the pericenter is sufficient to project the spacecraft onto a transfer geodesic bridging the steep radial height difference to the S31 orbit with minimal propulsive effort. At the same time, arrival at $f_{tgt} = 135°$ ensures perfect geometric phasing: the spacecraft intercepts S31 in a region where the velocity vectors of the two orbits are sufficiently aligned, minimizing the targeting cost of the final braking maneuver.

The Bang-Coast-Bang Profile and the Asymmetry of the Switching Function

The most astonishing engineering result of the research is the fraction of propellant required to accomplish this interstellar rendezvous. Bridging the orbital gap while consuming only 7.83% of the initial mass is a formidable achievement, made possible exclusively by the perfect control architecture outlined by the variational algorithm.

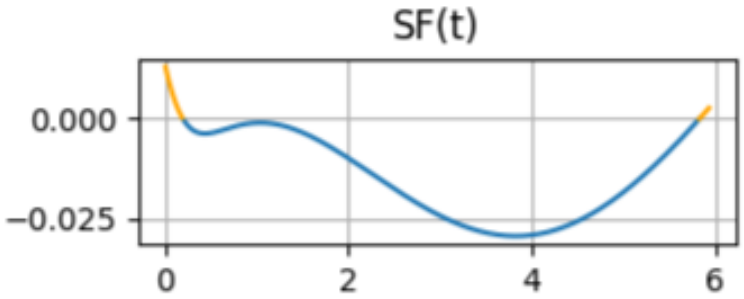

Figure 4.18: Switching Function $\mathcal{S}_\mathcal{F}$

The analysis of the Switching Function $\mathcal{S}_\mathcal{F}$, whose graph is shown in Figure 4.18, reveals the algorithmic engine behind this efficiency: in this relativistic scenario the curve exhibits a profoundly asymmetric shape, crossing the x-axis at two precise points and defining a strict Bang-Coast-Bang (1-0-1) temporal structure:

1. Escape and Injection: At the initial bang, $\mathcal{S}_\mathcal{F}$ is not only positive but also reaches its peak absolute magnitude. The thruster is pushed to its maximum level T_{max} for an initial fraction of time of approximately 0.19 TU. This impulse is concentrated at the moment of maximum depth in the gravitational well, where $r \approx 0.93\,DU$: the

high magnitude of $\mathcal{S}_{\mathcal{F}}$ reflects the need to deliver a violent ΔV to escape the extreme local curvature, raising the apocenter and simultaneously varying the inclination.

2. Passive Flight on a Geodesic: As soon as $\mathcal{S}_{\mathcal{F}}$ crosses zero, the engine is shut down completely and the Coasting Arc begins, a very long inertial phase, spanning nearly the entire duration of the transfer ($\approx 5TU$). This connecting trajectory is not a Keplerian transfer ellipse, but a complex Schwarzschild geodesic and the spacecraft moves passively within a curved spacetime, where the algorithm naturally calculates and compensates for purely relativistic phenomena, such as the precession of the pericenter. During this extended arc, the spacecraft does not expend a single drop of propellant.

3. Final Bang and Relativistic Asymmetry: In the very last moments before τ_f, the Switching Function abruptly turns positive again to trigger the rendezvous maneuver. However, careful observation of the graph reveals a clear asymmetry with respect to the initial momentum: the curve rises sharply but failing to reach the magnitude peaks seen at the start. As the vehicle has climbed along the gradient of the gravitational well up to $r \approx 4.08\,DU$, the local acceleration of the gravitational field and the spacetime curvature have decreased. The Primer Vector detects a much flatter environment and requires significantly less control effort to dampen the residual velocity and synchronize with the target.

Theoretical Validation: The Hamiltonian

The mathematical certainty that this Bang-Coast-Bang sequence represents the optimum for the physics of the problem is provided by examining the Hamiltonian $\mathcal{H}$ (Figure 4.19).

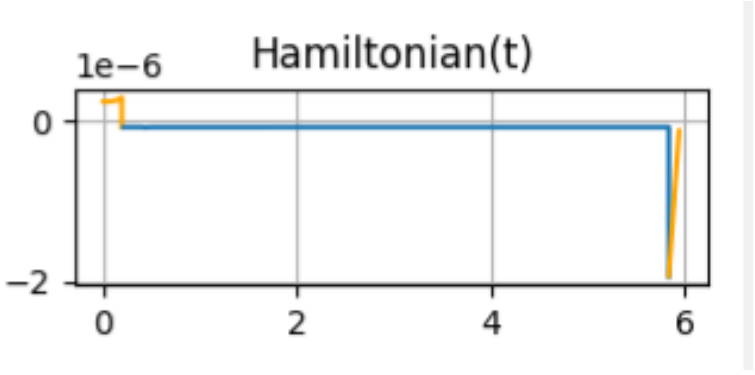

Figure 4.19: Hamiltonian $\mathcal{H}$

Since this is a final time free optimization problem, the Maximum Principle dictates that the Hamiltonian must be a motion constant that is identically zero. The graph confirms that, despite the variations in position and velocity, $\mathcal{H}$ remains strictly confined within a numerical noise band. This stability, pushed to the physical limit of machine double-precision, certifies that the algorithm has calculated the transfer while strictly adhering to the relativistic energy conservation laws imposed by the Schwarzschild metric tensor.

Consumption Dynamics: The Evolution of Mass

Among all the outputs provided by the OCULUS validation interface, the graph dedicated to the temporal evolution of the physical mass is shown in Figure 4.20. This graph represents the mission's efficiency and provides definitive proof that the numerical propagator has strictly followed the laws of Optimal Control Theory.

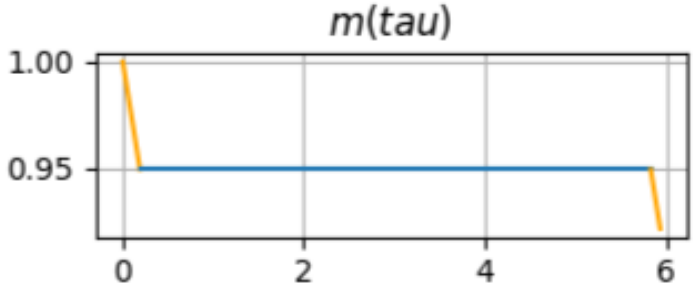

Figure 4.20: Mass vs τ

Observing the blue curve relating to the state of the mass, one immediately notices the signature of a Bang-Bang control. Starting from the normalized value of $m_0 = 1.0$, the mass does not decrease linearly or continuously but undergoes two phases separated by a vast plateau. During the initial fraction of the flight time the curve drops vertically and in this brief time span, the vehicle burns approximately 5% of the propellant. This great and sudden energy expenditure is the price to pay for escaping the region of highest curvature in the gravitational well of Sagittarius A* and providing the energy needed to trigger the transfer. The last burn, starting at $\tau_2 = 5.832\,\text{TU}$ causes a lower mass drop and propellant expenditure, reaching the final adimensional value of $m_f = 0.9216$. This demonstrates that the spacecraft, having now ascended into a much flatter spacetime region and having passively exploited gravity to curve its trajectory toward S31, requires a very small kinematic correction to complete the rendezvous.

Navigation in Curved Spacetime: The Evolution r, θ, ϕ

In Figure 4.21 can be observed the plots of the temporal evolution of the vehicle's three spatial coordinates. Analyzing these curves allows the vizualitazion of the exact three-dimensional trajectory calculated by the solver.

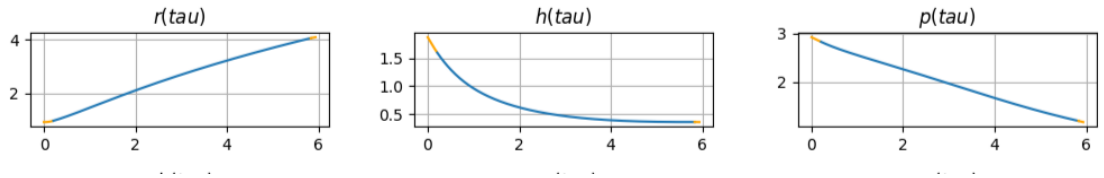

Figure 4.21: Evolution of r, θ, ϕ, vs τ

1. **The Radial Coordinate** r

   The radial distance curve represents the energetic heart of the mission. The spacecraft

starts from an altitude deeply sunk in the gravitational well ($r \approx 0.93\,DU$) and must reach the more stable orbit of S31 ($r \approx 4.08\,DU$). The graph shows that r is a monotonic function, gradually and slowly increasing for the entire transfer. During the final burn, the gravitational pull of Sgr A* slows the ascent, converting kinetic energy into potential energy and allowing the spacecraft to reach the final altitude with minimal residual velocity.

2. **Azimuthal Tracking** ϕ
   The curve representing the azimuthal angle ϕ describes the trajectory's wrap around the black hole. Unlike the radius, this curve is constantly decreasing.

3. **Colatitude** θ
   Finally, the colatitude curve reveals the three-dimensional aspect of the mission. Since the two stars do not lie exactly in the same plane, the trajectory cannot be purely equatorial. The solver calculated an initial Primer Vector that imparts the correct out-of-plane velocity component to the vehicle. After the initial impulse, the θ curve evolves passively, gently bringing the transfer orbital plane to coincide exactly with the colatitude of S31 at the arrival time τ_f. This distributed management of out-of-plane error avoids heavy and extremely costly corrective maneuvers.

Relativistic Kinematics: u^r, u^θ, u^ϕ

The graphs in Figure 4.22 illustrate the temporal evolution of the three spatial components of the four-velocity. These graphs represent where the acceleration imparted by the nuclear propulsion system collides and merges with the geodetic accelerations ruled by the Christoffel symbols.

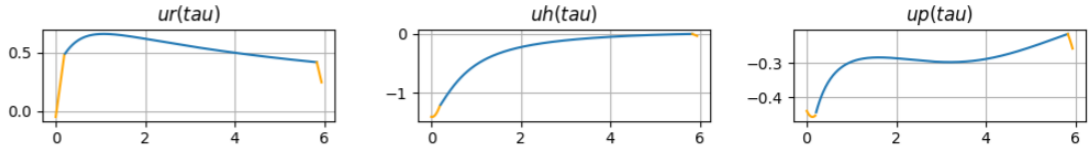

Figure 4.22: Velocity u^r, u^θ, u^ϕ vs τ

Unlike the position state, the velocity graphs exhibit distinct edges or sharp inflection points at the exact switching times τ_1 and τ_2. Since the solver has implemented a Bang-Bang logic, the engine thrust is described by a step function and, because acceleration is the derivative of velocity ($\dot{u}^\mu$), a step discontinuity in acceleration mathematically imposes a discontinuity in velocity. The sharpness of these edges attests to the exceptional stability of the numerical integrator. The radial velocity u^r curve shows a sharp slope at time τ_0, a direct measure of the acceleration imparted to break free from the gravitation of Sgr A*. When the engines shut down, the long coasting phase begins, during which the curve takes on a constant and very gentle negative slope. The intense gravity of the black hole acts as a continuous brake, progressively reducing radial velocity The component $u^\theta(\tau)$ initially takes on large negative values and decreases monotonically toward zero without oscillations. This behavior indicates a strong initial correction required to satisfy the dynamic constraints

and the optimality conditions, and to correctly perform the out-of-plane thrust necessary to complete the plane change. The subsequent asymptotic approach to zero suggests a progressive relaxation of the control, consistent with the gliding of the vehicle in the third dimension to cancel the polar velocity exactly at the moment of interception, accomplishing the change of plane without having to perform to costly maneuvers midway through the journey. The third graph shows the component $u^{\phi}(\tau)$ that exhibits a less pronounced but still significant behavior: after an initial minimum, it increases rapidly and stabilizes at nearly constant values, with a slight variation in the final phase. This trend is consistent with an initial adjustment of the angular dynamics, followed by a quasi-steady-state phase. The slight final variation can be interpreted as a correction necessary to satisfy the boundary conditions in the final configuration $S31$. This structure is consistent with the theory of optimal control in the presence of nonlinear dynamic constraints and boundary conditions, and confirms the effectiveness of the solution obtained in minimizing the functional cost associated with the transition between configurations $S29$ and $S31$.

Dynamics of the Temporal Component of the Four-Velocity u^t

The graph depicting the evolution of the state u^t (4.23 captures the vehicle's journey through time. In classical physics, this ratio would be exactly equal to 1; within the adopted Schwarzschild relativistic framework, u^t is a dynamic and fluctuating state variable.

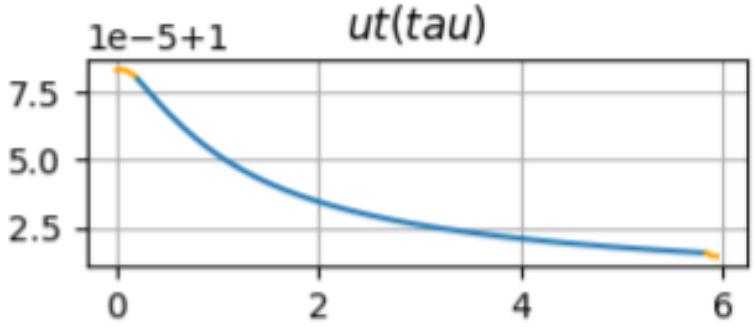

Figure 4.23: u^t vs τ

At the moment of departure, the curve is at its absolute maximum and this deviation from unity is the result of the greatest relativistic severity of the entire journey, due to the superposition of two phenomena happening at the same moment: Gravitational Time Dilation, because as the vehicle has plunged into the gravitational well $g_{tt} = -(1 - \frac{R_s}{r})$ and the clocks run slower, and Kinematic Time Dilation, because the vehicle is traveling at its maximum orbital velocity at perigee. Once the initial burn has passed, the curve shows a monotonically decreasing curve throughout the Coasting Arc. As the spacecraft navigates towards the orbit of S31, the curvature term relaxes and, simultaneously, the spatial velocity decreases. The result of these two decelerations is that local time gradually resume its flow at a rate that increasingly resembles that of coordinate universal time. Moreover, like the velocity components, the graph of u^t also exhibits slight but perceptible changes in slope when the engines are turned on and off. This phenomenon demonstrates

the normalization constraint of the velocity four-vector: when the engine provides thrust, it alters the spatial velocities and in order for the norm of the four-vector to remain invariantly equal to $-c^2$, the temporal component u^t is forced to adapt instantaneously, modifying its rate of change.

In conclusion, the anatomy of this ideal transfer confirms the reliability of the developed optimization framework. The indirect approach has proven to not only being capable of overcoming the instability of the Schwarzschild metric, but it has decoded its secrets, exploiting time dilation and relativistic gravitational slingshots to undertake an interstellar journey at a propulsive cost that would otherwise be unimaginable. From an engineering perspective, the results obtained and explained highlight that relativistic effects are not merely corrections to the trajectory but actively influence the optimal control structure. The inclusion of time dilation in the variational framework leads to propulsion strategies that are adapted to spacetime geometry, further confirming the necessity of a fully relativistic formulation for accurate trajectory design in strong gravitational fields.

4.2.7 Translation into Physical Quantities and Engineering Feasibility of the Mission

Although the entire simulation and numerical optimization was rigorously conducted in the dimensionless domain, the engineering interpretation of the mission requires a tangible translation into the International System of Units. The concluding subsection of this study is therefore dedicated to translating the optimal trajectory results into measurable physical quantities, in order to assess its operational feasibility in the context of advanced interstellar astrodynamics. By restoring the dimensional constants used during initialization, the parameters provided by OCULUS take on an engineering significance of extraordinary concreteness:

Mission Duration

The dimensionless flight time $\tau_f = 5.937\,\mathrm{TU}$ translates to a journey lasting approximately 14.96 years. This timeframe represents an exceptional milestone from a mission planning perspective. Although the orbits of S29 and S31 are separated by billions of kilometers, the solver has identified a trajectory that can be completed in less than fifteen years. This timeframe is fully compatible with the operational lifespans of modern robotic probes, such as Cassini or New Horizons, and ensures that the payloads will not become technologically obsolete between launch and interception.

Delta-V and Mass Consumption

The model was set to an extremely high propellant exhaust velocity: $v_e = 0.05\,c$, equal to approximately 14989 km/s, consistent with nuclear fusion propulsion systems, considered the only physically suitable propulsion systems for deep-space navigation in the S-Cluster, as exposed in Chapter 2. By applying the Tsiolkovsky's rocket equation to the mass change extracted by the optimizer, it is possible to derive the effective kinematic cost of the maneuver:

$$\Delta V = v_e \ln\left(\frac{m_0}{m_f}\right) \tag{4.11}$$

Substituting the mass values, the transfer requires a total propulsion budget of $\Delta V \approx 1,222\,\text{km/s}$. While this value would be impossible for conventional chemical or thermonuclear propulsion, it is fully in line, and even conservative, for the simulated fusion architectures. The negligible consumption of 7.83% of the spacecraft's full-load mass ensures that the remaining payload can be largely dedicated to life support systems, thermal-radiative shields for proximity to Sgr A*, and massive astrophysical research instruments.

Actual Propulsion Phases

When instantly scaled to actual dimensions, the mission's propulsion phase reveals the importance of the Oberth Effect being utilized. Of the nearly 15 years of travel, the total reactor burn time (Initial Bang plus Final Bang) covers approximately 275 days. For the remaining time span, the vehicle glides through space with its engines completely shut down. The heat generated by the reactor and the thermal wear on structural materials are thus minimized, maximizing the vehicle's long-term reliability.

Table 4.6 summarizes all the values of the optimal results obtained for the S29-S31 transfer.

Parameter	**Value**
Departure True Anomaly f_0	$-5.0°$
Target True Anomaly f_{tgt}	$135.0°$
Total Flight Time τ_f	14.96 years
First Burn Time τ_1	175.05 days
Coasting Arc Time $\tau_1 \to \tau_2$	14.22 years
Final Burn Time $\tau_2 \to \tau_f$	96.65 days
Time Dilation u_f^t	1.000014
Exhaust Velocity v_e	14989.62 km/s
Delta V ΔV	1222.23 km/s
Initial Mass m_0	1000 kg
Final Mass m_f	921.697 kg
Propellant consumed Δm	78.303 kg (7.83%)

Table 4.6: Results for Mission S29–S31

To conclude, the conversion into physical units closes the simulation done for the thesis. The trajectory obtained defines, based on physical data, the conceptual design of an interstellar mission that is both energetically sustainable and chronologically feasible. The combination of the natural geodesic path discovered by the continuation method and the reduced fuel consumption of a low-thrust continuous propulsion technology unequivocally demonstrates the feasibility of autonomous exploration in the vicinity of the event horizon.

Chapter 5

Conclusions and Future Developments

The conceptualization of interstellar spaceflight in the vicinity of supermassive black holes represents a great challenge in modern astrodynamics. In such extreme environments, the fundamental laws of classical celestial mechanics cease to be valid, because of the severe geometric distortions of spacetime dictated by General Relativity. With this thesis, a mathematical and computational investigation has been carried out to bridge the historical gap between theoretical relativistic astrophysics and the practical optimization of spacecraft trajectories.

By selecting the S-Stars cluster surrounding Sagittarius A* as the ultimate operational laboratory, this work demonstrated that navigating such hostile gravitational well in the galaxy is not a theoretical curiosity, but a solvable engineering problem. The following sections summarize the methodological milestones achieved in this research, analyzing the physical and astrodynamical implications of the numerical results, and outlining the future developments necessary to fully master autonomous relativistic navigation.

5.1 Summary of the Research and Key Achievements

To reach the established objectives, the research was structured through a progressive increase in physical modeling and numerical complexity, leading to the following key methodological and applied achievements.

The first major milestone was the formulation of a complete 9-dimensional state-space model based on the exact solutions of the perturbed equations of motion in the Schwarzschild metric. The spacecraft's kinematics were elevated from classical 3D vectors to four-position and four-velocity tensors. A critical consideration in this phase had to be done regarding time, as it is an active, independent dynamic variable: the chronological decoupling between the coordinate time t of a distant observer and the proper time τ measured onboard the spacecraft was actively propagated. To guarantee the numerical stability of the integrator, the entire system underwent a normalization process. By scaling distances, velocities, and time relative to the astrophysical environment, specifically

adopting the Schwarzschild radius (R_s) for free-fall scenarios and the S2 star semi-major axis as the Distance Unit (DU) for the transfer, the framework successfully prevented machine precision saturation. Operating simultaneously with central masses on the order of 10^{36} kg and velocities approaching the speed of light would have otherwise triggered round-off errors and Jacobian matrix divergences. The robustness of this physics engine was successfully validated through the integration of purely geodetic free-fall trajectories. The solver flawlessly reproduced relativistic phenomena, accurately mapping the phenomenological collapse at the Innermost Stable Circular Orbit boundary. Furthermore, it smoothly handled the mathematical singularity approaching the event horizon, recording extreme gravitational time dilation factors nearing 99.36 without incurring violations of the four-dimensional norm or integration instabilities.

Moving beyond natural geodesic motion, the research successfully formalized the continuous-thrust trajectory planning within the boundaries of the Optimal Control Theory and as a highly complex Boundary Value Problem through the application of Pontryagin's Maximum Principle. The control Hamiltonian in General Relativity has been derived, as well as the full set of Christoffel symbols $\Gamma^{\alpha}_{\beta\gamma}$, and the exact differential equations governing the evolution of the nine adjoint variables $\boldsymbol{\lambda}$. This expansion resulted in an 18-dimensional coupled differential system. This formulation allowed for the precise mathematical definition of the Relativistic Primer Vector. Instead of relying on arbitrary user-defined steering laws, the Primer Vector autonomously dictated the optimal thrust direction instant by instant. Concurrently, the mass adjoint variable λ_m and the Switching Function ($\mathcal{S}_{\mathcal{F}}$) governed the thrust magnitude, spontaneously generating efficient Bang-Coast-Bang control profiles . The exceptional stability of the Hamiltonian, which remained identically zero $\mathcal{H} = 0$ throughout the free-end-time optimization, definitively certified the physical and mathematical validity of the developed optimal control architecture.

Solving an 18-dimensional Boundary Value Problem in a highly nonlinear curved spacetime poses a severe computational challenge. Due to the chaotic geometric topology introduced by the supermassive black hole's metric tensor, the domain of attraction for the initial guess vector of the adjoint variables $\boldsymbol{\lambda}_0$ is very small. Providing the solver with a random initialization inevitably leads to divergence, scattering the trajectory into the event horizon or into unbound escape paths. This critical mathematical rigidity was overcome by implementing a continuation strategy within the Oculus solver: this optimization architecture was instructed to progressively tighten the boundary constraints through a defined sequence starting from a simplified one-dimensional radial intersection to a complete 3D spatial position match, and ultimately imposing the strict four-velocity kinematic rendezvous. This step-by-step approach allowed the algorithm to gradually build the exact control logic required to arrive at the target with the exact position and velocity vector perfectly aligned. Furthermore, the solver was not limited to identifying a single local optimum. An extensive parametric grid-search was conducted across the true anomalies of departure and arrival (f_0 and f_{tgt}), in order to generate three-dimensional variational manifolds for the adjoint variables . The absolute morphological smoothness of these surfaces provided a double validation of the framework: mathematically, it certified

that the solver consistently converged to neighboring solutions without jumping between uncorrelated local minima, proving that the algorithm successfully traced a coherent family of active geodesics, highly sensitive and adapted to the underlying curvature of spacetime.

The finale part of the work consisted in the extraction of the absolute global optimum for a continuous-thrust orbital transfer between the stars S29 and S31. By evaluating the computed mass consumption for each node of the explored parametric grid, the absolute minimum propulsive expenditure was identified for a departure at a true anomaly of $f_0 = -5^\circ$ and a target interception at $f_{tgt} = 135^\circ$. Operating a simulated advanced Fusion propulsion architecture with an effective exhaust velocity of $0.05c$, the solver found an asymmetric Bang-Coast-Bang control sequence.

The relativistic equivalent of the Oberth Effect was identified: the Initial Bang was triggered deep in the potential well, just instants before passing the pericenter, delivering a violent ΔV exactly when the spacecraft's orbital velocity was maximized to efficiently escape the extreme local curvature. This was followed by a vast Coasting Arc, spanning nearly the entire duration of the transfer, during which the vehicle moved passively along a complex Schwarzschild geodesic without expending any propellant. Finally, a much smaller Final Bang was commanded in a flatter spacetime region to synchronize with the target. The resulting transfer bridges the immense spatial and energetic gap between the two highly eccentric orbits in a flight time of 14.96 years. Most remarkably, the maneuver requires consuming a mere 7.83% of the initial spacecraft mass, translating to a kinematic cost (ΔV) of approximately 1222 km/s. This result demonstrates that, when propelled trajectories are rigorously coupled with continuous Optimal Control Theory, autonomous interstellar navigation in the vicinity of Sagittarius A*'s event horizon is not only mathematically solvable but also energetically sustainable and chronologically feasible for future spaceflight architectures.

5.2 Future Developments and Research Perspectives

The mathematical framework and the numerical results achieved in this thesis establish a solid foundation for the analysis of propelled trajectories in strong gravitational fields. However, the extreme non-linearity of relativistic astrodynamics leaves ample room for further theoretical expansion and algorithmic refinement.

Exploration of Multi-Burn Families: The $1-0-1-0-1$ Control Structure

The global optimum identified for the S29-S31 interstellar transfer in this study is characterized by a three-phase Bang-Coast-Bang $(1-0-1)$ control structure. While this topology proved to be remarkably efficient by maximally exploiting the relativistic Oberth effect at the departure pericenter, Optimal Control Theory dictates that highly non-linear differential systems can have multiple extremal solutions. These local minima satisfy all the necessary conditions of Pontryagin's Maximum Principle for the exact same physical boundary conditions but exhibit completely different temporal switching structures. A fundamental future development of this research involves the systematic investigation of

higher-order multi-burn trajectories, specifically focusing on the five-phase Bang-Coast-Bang-Coast-Bang $(1-0-1-0-1)$ solution family. From a mathematical perspective, this topology occurs when the initial adjoint variables vector is calibrated such that the Switching Function $\mathcal{S}_{\mathcal{F}}$ crosses the zero axis exactly four times during the integration time τ_f.

Physically, a $1-0-1-0-1$ control architecture represents a trajectory that relies on a mid-course correction maneuver. Instead of executing a single, massive initial slingshot deep within the potential well, the solver distributes the required ΔV across an initial injection burn, a secondary adjustment burn in the intermediate spacetime region, and a final synchronization burn. A first result of this specific shape of the Switching Function, driving the thruster through three distinct active burns separated by two passive geodetic arcs, has been computed and it is illustrated in Figure 5.1.

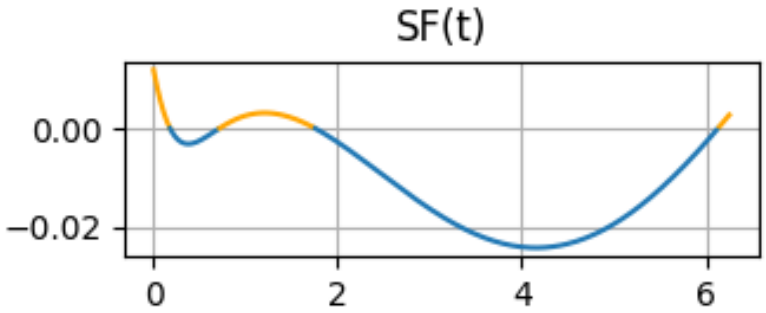

Figure 5.1: 1-0-1-0-1 Switching Structure

After this single initial guess vector is isolated and validated, ensuring the Hamiltonian remains identically zero, the continuation methods adopted in this thesis must be applied to propagate this new topological family across the entire (f_0, f_{tgt}) anomaly grid. This extensive mapping process would generate a parallel set of three-dimensional variational manifolds. The ultimate objective of this future study would be to conduct a rigorous cross-examination between the two solution families. To conclude, by directly comparing the resulting propellant mass fractions Δm, the time dilation u^t, and the total proper time of flight (τ_f) for every single node of the grid, it would be possible to conclusively determine the absolute theoretical global optimum. This comparative analysis would definitively answer the question of whether breaking the propulsive effort into intermediate burns in flatter spacetime regions is energetically superior to having a single, continuous initial impulse.

Extension to the Kerr Metric: Rotating Spacetime

The dynamic model formulated and validated in this thesis relies on the Schwarzschild metric, which provides an exact mathematical solution for a static, non-rotating spherically symmetric mass. While this assumption is exceptionally robust for establishing the foundational architecture of relativistic optimal control, astrophysical observations strongly suggest that Sagittarius A*, like the vast majority of supermassive black holes, possesses a significant angular momentum. To elevate the simulation framework to a higher level

of astrophysical fidelity, the entire mathematical and algorithmic architecture must be upgraded to operate within the Kerr metric.

Transitioning to a rotating singularity introduces geometric and analytical complexities into the Optimal Control Problem. Unlike the Schwarzschild spacetime, the covariant Kerr metric tensor $g_{\mu\nu}$ loses its purely diagonal form and acquires critical off-diagonal components, particularly the $g_{t\phi}$ term, which creates a mathematical coupling between the temporal coordinate t and the azimuthal spatial angle ϕ. This geometric distortion exponentially increases the algebraic complexity of the complete set of Christoffel symbols $\Gamma^{\alpha}_{\beta\gamma}$ and, consequently, the analytical derivation of the Hamiltonian $\mathcal{H}$ and the associated 18-dimensional differential system would require a complete and highly non-linear reformulation.

The presence of the $g_{t\phi}$ term mathematically translates into the physical phenomenon known as frame-dragging, or the Lense-Thirring effect. In this regime, the immense rotation of the black hole literally drags the surrounding spacetime along with it, creating a vast spacetime vortex that culminates in the boundary of the ergosphere. This dynamic rotation completely shatters the spherical symmetry of classical orbital mechanics: prograde orbits (co-rotating with the black hole's spin) and retrograde orbits (counter-rotating) no longer share the same specific energy states, orbital periods, or Innermost Stable Circular Orbit (ISCO) boundaries. As a consequence, for a spacecraft, moving "with the current" or "against the current" of spacetime requires different propulsive efforts.

For a continuous-thrust optimization solver, this asymmetric topology offers an interesting opportunity: by using the Kerr metric tensor into the indirect optimization environment, the algorithm could be trained to actively sense and exploit the spacetime vortex. The variational algorithm would autonomously design trajectories that intentionally sail along the frame-dragging currents, executing prograde injection burns to receive a massive, propellant-free velocity boost derived directly from the angular momentum of the singularity. On the other hand, the mass adjoint variable λ_m would penalize retrograde maneuvers that force the nuclear fusion thruster to consume payload just to fight the rotational tide of the universe.

Ultimately, extending the framework to the Kerr metric would not only refine the research for the S-Cluster missions, but it would also pioneer entirely new classes of relativistic orbital maneuvers and reveal several stronger relativistic effects to be studied. It would allow the simulation of advanced techniques such as ergospheric gravity assists where a spacecraft could theoretically extract orbital energy directly from the black hole's rotation, achieving transfer efficiencies that have no equivalent in classical Newtonian celestial mechanics.

Multi-Body Perturbations and Relativistic N-Body Trajectory Design

The optimal control framework developed in this thesis successfully models the spacecraft navigating the unperturbed, isolated Schwarzschild spacetime generated by Sagittarius A*. While this idealization is acceptable for capturing the dominant relativistic dynamics, the physical reality of the Galactic Center is different. The S-Cluster is a dense and chaotic

stellar environment, populated by dozens of massive B-type main-sequence stars moving at high velocities. To transition this trajectory design tool from a theoretical proof-of-concept to a high-fidelity mission planning simulator, the mathematical architecture must be expanded to account for multi-body gravitational perturbations.

Modeling an N-body environment means incorporating the gravitational pull of passing stars, such as S2 or S8, and it requires abandoning the pure Schwarzschild exact solution in favor of approximated analytical frameworks, such as the Post-Newtonian (PN) expansion or the Einstein-Infeld-Hoffmann (EIH) equations of motion. From an engineering and astrodynamics perspective, feeding an N-body relativistic model to the OCULUS solver would unlock two mission design capabilities: First, it would enable autonomous perturbation rejection. The variational algorithm would learn to subtly correct the spacecraft's trajectory to counter the gravitational forces of nearby stars, providing realistic estimates for the station-keeping propellant required during the Coasting Arc. Second, and most importantly, it would allow the solver to mathematically discover relativistic gravity assists or flybys. If the transfer trajectory happens to cross paths with an intermediate massive body like the S2 star, the global optimizer could intentionally alter the initial Bang to ensure a close encounter. By exploiting the moving gravitational well of the intermediate star, the spacecraft could extract additional orbital energy, further reducing the overall continuous-thrust ΔV requirements and the total time of flight. Solving this perturbed optimal control problem would represent the ultimate frontier in deep-space autonomous navigation.

Modeling Propulsion Transients and Thrust Rate Constraints

The optimal Bang-Coast-Bang profile derived relies on a mathematical idealization standard in optimal control theory: the instantaneous switching of the thrust. The algorithm assumes that the spacecraft's engine can transition from zero thrust to maximum thrust $F = T_{max}$, and vice versa, in an infinitesimally short time interval ($d\tau \to 0$). In the realm of applied space engineering this assumption must be reassessed. A nuclear fusion reactor cannot ignite instantaneously and the physical processes involved, such as radio-frequency plasma heating or magnetic nozzle stabilization, dictate a finite and significant transient phase. Integrating these ignition and shutdown transients into the optimal control framework would represent a major leap toward high-fidelity mission design. Therefore, a future bounded-rate optimization algorithm would have to learn to anticipate the relativistic slingshot. The solver would need to shift the ignition time (τ_1) backwards, starting the reactor heating phase well before the pericenter, ensuring that the peak thrust is perfectly synchronized with the minimum radial coordinate. By thoroughly analyzing how these transient constraints reshape the thrusting windows, future research could assess the operational flexibility of fusion engines in highly dynamic gravitational environments, providing design requirements for the actual propulsion and transfer optimization.

Extending the Optimization Framework to Solar System Applications

While the S-Stars cluster and the supermassive black hole Sagittarius A* provided the ultimate, extreme theoretical laboratory for this thesis, the relativistic optimal control framework developed has practical potential for advanced mission design within the Solar System. The mathematical and computational architecture, specifically the active propagation of time dilation, the integration of metric tensors into the Hamiltonian, and the resolution of the Boundary Value Problem via continuation methods, can be directly scaled and applied to next-generation interplanetary and interstellar-precursor missions. Although the gravitational field of the Sun is fundamentally weak compared to a supermassive black hole, the classical Newtonian approximations currently employed in mission design become increasingly inadequate when planning highly energetic trajectories that pass exceptionally close to the solar surface. In fact, a spacecraft could plunge deep into the Sun's gravity well, reaching extreme perihelion velocities, and execute a massive propulsive burn at the point of maximum kinetic energy to achieve solar escape velocities. Applying this relativistic optimization solver to such scenarios would be advantageous over standard interplanetary software.

Final Remarks

In conclusion, the intersection of General Relativity and Optimal Control Theory provides a mathematically elegant and robust framework for the future of deep-space exploration. As advanced continuous-thrust technologies evolve from theoretical concepts into engineering realities, the boundaries of human and robotic exploration will inevitably expand beyond the classical confines of the Solar System. Navigating the extreme spacetime curvature of the Galactic Center will demand not only huge propulsive power but also unprecedented algorithmic intelligence. By proving that a spacecraft can autonomously surf the geodetic currents of a supermassive black hole, actively optimizing its fuel consumption while mathematically accounting for the dilation of time, this research aims to demonstrate that the extreme cosmos is not merely a gravitational obstacle to be overcome by brute force, but a highly complex geometric landscape waiting to be understood, mapped, and elegantly navigated.

Appendix A

Christoffel Symbols for Schwarzschild metric

Schwarzschild Radius

$$r_s = \frac{2GM}{c^2} \tag{A.1}$$

Christoffel Symbols

$$\begin{aligned}
\Gamma^t_{rt} &= \Gamma^t_{tr} = \frac{1}{2}\frac{r_s}{r^2 - rr_s} \\
\Gamma^r_{tt} &= \frac{1}{2}c^2\frac{r_s}{r^2}\left(1 - \frac{r_s}{r}\right) \\
\Gamma^r_{rr} &= \frac{1}{2}\frac{r_s}{rr_s - r^2} \\
\Gamma^r_{\theta\theta} &= r_s - r \\
\Gamma^r_{\phi\phi} &= (r_s - r)\sin^2\theta \\
\Gamma^\theta_{r\theta} &= \Gamma^\theta_{\theta r} = \frac{1}{r} \\
\Gamma^\theta_{\phi\phi} &= -\sin\theta\cos\theta \\
\Gamma^\phi_{r\phi} &= \Gamma^\phi_{\phi r} = \frac{1}{r} \\
\Gamma^\phi_{\theta\phi} &= \Gamma^\phi_{\phi\theta} = \frac{1}{\tan\theta}
\end{aligned} \tag{A.2}$$

Christoffel Derivatives in r

$$\begin{aligned}
\partial_r \Gamma^t_{rt} &= \frac{r_s^2/2 - r r_s}{(r^2 - r r_s)^2} \\
\partial_r \Gamma^r_{tt} &= c^2(-\frac{r_s}{r^3} + \frac{3r_s^2}{2r^4}) \\
\partial_r \Gamma^r_{rr} &= \frac{r r_s - r_s^2/2}{(r r_s - r^2)^2} \\
\partial_r \Gamma^r_{\theta\theta} &= -1 \\
\partial_r \Gamma^r_{\phi\phi} &= -\sin^2\theta \\
\partial_r \Gamma^\theta_{r\theta} &= -\tfrac{1}{r^2} \\
\partial_r \Gamma^\theta_{\phi\phi} &= 0 \\
\partial_r \Gamma^\phi_{r\phi} &= -\tfrac{1}{r^2} \\
\partial_r \Gamma^\phi_{\theta\phi} &= 0
\end{aligned} \tag{A.3}$$

Christoffel Derivatives in θ

$$\begin{aligned}
\partial_\theta \Gamma^r_{\phi\phi} &= 2(r_s - r)\sin\theta\cos\theta \\
\partial_\theta \Gamma^\theta_{\phi\phi} &= \sin^2\theta - \cos^2\theta \\
\partial_\theta \Gamma^\phi_{\theta\phi} &= -\tfrac{1}{\sin^2\theta}
\end{aligned} \tag{A.4}$$

Appendix B

Motion equation

$$
\begin{aligned}
\frac{\partial t}{\partial \tau} &= u^t \\
\frac{\partial r}{\partial \tau} &= u^r \\
\frac{\partial \theta}{\partial \tau} &= u^\theta \\
\frac{\partial \phi}{\partial \tau} &= u^\phi \\
\frac{\partial u^t}{\partial \tau} &= -2\Gamma^t_{rt} u^t u^r + \frac{1}{m} f^t \\
\frac{\partial u^r}{\partial \tau} &= -\Gamma^r_{tt}(u^t)^2 - \Gamma^r_{rr}(u^r)^2 - \Gamma^r_{\theta\theta}(u^\theta)^2 - \Gamma^r_{\phi\phi}(u^\phi)^2 + \frac{1}{m} f^r \\
\frac{\partial u^\theta}{\partial \tau} &= -2\Gamma^\theta_{r\theta} u^\theta u^r - \Gamma^\theta_{\phi\phi}(u^\phi)^2 + \frac{1}{m} f^\theta \\
\frac{\partial u^\phi}{\partial \tau} &= -2\Gamma^\phi_{r\phi} u^\phi u^r - 2\Gamma^\phi_{\theta\phi} u^\theta u^\phi + \frac{1}{m} f^\phi \\
\frac{\partial m}{\partial \tau} &= -\frac{F}{I_{sp}\, g_0}
\end{aligned}
\tag{B.1}
$$

Appendix C

Optimal Control Theory Equations

Hamiltonian

$$
\begin{aligned}
H = {} & \lambda_t \, u^t + \lambda_r \, u^r + \lambda_\theta \, u^\theta + \lambda_\phi \, u^\phi \\
& + \lambda_{u^t} \frac{\partial u^t}{\partial \tau} + \lambda_{u^r} \frac{\partial u^r}{\partial \tau} + \lambda_{u^\theta} \frac{\partial u^\theta}{\partial \tau} + \lambda_{u^\phi} \frac{\partial u^\phi}{\partial \tau} + \lambda_m \frac{\partial m}{\partial \tau}
\end{aligned}
\tag{C.1}
$$

Adjoint Variables Equations ($\dot{\lambda}_y = -\frac{\partial H}{\partial y}$)

$$
\begin{aligned}
\dot{\lambda}_t &= 0 \\
\dot{\lambda}_r &= -\lambda_{u^t}\left(-2\frac{\partial \Gamma^t_{rt}}{\partial r}u^t u^r\right) - \lambda_{u^r}\left(-\frac{\partial \Gamma^r_{tt}}{\partial r}(u^t)^2 - \frac{\partial \Gamma^r_{rr}}{\partial r}(u^r)^2 - \frac{\partial \Gamma^r_{\theta\theta}}{\partial r}(u^\theta)^2 - \frac{\partial \Gamma^r_{\phi\phi}}{\partial r}(u^\phi)^2\right) \\
&\quad - \lambda_{u^\theta}\left(-2\frac{\partial \Gamma^\theta_{\theta r}}{\partial r}u^\theta u^r\right) - \lambda_{u^\phi}\left(-2\frac{\partial \Gamma^\phi_{r\phi}}{\partial r}u^\phi u^r\right) - \frac{\partial H_f}{\partial r} \\
\dot{\lambda}_\theta &= -\lambda_{u^r}\left(-\frac{\partial \Gamma^r_{\phi\phi}}{\partial \theta}(u^\phi)^2\right) - \lambda_{u^\theta}\left(-\frac{\partial \Gamma^\theta_{\phi\phi}}{\partial \theta}(u^\phi)^2\right) - \lambda_{u^\phi}\left(-2\frac{\partial \Gamma^\phi_{\theta\phi}}{\partial \theta}u^\theta u^\phi\right) - \frac{\partial H_f}{\partial \theta} \\
\dot{\lambda}_\phi &= 0 \\
\dot{\lambda}_{u^t} &= -\lambda_t - \lambda_{u^t}\left(-2\Gamma^t_{rt}u^r\right) - \lambda_{u^r}\left(-2\Gamma^r_{tt}u^t\right) \\
\dot{\lambda}_{u^r} &= -\lambda_r - \lambda_{u^t}\left(-2\Gamma^t_{rt}u^t\right) - \lambda_{u^r}\left(-2\Gamma^r_{rr}u^r\right) - \lambda_{u^\theta}\left(-2\Gamma^\theta_{\theta r}u^\theta\right) - \lambda_{u^\phi}\left(-2\Gamma^\phi_{r\phi}u^\phi\right) \\
\dot{\lambda}_{u^\theta} &= -\lambda_\theta - \lambda_{u^r}\left(-2\Gamma^r_{\theta\theta}u^\theta\right) - \lambda_{u^\theta}\left(-2\Gamma^\theta_{\theta r}u^r\right) - \lambda_{u^\phi}\left(-2\Gamma^\phi_{\theta\phi}u^\phi\right) \\
\dot{\lambda}_{u^\phi} &= -\lambda_\phi - \lambda_{u^r}\left(-2\Gamma^r_{\phi\phi}u^\phi\right) - \lambda_{u^\theta}\left(-2\Gamma^\theta_{\phi\phi}u^\phi\right) - \lambda_{u^\phi}\left(-2\Gamma^\phi_{r\phi}u^r - 2\Gamma^\phi_{\theta\phi}u^\theta\right) \\
\dot{\lambda}_m &= \boldsymbol{\lambda_V} \cdot \frac{F}{m^2}
\end{aligned}
\tag{C.2}
$$

Bibliography

[1] S. Gillessen et al. "An Update on Monitoring Stellar Orbits in the Galactic Center". In: *The Astrophysical Journal* 837 (Feb. 2017), p. 30. DOI: 10.3847/1538-4357/aa5c41. URL: https://doi.org/10.3847%2F1538-4357%2Faa5c41.

[2] Wikipedia. *Sagittarius A**. Wikipedia, Dec. 2019. URL: https://en.wikipedia.org/wiki/Sagittarius_A.

[3] Judy Liu. *S-Star Cluster Around Sagittarius A* Confirms Einstein's Theory of General Relativity*. NHSJS, July 2021. URL: https://nhsjs.com/2021/s-star-cluster-around-sagittarius-a-confirms-einsteins-theory-of-general-relativity/.

[4] Pedro G. Henriques and Jose Natario. "The Rocket Problem in General Relativity". PhD thesis. Apr. 2012. URL: https://arxiv.org/pdf/1105.5235.

[5] Howard S Seifert, Mark Muir Mills, and Martin Summerfield. *The Physics of Rockets: Dynamics of Long Range rockets*. 1947, pp. 255–272.

[6] L Krause. *Relativistic Rocket Mechanics*. 1960.

[7] Richard Tinder. *Relativistic Flight Mechanics and Space Travel*. Springer Nature, June 2022.

[8] John D Barrow, P C W Davies, and Charles L Harper. *Science and ultimate reality : quantum theory, cosmology, and complexity*. University Press, 2005.

[9] John Archibald Wheeler. *A Journey into Gravity and Spacetime*. W. H. Freeman, June 1999.

[10] Edwin F Taylor, John Archibald Wheeler, and Edmund William Bertschinger. *Exploring black holes : introduction to general relativity*. Addison-Wesley, 2010.

[11] Alexei V. Nesteruk. "A "Participatory Universe" of J. A. Wheeler as an Intentional Correlate of Embodied Subjects and an Example of Purposiveness in Physics". PhD thesis. 2013, pp. 415–437. URL: https://arxiv.org/pdf/1304.2277.

[12] Faculty of Khan. *The Schwarzschild Metric: Complete Derivation | General Relativity*. YouTube, Mar. 2025. URL: https://www.youtube.com/watch?v=6cSYZMM0wU4.

[13] Faculty of Khan. *Schwarzschild Geodesic Equations and Conservation Laws: Derivation*. YouTube, Aug. 2025. URL: https://www.youtube.com/watch?v=I4DTWtiF0DM.

[14] Faculty of Khan. *Deriving the Schwarzschild Metric: Computing the Schwarzschild Radius and Conclusion*. YouTube, Mar. 2025. URL: https://www.youtube.com/watch?v=yIO4u6De6EU.

[15] Faculty of Khan. *Deriving the Christoffel Symbols for a Diagonal Metric | Schwarzschild Metric Example*. YouTube, Feb. 2025. URL: https://www.youtube.com/watch?v=WypC3SJKSVk.

[16] Yosef S Razin, Gary Alan Pajer, Mary Breton, Eric Ham, Joseph B Mueller, Michael Paluszek, Alan H Glasser, and Samuel M Cohen. "A direct fusion drive for rocket propulsion". In: 105 (Dec. 2014), pp. 145–155. DOI: 10.1016/j.actaastro.2014.08.008.

[17] Wikipedia. *Direct Fusion Drive*. Wikipedia, June 2024. URL: https://en.wikipedia.org/wiki/Direct_Fusion_Drive.

[18] Paolo Aime, Marco Gajeri, and Roman Ya. Kezerashvili. "Exploration of trans-Neptunian objects using the Direct Fusion Drive". In: *Acta Astronautica* 178 (Jan. 2021), pp. 257–264. DOI: 10.1016/j.actaastro.2020.09.022. URL: https://arxiv.org/pdf/2009.12633.pdf.

[19] Marco Gajeri, Paolo Aime, and Roman Ya. Kezerashvili. "A Titan mission using the Direct Fusion Drive". In: *Acta Astronautica* 180 (Mar. 2021), pp. 429–438. DOI: 10.1016/j.actaastro.2020.12.013.

[20] Roman Ya Kezerashvili. *Exploration of the solar system and beyond using a thermonuclear fusion drive*. arXiv.org, 2021. URL: https://arxiv.org/abs/2108.01689.

[21] NASA. *Aneutronic Fusion Spacecraft Architecture*. Feb. 2014. URL: https://www.nasa.gov/general/aneutronic-fusion-spacecraft-architecture/.

[22] Brian Wang. *Path to Megawatt Direct Drive Fusion Propulsion Has No Scientific Roadblocks | NextBigFuture.com*. NextBigFuture.com, Oct. 2020. URL: https://www.nextbigfuture.com/2020/10/path-to-megawatt-direct-drive-fusion-propulsion-has-no-scientific-roadblocks.html.

[23] Wikipedia. *Princeton Plasma Physics Laboratory*. Wikipedia, Aug. 2025.

[24] Manuel Arca Sedda, Elisa Bortolas, and Mario Spera. *Black Holes in the Era of Gravitational-Wave Astronomy*. Elsevier, June 2024.

[25] Roland Gredel. *The Galactic Center*. 1996.

[26] *The Nobel Prize in Physics 2020*. NobelPrize.org, 2020. URL: https://www.nobelprize.org/prizes/physics/2020/summary/.

[27] Avery E. Broderick, Abraham Loeb, and Ramesh Narayan. "THE EVENT HORIZON OF SAGITTARIUS A*". In: *The Astrophysical Journal* 701 (July 2009), pp. 1357–1366. DOI: 10.1088/0004-637x/701/2/1357. (Visited on 05/19/2020).

[28] Event Horizon Telescope Collaboration. "First Sagittarius A* Event Horizon Telescope Results". In: *The Astrophysical Journal Letters* (2022).

[29] Clifford M Will. "Gravitational redshift of gravitational clocks". In: *Annals of Physics* 155 (June 1984), pp. 133–157. DOI: 10.1016/0003-4916(84)90255-0. (Visited on 01/06/2020).

[30] Gesellschaft. *Dynamics of Star Clusters and the Milky Way*. 2001.

[31] S. Doeleman. "Event-horizon-scale structure in the supermassive black hole candidate at the Galactic Centre". In: *Nature* 455 (2008), pp. 78–80.

[32] Charles W Misner, Kip S Thorne, and John Archibald Wheeler. *Gravitation*. New York Freeman, 1995.

[33] James B Hartle and Cambridge University Press. *Gravity : an introduction to Einstein's general relativity*. Cambridge Cambridge University Press, 2021.

[34] Luigi Mascolo. *OCULUS -A Unified Visual Solver For Optimal Control Problems Via Indirect Methods*. URL: https://iafastro.directory/iac/paper/id/103041/abstract-pdf/IAC-25,E1,4,4,x103041.brief.pdf?2025-03-27.11:39:08.

[35] Luigi Mascolo. "Low-Thrust Optimal Escape Trajectories from Lagrangian Points and Quasi-Periodic Orbits in a High-Fidelity Model". In: *Polito.it* (Mar. 2023), pp. 1–217. DOI: https://hdl.handle.net/11583/2976595. URL: https://iris.polito.it/handle/11583/2976595.

[36] Lev S Pontrjagin and Revaz V Gamkrelidze. *The mathematical theory of optimal processes*. Gordon and Breach, 1986.

[37] John T Betts. *Practical Methods for Optimal Control and Estimation Using Nonlinear Programming*. SIAM, Jan. 2010.

[38] Richard F Tinder. *Relativistic flight mechanics and space travel : a primer for students, engineers and scientists*. Morgan and Claypool, 2007.

[39] Kenneth K.H Fung, Geraint F Lewis, and Xiaofeng Wu. "The optimisation of low-acceleration interstellar relativistic rocket trajectories using genetic algorithms". In: *Acta Astronautica* 133 (Jan. 2017), pp. 258–268. DOI: 10.1016/j.actaastro.2017.01.033. (Visited on 04/11/2025).

[40] *The Future of Magnetic Confinement Fusion*. Stanford.edu, 2024. URL: http://large.stanford.edu/courses/2024/ph241/thaman1/.

[41] information@eso.org. *Orbits of stars around black hole at the heart of the Milky Way*. www.eso.org, 2024. URL: https://www.eso.org/public/images/eso1825d/.

[42] Robert M Wald. *General relativity*. Univ. Of Chicago Press, 1984.

[43] Sean Carroll. *Spacetime and geometry an introduction to General Relativity - Carroll S. - 2004*. Djvu.online, 2026. URL: https://djvu.online/file/zAozGlXDot7DN? (visited on 03/19/2026).

[44] Barrett O'Neill. *The Geometry of Kerr Black Holes*. Courier Corporation, Jan. 2014.

[45] Maurizio Gasperini. *Relatività Generale e Teoria della Gravitazione*. Springer Science Business Media, July 2010.

[46] K F Long and Springerlink. *Deep Space Propulsion : A Roadmap to Interstellar Flight*. Springer New York, 2012.

[47] Jack Macki and Aaron Strauss. *Introduction to Optimal Control Theory*. Springer Science Business Media, Dec. 2012.

Dedications

Dedications for everyone